Investigation On Tetra-Cationic Heavier Di-Pnictanes

A Thesis

submitted to

Indian Institute of Science Education and Research Pune in partial fulfilment of the requirements for the BS-MS Dual Degree Programme

by

Satyabrata Das

(20201109)

Indian Institute of Science Education and Research Pune

Dr. Homi Bhabha Road,

Pashan, Pune 411008, INDIA.

March, 2025

Supervisor: Dr. Moumita Majumdar

Student: Satyabrata Das

Certificate

This is to certify that this dissertation entitled "**Investigation on Tetra-Cationic Heavier Di-Pnictanes"** towards the partial fulfilment of the BS-MS dual degree programme at the Indian Institute of Science Education and Research, Pune represents study/work carried out by **Satyabrata Das** at Indian Institute of Science Education and Research under the supervision of **Dr. Moumita Majumdar**, Associate Professor, Department of Chemistry, during the academic year **2024-2025**.

Dr. Moumita Majumdar

Supervisor

Committee:

Name of your Guide: Dr. Moumita Majumdar

Name of Your TAC: Dr. R. Boomi Shankar

This thesis is dedicated to my supervisor, family and lab mates.

Declaration

I hereby declare that the matter embodied in the report entitled "**Investigation on Tetra-Cationic Heavier Di-Pnictanes**" are the results of the work carried out by me at the Department of **Chemistry**, Indian Institute of Science Education & Research (IISER) Pune, under the supervision of **Dr. Moumita Majumdar**, and the same has not been submitted elsewhere for any other degree. Wherever others contribute, every effort is made to indicate this clearly, with due reference to the literature and acknowledgement of collaborative research and discussions.

Satyabrata Das

20201109

Table of Contents

List of Tables

List of Schemes

List of Figures

Abstract

A thorough characterization of tetra-cationic dipnictane dimers (Sb = $[1]_2[OTf]_4$, Bi = $[2]_2[OTf]_4$) have been done, the role of solvent in their homolytic cleavage and differing stability in solution by UV-Visible Spectroscopy and the formation of elusive stibine hydride and bismuth hydride species in solution elucidated by NMR spectroscopy. The reactivity of the dimeric compound $[2]_2[OTf]_4$, with diphenyl disulfide (Ph_2S_2), diphenyl diselenide (Ph_2Se_2), p-Benzoquinone ($C_6H_4O_2$) and oxygen (O_2) were carried out giving rise to compounds [LBi-SPh][OTf]$_2$ = [3][OTf]$_2$, [LBi-SePh][OTf]$_2$ = [4][OTf]$_2$, [LBi-OC_6H_4O-BiL][OTf]$_4$ = [5][OTf]$_4$, and [LBi-O-BiL][OTf]$_4$ = [6][OTf]$_4$ respectively. The reaction of $[2]_2[OTf]_4$ with dicobalt octacarbonyl ($Co_2(CO)_8$), dimanganese decacarbonyl ($Mn_2(CO)_{10}$) and bis-cyclopentadienyldiiron tetracarbonyl ($(FeCp(CO)_2)_2$) gave rise to complexes [LBi-$Co(CO)_3$-BiL][OTf]$_3$ = [7][OTf]$_3$, [LBi-$Mn(CO)_5$][OTf]$_2$ = [8][OTf]$_2$, and [LBi-$FeCp(CO)_2$][OTf]$_2$ = [9][OTf]$_2$ respectively featuring a transition metal-pnictogen bond. As the $[2]_2[OTf]_4$ bismuth dimer have a longer shelf-live in solution, allowed us the perform small molecule activations. The compound $[2]_2[OTf]_4$ activates C-C bond in acetonitrile to give [LBi-CH_3][OTf]$_2$ = [10][OTf]$_2$, and O-H bond water to give [LBi-$(\mu\text{-}OH)_2$-BiL][OTf]$_4$ = [11][OTf]$_4$. All these complexes were characterized by NMR Spectroscopy, UV-Visible Spectroscopy and Single-Crystal X-Ray Diffraction analyses.

Acknowledgments

I would like to express my sincere gratitude to my MS Thesis supervisor Dr. Moumita Majumdar for providing me the opportunity to work on this project. Her constant inputs towards my research and maintenance of a healthy working atmosphere have shaped my achievements. I am also thankful to my TAC member Dr. R. Boomi Shankar for giving his thoughtful insights for enhancing the quality of my thesis.

I acknowledge IISER Pune for providing excellent research opportunities for undergraduates and access to the advanced characterization methods of NMR and SC X-ray diffraction facilities, as well as the financial assistance I received during my BS-MS. I would also like to extend my deep appreciation to Mr. Hritwik Haldar and Ms. Akanksha Kumari for their guidance in the form of academic discussions, assistance in analysis, and meaningful suggestions throughout. I also thank Dr. Cem B. Yildiz, our computational collaborator, for providing various computational insights throughout the projects.

I extend my appreciation to my sister, Ms. Abhilipsa Das, and my friend Mr. Asutosh Routa, for their constant encouragement and mental support throughout this period.

Chapter 1 Introduction

This work aimed to establish a thorough understanding of the two main-group heavier bimetallic tetracationic pnictogen compounds through a unique set of reactivities, which will help to understand their electronics, frontier orbitals that take part in the reaction and solution dynamics, as well as solid-state behavior.

Now, stepping back and wondering, "Why is it important to study more about bimetallic complexes?" The answer to this question can be an elaborate one, starting from the cases of dimeric transition-metal based complexes, which are very large and diverse in number and can activate small molecules like H_2, N_2, CO_2, CO, NH_3, etc. These activations often are energy-requiring and sometimes lead to kinetically unstable products, leaving potential room for catalytic conversions and selective chemical transformations, emphasizing the importance of tuning the electronics, which is otherwise challenging or not possible to carry out with either one alone.[1, 2, 3, 4]

Taking main-group based dimers into account, numerous complexes have been stabilized in the last decades. Various ligand systems have tuned the otherwise considered electronically non-flexible elements to achieve many selective chemical transformations.[5]

Fundamentally, the more accessible main-group dimers contain multiple bonds, as they contain the pi-bonds, which are much higher in energy than the carbon-carbon multiple bonds. They are easily accessible in case of heavier elements and tend to react with various substrates. Cornella and co-workers stabilized the well-known triplet bismuthinidene using a bulky indacene ligand that dimerizes in solid state but, in solution, exists as the monomeric form and is known to perform oxidative addition with methyl iodide and cycloaddition reactions.[6] The utilization of bulkier distibene and dibismuthene by Bismuto and co-workers to initially form π-complexes with Jonas' reagent and successively led to the form of cycloaddition products by forming three-membered hetero-metallacycles.[7] There are also numerous other examples containing the P=P, and As=As as well, which have been utilized for the generation of radical species by one-electron reduction or oxidation, cycloaddition products with a variety of unsaturated hydrocarbons, forming new classes of compounds with transition metal substituents, and activations of elemental chalcogens.[8]

Moving to the singly bonded main-group homo-metallic dimers, the dimagnesium complexes come first to mind, containing the magnesium in the +I oxidation state with a tendency to oxidize to +II and act as reducing agents. It activates a variety of organic substrates as well as small molecules like CO, CO_2, N_2, etc. Its use as a reducing agent is further expanded to form low-valent main-group dimers and clusters compounds for groups 13, 14, and 15 by creating new element-element bonds.[9] But isolating the subvalent monomeric species in these complexes is difficult due to its small size and high reactivity. As per literature reports of heavier bonded dipnictanes, few are known to dissociate in solution to give rise to corresponding monomeric persistent radical species which can activate P_4 (Scheme 1) and forms TEMPO adducts.[10, 11, 12] It is essential to note the general use of steric bulk to stabilize sub-valent species can have bond elongation effect in case of σ-bonded dimers, subsequently leading to the formation of radicals in the solution.

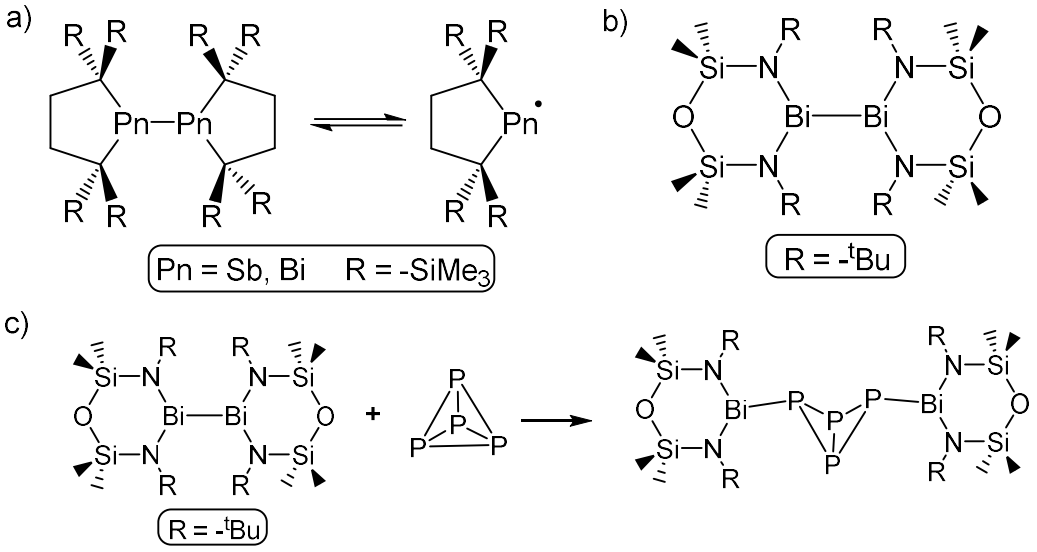

Scheme 1: Examples of neutral heavier main-group dimers. a) Dipnictanes dissociate due to bulky -$SiMe_3$ groups; b) Neutral bismuthane with bulky -tBu group; and c) Radical reactivity of dibismuthane by bond homolysis and activation of P_4.

When we consider the effects of charges on cationic main-group dimers and their applications, the number of examples is surprisingly limited. The decrease in the occurrence of these species is due to coulombic repulsion between the charges and, ultimately, coulomb explosion.[13] Krossing et al. reported the first stable tetracationic digallane species, utilizing the 1,10-Phenanthroline ligand and tetracationic tetramer of Ga(I) formed in solid-state by using the smaller isonitrile ligands is calculated to dissociate in the solution to monomeric Ga(I) species due to coulomb explosion.[14]

Recently, Gilliard and co-workers have synthesized the carbodiphosphine stabilized distibene dications and dibismuthene dications. The stability of the complex is achieved due to a significant delocalization of the positive charge from the antimony center to the ligand backbone. The distibene activates the S-S bond of diphenyl disulfide and undergoes various cycloaddition reactions (Scheme 2).[15] Krossing et al. also established the heavier carbene analogue, digallene dications which dimerizes by the non-classical double-donor acceptor interaction and reacts with diphenyl disulfides, aliphatic alkenes, phosphine, cyclooctyne and insertion between Ga-H, Si-H, and B-H bonds. There are also reports of oligomeric cationic complexes groups 13 and 14, which delocalize a significant amount of the charges to the ligand backbone or dissociate to their monomeric forms in solution.[16]

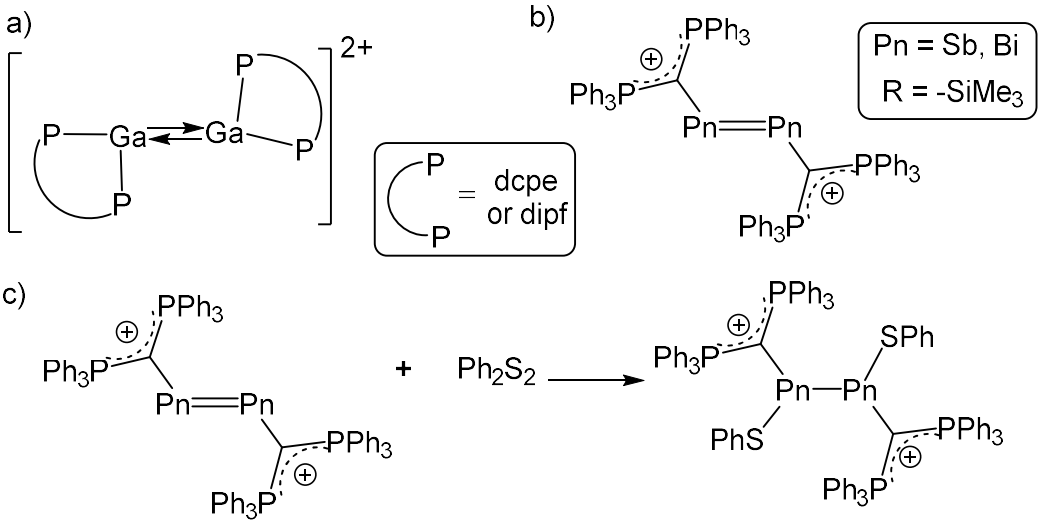

Scheme 2: Examples of cationic heavier main-group dimers. a) Dicationic digallene dissociate to monomeric gallene; b) Carbodiphosphine stabilized distibene dication; and c) Diphenyl disulfide activation by using Carbodiphosphine stabilized distibene dication.

Another interesting class of compounds is the charged radicals. Only a handful of examples of this kind of compound taking part in reactions. In 2017, Tan and co-workers reported the first stable triarylstibine(IV) radical cations, with localized spin on the antimony center and stabilized by the sterics of ligand. Further reactivity studies confirmed its radical nature.[17] In 2024, Lu and Lin reported the hexaaryldiboron dianionic dimer, which homolytically cleaves in solution to give boryl radical anions. This compound is utilized for diborylation reactions with diphenylacetylene, anthracene and elemental chalcogens.[18] Recently we have published the synthesis and reactivity study of a tetracationic distibane which, homolytically cleaves in solution

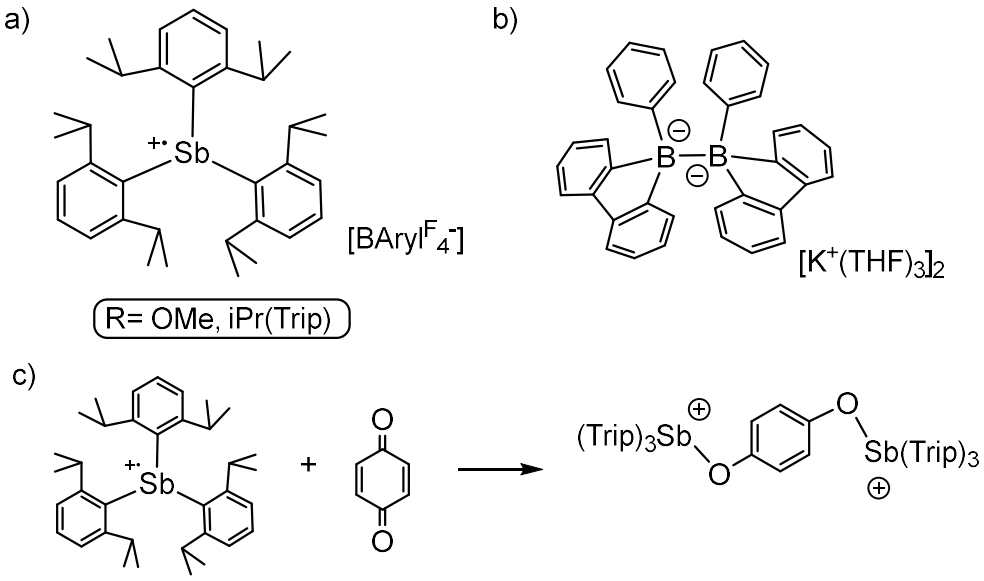

Scheme 3: Examples of main-group charged radical species. a) Antimony(IV) radical cation; b) Hexaaryldiboron dianion known for dissiociation to give radical anion; and c) Radical reactivity of antimony(IV) radical cation with p-Benzoquinone.

to give monomeric dicationic radical confirmed by EPR, which shows reactivity with common radical quenchers (Scheme 4).[19] To the best of our knowledge, it is the first case of a cationic dimer giving radical species in solution. In this study have also performed the redox reactivity of cationic Sb(II) species with transition metal dimers. Taking inspiration from this work the stabilization of a tetracationic dibismuthane [**2**]$_2$[OTf]$_4$ has been achieved in our group.[20]

Among the antimony dimer [**1**]$_2$[OTf]$_4$ and bismuth dimer [**2**]$_2$[OTf]$_4$, the bismuth analogue is more robust and offers a large shelf-life of months. From the literature survey, it is well-known that bismuth is the heaviest stable element in the periodic table having a half-life billion times the estimated age of universe[21] and it has been widely used in the diverse pharmaceuticals[22], alloy[23], petroleum[24], and dye industries[25]. While exploring the roles of bismuth compounds in the field of activation and catalysis, landmark contributions has been made by Cornella et.al. i.e., degradation of SF_5 leading to the formation of dicationic dibismuthane as an intermediate, bismuth redox shuttles between +I and +III as well as +III and +V for Hydrodefluorination of polyfluoroarenes and deoxygenation of nitrous oxide using pinacol boranes respectively.[26, 27] In this thesis work, the evidently different solvent dynamics observed for [**2**]$_2$[OTf]$_4$ with the unusual activation of acetonitrile, analogous reactivity studies and characterizations were performed to investigate the presence of radical in solution. As the cooperation between transition metal and main-group elements is well

established, attempts at synthesis and characterization of TM-Bi complexes were made. Further the activations of acetonitrile (CH_3CN), and water (H_2O) by cationic dimer [**2**]$_2$[OTf]$_4$ also shows its potential to be explored in small molecule activation chemistry, catalysis and polymerization.

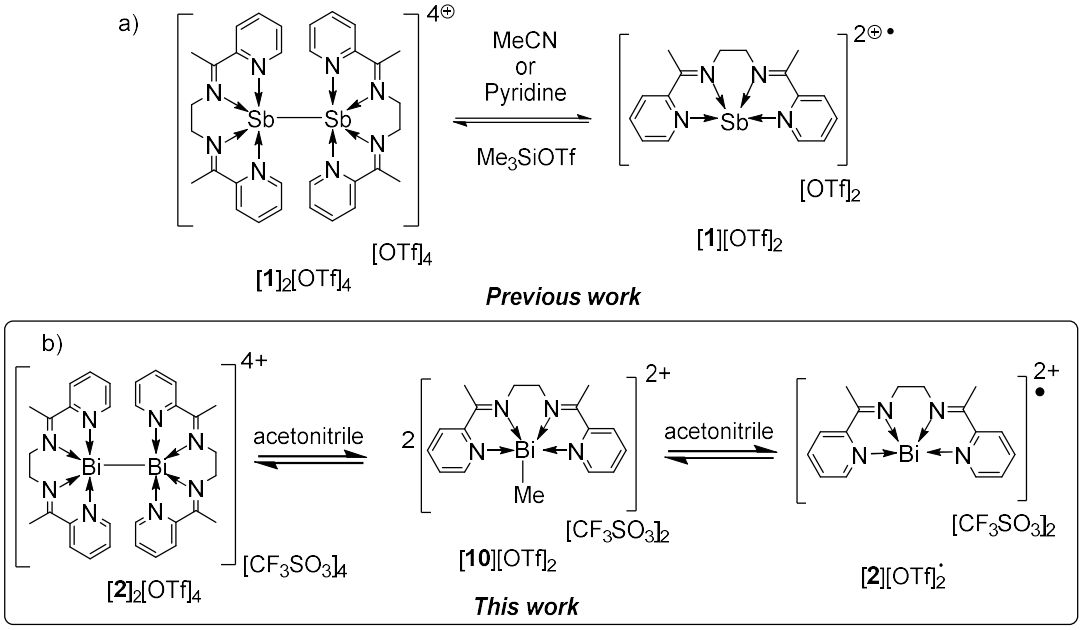

Scheme 4: Cationic dimers giving radical species in solution. a) Previous work: Tetracationic distibane, a component equilibrium in solution; b) This work: Tetracationic dibismuthane, a three component equilibrium in solution.

Chapter 2 Materials and Methods

General Procedures:

All the compounds mentioned here are air and moisture-sensitive hence, manipulations mentioned are either carried in an argon-filled glove box or under an argon environment supplied by standard Schlenk line techniques. Acetonitrile was dried by refluxing and stirring over anhydrous calcium hydride kept over 3 Å molecular sieves. Tetrahydrofuran was dried by refluxing and stirring it overnight over a mixture of sodium and benzoquinone. Diethyl ether was distilled, degassed, and stored in a solvent solvent-protective system under an argon atmosphere. [**1**]$_2$[OTf]$_4$[19] and Bi(OTf)$_3$[28] was prepared according to the reported procedure. Acetonitrile-D3 (CD_3CN) ampoules were purchased from Sigma Aldrich and used as they are. All the other chemicals were purchased from Sigma Aldrich, TCI Chemicals, and Thermo Fisher Chemicals and used as received. ^{1}H and ^{13}C{^{1}H} NMR spectra were referenced to external $SiMe_4$ using the residual signals of the deuterated solvent (^{1}H) or the solvent itself (^{13}C{^{1}H}). ^{19}F and ^{77}Se were referenced to external $C_6H_5CF_3$ (TFT) and $SeMe_2$ (plus 5 % C_6D_6). NMR spectra were recorded on Bruker AVANCE III HD ASCEND 9.4 Tesla/400 MHz and Bruker AVANCE III HD ASCEND 14.1 Tesla/600 MHz NMR spectrometers. Solution phase UV/Vis spectra were acquired from SHIMADZU UV-1900 and UV-3600 plus UV-VIS-NIR spectrophotometer using quartz cells with a path length of 1 cm and analyzed through Origin software. Melting points are determined by filling samples in NMR tubes under a protective argon atmosphere. Single crystal data were collected on both Bruker SMART APEX four-circle diffractometers equipped with Bruker APEX-II CCD diffractometers using Mo Kα radiation (0.71073 Å), analyzed through APEX4 software and refinements performed in Olex2 software. Infrared spectroscopic data were recorded in Bruker Alpha-II FTIR-Eco ATR and Opus software. EPR spectra were recorded at 5 K using a closed cycle Helium cryostat (Cryogenic CF VTC).

Synthesis of [L$_2$Bi$_2$][OTf]$_4$ [2]$_2$[OTf]$_4$: [**2**]$_2$[OTf]$_4$ was prepared according to the reported procedure.[20] Decomp. of [**2**]$_2$[OTf]$_4$: 184°C

NMR Recorded at time, t = 0:

^{1}H NMR (400 MHz, CD_3CN, 298 K) δ 8.74 (m, 2H, *o*-Pyr-*H*); 8.10 (td, *J* = 7.8, 1.7, 2H, *m*-Pyr-*H*); 7.93 (d, *J* = 7.9, 2H, *m*-Pyr-*H*); 7.78 (ddd, *J* = 7.6, 5.2, 1.2, 2H, *p*-Pyr-*H*); 4.77-4.73 (m, 2H, -C*H*$_2$-C*H*$_2$−); 4.57-4.55 (m, 2H, -C*H*$_2$-C*H*$_2$−); 2.80 (s, 6H, -C*H*$_3$) ppm.

$^{13}C\{^1H\}$ NMR (101 MHz, CD_3CN, 298 K) δ 178.85 (*C*=N); 151.35 (Pyr-C_i); 150.10 (Pyr-C_o); 142.63 (Pyr-C_p); 129.69 (Pyr-C_m); 128.85 (Pyr-C_m); 55.15 (−CH_2-CH_2−); 20.89 (−CH_3) ppm.

$^{19}F\{^1H\}$ NMR (377 MHz, CD_3CN, 298 K) δ -79.12 (s) ppm.

NMR Recorded at time t = 3h:

^1H NMR (600 MHz, CD_3CN, 298 K) δ 9.28 (d, *J* = 5.8, 2H, *o*-Pyr-*H*); 9.02 (d, *J* = 5.0, 2H, *o*-Pyr-*H*); 8.43-8.38 (m, 2H, *p*-Pyr-*H*); 8.23-8.18 (m, 2H, *p*-Pyr-*H*); 7.92 (ddd, *J* = 6.9, 5.0, 1.5, 2H, *m*-Pyr-*H*); 7.92 (ddd, *J* = 7.6, 5.2, 1.2, 2H, *m*-Pyr-*H*); 7.67 (ddd, *J* = 6.9, 5.0, 1.5, 2H, *m*-Pyr-*H*); 4.39-4.35 (m, 2H, -CH_2-CH_2−); 3.99-3.94 (m, 2H, -CH_2-CH_2−); 2.73 (s, 6H, -CH_3) ppm.

$^{13}C\{^1H\}$ NMR (151 MHz, CD_3CN, 298 K) δ 178.84 (*C*=N); 176.56 (*C*=N); 152.32 (Pyr-C_i); 151.36 (Pyr-C_i); 150.66 (Pyr-C_o); 150.09 (Pyr-C_o); 142.62 (Pyr-C_p); 142.02 (Pyr-C_p); 129.86 (Pyr-C_m); 128.86 (Pyr-C_m);128.53 (Pyr-C_m); 121.35 (q, J = 320 Hz, CF_3SO_3); 55.15 (−CH_2-CH_2−); 53.54 (−CH_2-CH_2−); 53.52 (−CH_2-CH_2−); 20.87 (−CH_3); 19.84 (−CH_3) ppm.

$^{19}F\{^1H\}$ NMR (564 MHz, CD_3CN, 298 K) δ -80.21 (s) ppm.

Synthesis of [LBiSPh][OTf]$_2$ [3][OTf]$_2$: [**2**]$_2$[OTf]$_4$ (0.040 g, 0.0258 mmol) and S_2Ph_2 (0.00564 g, 0.0258 mmol) were combined in 6 mL acetonitrile solvent, leading to fading of the yellowish color of the solution to colourless and stirred for 1 day for completion. The product was collected through filtration followed by diethylether layering of acetonitrile solution maintained at -30°C. Light-green single crystals of [**3**][OTf]$_2$ was obtained in 60 % yield (27.32 mg). Decomp. of [**3**][OTf]$_2$: 191(2)°C.

^1H NMR (600 MHz, CD_3CN, 298 K) δ 9.32-9.30 (m, 2H, *o*-Pyr-*H,* Bi-Me); 9.17 – 9.16(m, 2H, *o*-Pyr-*H*); 8.36 – 8.32 (m, 2H, *p*-Pyr-*H*, Bi-Me); 8.27 (td, *J* = 7.8, 1.7, 2H, *p*-Pyr-*H*); 8.15- 8.14 (d, 2H, *J* = 9.1, *m*-Pyr-*H*); 7.92 – 7.90 (m, 2H, *m*-Pyr-*H*); 7.89 – 7.88 (m, 2H, *m*-Pyr-*H,* Bi-Me*),* 6.98 – 6.95 (m, 2H, *o*-SPh-*H*); 6.73- 6.71 (m, H, *p*-SPh-*H*); 6.69 - 6.68 (m, 2H, *m*-SPh-*H*); 4.57- 4.53 (m, 2H, -CH_2-CH_2−); 4.42-4. 4.36(m, 2H, -CH_2-CH_2−); 4.35-4.32 (m, 2H, -CH_2-CH_2−), 4.24-4.20 (m, 2H, -CH_2-CH_2−), 2.72 (s, 6H, -CH_3); 2.58 (s, 6H, -CH_3), 1.41(s, 3H, Bi-CH_3) ppm.

$^{13}C\{^1H\}$ NMR (151 MHz, CD_3CN, 298 K) δ 176.54 (*C*=N); 176.15 (*C*=N); 152.30 (Pyr-C_i); 151.18 (Pyr-C_i); 150.65 (Pyr-C_o); 150.49 (Pyr-C_o); 142.22 (Pyr-C_p); 142.02 (Pyr-C_p); 131.73 (SPh-C_i); 130.24 (Pyr-C_m); 130.01 (Pyr-C_m); 129.51 (SPh-C_p); 128.52 ((Pyr-C_m); 128.31(SPh-C_o); 128.14 (SPh-C_m); 121.35 (q, J = 320 Hz, CF_3SO_3); 53.81 (−CH_2-CH_2−); 53.53 (−CH_2-CH_2−); 20.00 (−CH_3); 19.84 (−CH_3) ppm

$^{19}F\{^1H\}$ NMR (564 MHz, CD_3CN, 298 K) δ -80.26 (s) ppm.

Synthesis of [LBiSePh][OTf]$_2$ [4][OTf]$_2$: [**2**]$_2$[OTf]$_4$ (0.040 g, 0.0258 mmol) and Se_2Ph_2 (0.00807 g, 0.0258 mmol) were combined in 6 mL acetonitrile solvent, leading

to immediate fading of the yellowish color of the solution to light-green color and stirred for 1 day for completion. The product was collected through filtration followed by diethylether layering of acetonitrile solution maintained at -30°C. Dark Yellow single crystals of [**4**][OTf]$_2$ was obtained in 62 % yield (29.73 mg). Decomp. of [**4**][OTf]$_2$: 188(2)°C.

^{1}H NMR (600 MHz, CD_3CN, 298 K) δ 9.31 (d, J = 5.1, 2H, *o*-Pyr-*H,* Bi-Me); 9.18 (d, J = 7.0, 2H, *o*-Pyr-*H*); 8.35 – 8.33 (m, 2H, *p*-Pyr-*H*, Bi-Me); 8.27 (td, *J* = 7.8, 1.7, 2H, *p*-Pyr-*H*); 8.14 (d, 2H, *J* = 8.1, *m*-Pyr-*H*); 7.89 (dd, J = 7.7, 2H, *m*-Pyr-*H*); 6.98 – 6.94 (m, 2H, *o*-SPh-*H*), 6.84 – 6.81 (m, H, *p*-SPh-*H*); 6.80- 6.79 (m, 2H, *m*-SPh-*H)* 4.58- 4.51 (m, 2H, -CH_2-CH_2−); 4.43 - 4.35 (m, 2H, -CH_2-CH_2−); 4.34-4.33 (m, 2H, -CH_2-CH_2−), 4.28-4.18 (m, 2H, -CH_2-CH_2−), 2.72 (s, 6H, -CH_3); 2.56 (s, 6H, -CH_3), 1.41(s, 3H, Bi-CH_3) ppm.

^{13}C{^{1}H} NMR (151 MHz, CD_3CN, 298 K) δ 176.54 (*C*=N); 175.89 (*C*=N); 152.30 (Pyr-C_i); 151.19 (Pyr-C_i); 150.65 (Pyr-C_o); 150.47 (Pyr-C_p); 142.20.88 (Pyr-C_o); 142.02.51 (Pyr-C_m); 139.07 (Pyr-C_m); 130.47 (Pyr-C_m); 125.50.99 (SPh-C_i); 128.41 (Pyr-C_o); 128.52 (SPh-C_p); 128.42(SPh-C_m); 121.35 (q, J = 320 Hz, CF_3SO_3); 53.91 (−CH$_2$-CH$_2$−); 53.52 (−CH$_2$-CH$_2$−); 19.96 (−CH$_3$); 19.84 (−CH$_3$) ppm

^{19}F{^{1}H} NMR (564 MHz, CD_3CN, 298 K) δ -80.25 (s) ppm.

^{77}Se{^{1}H} NMR (77 MHz, CD_3CN, 298 K) δ 303.29 (s) ppm.

Synthesis of [L$_2$Bi$_2$O$_2$C$_6$H$_4$][OTf]$_4$ [5][OTf]$_4$: [**2**]$_2$[OTf]$_4$ (0.040 g, 0.0258 mmol) and p-Benzoquinone (0.00279 g, 0.0258 mmol) were combined in 6 mL acetonitrile solvent, leading to immediate change of the yellowish color of the solution to orange color and stirred overnight for completion. The product was collected through filtration followed by diethylether layering of acetonitrile solution maintained at -30°C. Dark orange single crystals of [**5**][OTf]$_4$ was obtained in 58 % yield (24.76 mg). Decomp. of [**5**][OTf]$_4$: 190(2)°C.

Synthesis of [L$_2$Bi$_2$O][OTf]$_4$ [6][OTf]$_4$: [**2**]$_2$[OTf]$_4$ (0.040 g, 0.0258 mmol) and TEMPO (0.00404 g, 0.0258 mmol) were combined in 6 mL acetonitrile solvent, leading to immediate change of the yellowish color of the solution to greenish yellow color and stirred overnight for completion. The product was collected through filtration followed by diethylether layering of acetonitrile solution maintained at -30°C. Yellowish green single crystals of [**6**][OTf]$_4$ was obtained in 65 % yield (25.61 mg). Decomp. of [**6**][OTf]$_4$: 180(2)°C.

[**6**][OTf]$_4$ was also obtained by exposing [**2**]$_2$[OTf]$_4$ to air, followed by color change and subsequent filtration and crystallization at -30°C to give Yellowish green single crystals with some crystals of [**12**][OTf]$_4$.

^{1}H NMR (600 MHz, CD_3CN, 298 K) δ 8.85 (d, *J* = 5.0, 2H, *o*-Pyr-*H*); 8.55 (s, 2H, *o*-Pyr-*H*); 8.14 (td, J= 7.8, 2H, *p*-Pyr-*H*); 8.10 (d, *J* = 8.0, 2H, *p*-Pyr-*H*); 8.03 (m, 2H, *m*-Pyr-*H*); 7.98 (d, *J* = 8.0, 2H, *p*-Pyr-*H*); 7.69 (dd, *J* = 7.7, 4.9, 2H, *p*-Pyr-*H*); 7.40 (s, 2H, *m*-Pyr-*H*); 4.60 (d, 4H, *J* = 8.4, -C*H*$_2$-C*H*$_2$−); 4.47-4. 43(m, 2H, -C*H*$_2$-C*H*$_2$−); 4.34-4. 29(m, 2H, -C*H*$_2$-C*H*$_2$−)2.72 (s, 6H, -C*H*$_3$); 2.50 (s, 6H, -C*H*$_3$) ppm

^{13}C{^{1}H} NMR (151 MHz, CD_3CN, 298 K) δ 176.13 (*C*=N); 175.78 (*C*=N); 152.07 (Pyr-*C*$_i$); 151.63 (Pyr-*C*$_i$); 149.85 (Pyr-*C*$_o$); 149.76 (Pyr-*C*$_o$); 142.49 (Pyr-*C*$_p$); 142.27 (Pyr-*C*$_p$); 129.66 (Pyr-*C*$_m$); 129.10 (Pyr-*C*$_m$); 128.13 (Pyr-*C*$_m$); 128.02 (Pyr-*C*$_m$); 121.35 (q, J = 320 Hz, CF_3SO_3); 53.70 (−*C*H$_2$-*C*H$_2$−); 53.90 (−*C*H$_2$-*C*H$_2$−); 19.40 (−*C*H$_3$); 19.11 (−*C*H$_3$) ppm

^{19}F{^{1}H} NMR (564 MHz, CD_3CN, 298 K) δ -80.27 (s) ppm.

Synthesis of [L$_2$Bi$_2$Co(CO)$_3$][OTf]$_3$ [7][OTf]$_3$: [**2**]$_2$[OTf]$_4$ (0.040 g, 0.0258 mmol) and $Co_2(CO)_8$ (0.00884 g, 0.0258 mmol) were combined in 6 mL acetonitrile solvent, leading to change of the yellowish color of the solution to a dark red color over a period of 30 seconds followed by stirring for 1 day for completion. The product was collected through filtration followed by diethylether layering of acetonitrile solution maintained at -30°C. Red single crystals of [**7**][OTf]$_3$ was obtained in 64 % yield (26.62 mg). Decomp. of [**7**][OTf]$_3$: 190(2)°C.

^{1}H NMR (600 MHz, CD_3CN, 298 K) δ 15.45-14.66 (br, Co(I)-CH_3CN); 9.28 (d, *J* = 5.8, *o*-Pyr-*H*); 9.02 (d, J = 5.0, *o*-Pyr-*H*); 8.43 – 8.38 (m, 2H, *p*-Pyr-*H*); 8.23-8.18 (m, *p*-Pyr-*H*); 7.93-7.91 (m, 2H, *p*-Pyr-*H*); 7.68-7.66 (m, 2H, *m*-Pyr-*H*); 4.39–4.35(m, 2H, -C*H*$_2$-C*H*$_2$−), 3.98 – 3.94 (m, 2H, -C*H*$_2$-C*H*$_2$−); 2.79 (s, 6H, -C*H*$_3$), 2.73 (s, 6H, -C*H*$_3$) ppm

^{13}C{^{1}H} NMR (151 MHz, CD_3CN, 298 K) δ 201.67 (Co-*CO*), 191.27 (Co-*CO*), 176.58 (*C*=N); 173.73 (*C*=N); 151.01 (Pyr-*C*$_i$); 150.39 (Pyr-*C*$_i$); 141.42 (Pyr-*C*$_p$); 141.40 (Pyr-*C*$_p$); 128.71 (Pyr-*C*$_O$); 128.61 (Pyr-*C*$_O$); 127.61 (Pyr-*C*$_m$); 127.46 (Pyr-*C*$_m$); 121.35 (q, J = 320 Hz, CF_3SO_3); 65.28 (−*C*H$_2$-*C*H$_2$); 53.47 (−*C*H$_2$-*C*H$_2$) 53.19 (−*C*H$_2$-*C*H$_2$−); 19.67 (−*C*H$_3$); 19.06 (−*C*H$_3$); 14.64 (−*C*H$_3$) ppm

^{19}F{^{1}H} NMR (564 MHz, CD_3CN, 298 K) δ -80.21 (s) ppm.

Synthesis of [LBiMn(CO)$_5$][OTf]$_2$ [8][OTf]$_2$: [**2**]$_2$[OTf]$_4$ (0.040 g, 0.0258 mmol) and $Mn_2(CO)_{10}$ (0.0106 g, 0.0258 mmol) were combined in 6 mL acetonitrile solvent, leading to change of the yellowish color of the solution to a dull yellow color over a period of 7 days for completion. The product was collected through filtration followed

by diethylether layering of acetonitrile solution maintained at -30°C. Dull yellow single crystals of [**8**][OTf]$_2$ was obtained in 40 % yield (20.83 mg). Decomp. of [**8**][OTf]$_2$: 160(2)°C.

Synthesis of [LBiFe(CO)$_2$Cp][OTf]$_2$ [9][OTf]$_2$: [**2**]$_2$[CF_3SO_3]$_4$ (0.040 g, 0.0258 mmol) and $Fe_2(CO)_4Cp_2$ (0.00915 g, 0.0258 mmol) were combined in 6 mL acetonitrile solvent, leading to change of the yellowish color of the solution to a bright red color over a period of 1 day for completion. The product was collected through filtration followed by diethylether layering of acetonitrile solution maintained at -30°C. Bright red single crystals of [**9**][OTf]$_2$ was obtained in 67 % yield (34.27 mg). Decomp. of [**9**][OTf]$_2$: 182(2)°C.

^{1}H NMR (600 MHz, CD_3CN, 298 K) δ 9.22- 9.20 (m, *o*-Pyr-*H*); 8.57 (s, *o*-Pyr-*H*); 8.39 – 8.37 (m, 2H, *p*-Pyr-*H*); 8.34-8.31 (m, *p*-Pyr-*H*); 8.28-8.27 (m, 2H, *p*-Pyr-*H*); 8.09-7.98 (m, 2H, *m*-Pyr-*H*); 7.85 – 7.82(m, 2H, *m*-Pyr-*H*), 5.08 (s, 5H, Fe-*cp*); 4.07-4.69 (m, 2H, -C*H*$_2$-C*H*$_2$−) 4.61- 4.59 (m, 2H, -C*H*$_2$-C*H*$_2$−); 4.48 - 4.44 (m, 2H, -C*H*$_2$-C*H*$_2$−); 4.16-4.13 (m, 2H, -C*H*$_2$-C*H*$_2$−), 2.79 (s, 6H, -C*H*$_3$), 2.72 (s, 6H, -C*H*$_3$) ppm

^{13}C{^{1}H} NMR (151 MHz, CD_3CN, 298 K) δ 199.34 (Fe-*CO*) 175.75 (*C*=N); 152.27 (Pyr-*C*$_i$); 150.67 (Pyr-*C*$_i$); 142.46 (Pyr-*C*$_o$); 141.69 (Pyr-*C*$_o$); 129.22 (Pyr-*C*$_m$); 128.97 (Pyr-*C*$_m$); 125.02 (q, J = 320 Hz, CF_3SO_3); 86.02 (Fe-*Cp*); 82.20 (−*C*H$_2$-*C*H$_2$) 54.15 (−*C*H$_2$-*C*H$_2$−); 20.50 (−*C*H$_3$) ppm.

^{19}F{^{1}H} NMR (564 MHz, CD_3CN, 298 K) δ -80.24 (s) ppm.

Acetonitrile C-C bond activation [LBiMe][OTf]$_2$ [10][OTf]$_2$: This comes as a side products for many reactions mentioned above, amount varies and takes some time for activation. Colorless crystals suitable for mounting were obtained from the reaction medium.

^{1}H NMR (600 MHz, CD_3CN, 298 K) δ 9.32-9.30 (m, 2H, *o*-Pyr-*H,* Bi-Me); 8.36 – 8.32 (m, 2H, *p*-Pyr-*H*, Bi-Me); 7.89 – 7.88 (m, 2H, *m*-Pyr-*H,* Bi-Me*),* 4.24-4.20 (m, 2H, -C*H*$_2$-C*H*$_2$−), 2.58 (s, 6H, -C*H*$_3$), 1.41(s, 3H, -C*H*$_3$) ppm.

^{13}C{^{1}H} NMR (151 MHz, CD_3CN, 298 K) δ 152.29 (*C*=N); 151.17 (*C*=N); 150.65 (Pyr-*C*$_i$); 142.21 (Pyr-*C*$_o$); 137.95 (Pyr-*C*$_p$); 130.27 (Pyr-*C*$_m$); 130.61 (Pyr-*C*$_m$); 121.35 (q, J = 320 Hz, CF_3SO_3); 53.81 (−*C*H$_2$-*C*H$_2$−); 53.53 (−*C*H$_2$-*C*H$_2$−); 20.00 (−*C*H$_3$); 19.84 (−*C*H$_3$) ppm.

^{19}F{^{1}H} NMR (564 MHz, CD_3CN, 298 K) δ -80.26 (s) ppm.

Activation of O-H bond of H_2O $[L_2Bi_2(OH)_2][OTf]_4$ [11][OTf]$_4$: [**2**]$_2$[OTf]$_4$ (0.040 g, 0.0258 mmol) and H_2O (0.00046 mL, 0.0258 mmol) were combined in 6 mL acetonitrile solvent, leading to immediate change of the yellowish color of the solution to greenish yellow color and stirred overnight for completion. The product was collected through filtration followed by diethylether layering of acetonitrile solution maintained at -30°C. Colorless single crystals of [**11**][OTf]$_4$ was obtained in 70 % yield (31.55 mg). Decomp. of [**11**][OTf]$_4$: Above 200°C.

^{1}H NMR (600 MHz, CD_3CN, 298 K) δ 8.85 (d, *J* = 4.9, 2H, *o*-Pyr-*H*); 8.53 (d, *J* = 5.0, 2H, *o*-Pyr-*H*); 8.15-8.12 (m, 2H, *p*-Pyr-*H*); 8.08 (d, *J* = 7.9 2H, *p*-Pyr-*H*); 8.02- 7.98 (m, *m*-Pyr-*H*); 7.69-7.67 (m, 2H, *p*-Pyr-*H*); 7.39- 7.37 (m, *p*-Pyr-*H*); 6.55 (s, *m*-Pyr-*H*); 4.64-4.44 (m, 2H, -C*H*$_2$-C*H*$_2$−); 4.35-4. 30(m, 2H, -C*H*$_2$-C*H*$_2$−); 2.72 (s, 6H, -C*H*$_3$); 2.50 (s, 6H, -C*H*$_3$) ppm.

^{13}C{^{1}H} NMR (151 MHz, CD_3CN, 298 K) δ 176.06 (*C*=N); 175.68 (*C*=N); 152.05 (Pyr-*C*$_i$); 151.63 (Pyr-*C*$_i$); 149.83 (Pyr-*C*$_o$); 149.71 (Pyr-*C*$_o$); 142.45 (Pyr-*C*$_p$); 142.24 (Pyr-*C*$_p$); 129.61 (Pyr-*C*$_m$); 129.03 (Pyr-*C*$_m$); 128.10 (Pyr-*C*$_m$); 127.94 (Pyr-*C*$_m$); 121.35 (q, J = 320 Hz, CF_3SO_3); 53.70 (−*C*H$_2$-*C*H$_2$−); 53.90 (−*C*H$_2$-*C*H$_2$−); 19.36 (−*C*H$_3$); 19.06 (−*C*H$_3$) ppm.

^{19}F{^{1}H} NMR (564 MHz, CD_3CN, 298 K) δ -80.72 (s) ppm.

Chapter 3 Results and Discussion

Elusive Pnictogen Hydride detection:

The synthesis of [**2**]$_2$[OTf]$_4$[20] was carried out by the reported procedure by the dehydrocoupling pathway. For the proof of concept there should be the release of hydrogen gas preceded by the formation of transient bismuth hydride species. Performing a low-temperature NMR of in-situ reaction mixture containing the Bis(α-iminopyridine) ligand **L**, the corresponding triflate salt Bi(OTf)$_3$) and Triethylsilane at -40°C in acetonitrile gave a new sharp peak at 4.67 ppm indicating the release of dihydrogen during the formation of the tetracationic dimer.[19] For [**2**]$_2$[OTf]$_4$ two broad peaks centred at 13 and 14 ppm were observed which indicates the possible Bi-H in the solution (Figure 9), the value deviates from the reported one.[29]

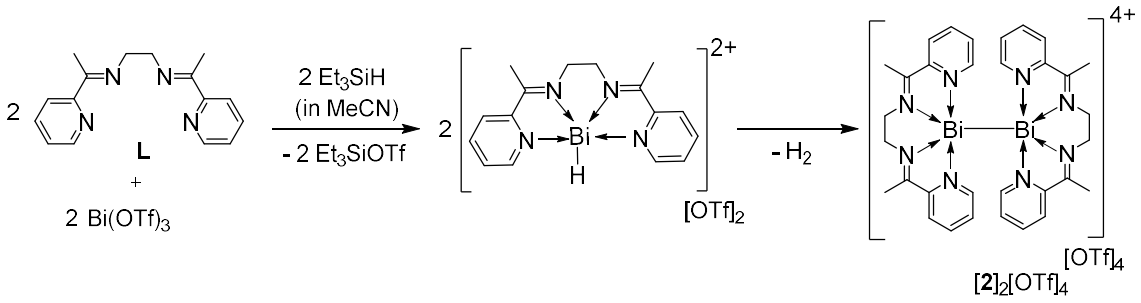

Scheme 5: Synthetic pathway for the tetracationic dimers with the hydride intermediates.

Detail Spectroscopic Characterization of [2]$_2$[OTf]$_4$:

[**2**]$_2$[OTf]$_4$ was characterized earlier by only Single Crystal X-ray diffraction as a red-colored crystal, a better data than the earlier was acquired (Figure 1).[20] In contrast to [**1**]$_2$[OTf]$_4$, which persisted in solution for nearly thirty minutes, [**2**]$_2$[OTf]$_4$ is remarkably stable in solution with a shelf-life of more than two months without notable degradation. However, it shows a solvent-dependent color change analogous to [**1**]$_2$[OTf]$_4$, ranging from red when highly concentrated to yellow when intermediate and finally giving a bright green color when diluted. An EPR measurement gave a broad peak centered at 350 mT (Figure 2b), depicting the formation of dicationic bismuth radical species [**2**][OTf]$_2^{\bullet}$. The dynamics of [**2**]$_2$[OTf]$_4$ in solution NMR measurements were studied in deuterated acetonitrile. The ^{1}H NMR performed immediately at a concentration of 33.33 mM led to the detection of only one set of peaks (Figure 10). The same was noticed from the ^{13}C{^{1}H} NMR spectra (Figure 11), which is in stark contrast to the dimer monomer equilibrium observed in the case of [**1**]$_2$[OTf]$_4$, which contains a

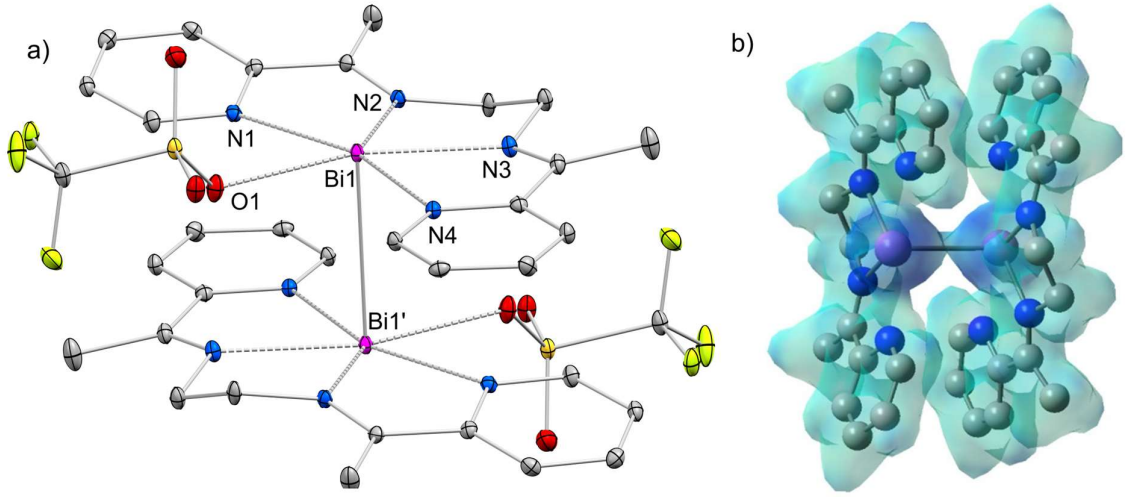

Figure 1: Study of [**2**]$_2$[OTf]$_4$. a) Modified Molecular structure of the cationic fully grown [**2**]$_2$[OTf]$_4$ in the solid state shown for better representation (thermal ellipsoids at 30%, H atoms and two counter anions are omitted for clarity). Selected bond lengths [Å]: Bi1-N2= 2.403(4), Bi1-N1= 2.557(4), Bi1-N3= 2.404(4), Bi1-N4= 2.583(4), Bi1-Bi1= 3.1618(7), Bi1-O1= 2.736(3); b) Electrostatic potential map of [**2**]$_2$[CF_3SO_3]$_4$ with significant positive charge on bismuth.

mixture of dimer and monomer at higher concentration. This presents two unique cases: the first set of peaks observed belongs to the dimer, and the second is the set of peaks observed belongs to the wholly dissociated monomer. A ^{1}H Diffusion ordered spectroscopy (DOSY) NMR was performed, giving rise to two distinct diffusion coefficients (Figure 13) for two different species in solution, with the molecular weight of the slower species being nearly twice of the faster one; same was observed in ^{19}F DOSY . An NMR experiment was performed after a three-hour delay after adding acetonitrile to capture the second species. Two sets of peaks were found in ^{1}H NMR

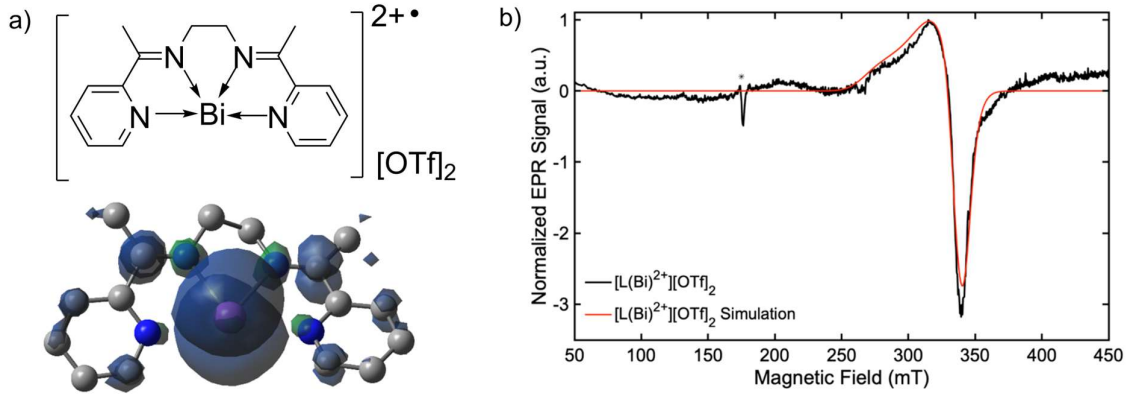

Figure 2: Investigation of the paramagnetic molecule [**2**][OTf]$_2$•. a) spin-density plot for [**2**][OTf]$_2$• showing the spin-localization at bismuth center; b) Experimental (black line) and simulated (red line) continuous-wave EPR spectra of [**2**]$_2$[OTf]$_4$ as a frozen solution obtained at the X-band (9.634 GHz). Experimental conditions: temperature 5 K; modulation amplitude = 1 mT; modulation frequency = 100 kHz; time constant = 81.92 ms; scan time = 335.54 s; number of scans = 1; * = signal from the resonator.

and $^{13}C\{^{1}H\}$; the position of the peaks matched what was observed for DOSY (Figure 14 and 15), leading to the question of whether the dimer takes some time to break into monomer which, despite being a radical, gives sharp peaks because of spin localization as was observed for [**1**]$_2$[OTf]$_4$ and is backed by the computational findings (Figure 2a). When the solvent was recrystallized, a few colorless crystals of a Bi-CH_3 species [**10**][OTf]$_2$ were found (will be discussed in a later section).

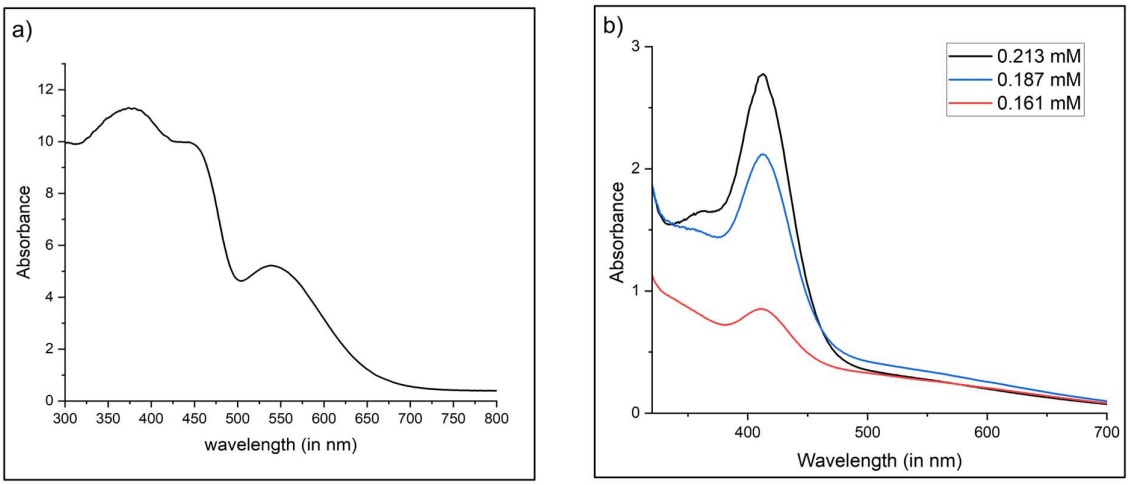

Figure 3: UV-Visible characterization of [**2**]$_2$[OTf]$_4$. a) solid state having large peaks around 400 nm and a peak at 550 nm b) solution state in acetonitrile in three different concentrations - 0.161 mM (red), 0.187 mM (blue), and 0.213 mM (black).

Absorbance measurements were performed to get a clear picture of the changes solid and solution state. In solid-state UV-Visible spectra, there are two broad peaks, the first centered at 410 nm and the second centered at 550 nm (Figure 3a), as in solid state, the bond homolysis is not possible; these transitions were assigned to that of dimer. The only significant transition observed in the solution state is at 410 nm under dilute conditions (Figure 3b). On concentrating the solution, two small humps were monitored at 550 nm and 685 nm alongside the saturating peak at 410 nm, confirming the presence of more than one-species in solution hence indicating the bond homolysis. As per Time-Dependent Density Functional Theory (TD-DFT) calculations, the transition from 410 nm is corresponding to the HOMO→LUMO transition of dimeric species, in which the peak at 680 nm is the SOMO→LUMO transition of the monomeric radical cation.

As in the case of [**1**]$_2$[OTf]$_4$, the radical's concentration was enhanced upon the addition of pyridine at the same 650 nm without any shift; the addition of pyridine to the [**2**]$_2$[OTf]$_4$ solutions led to the appearance of another new transition at 780 nm,

which decreased over time. The new transition is suspected because of the pyridine coordinated radical's SOMO→LUMO, which was also observed upon the addition of coordinating species to the concentrated solution of [**2**]$_2$[OTf]$_4$ (Figure 4).

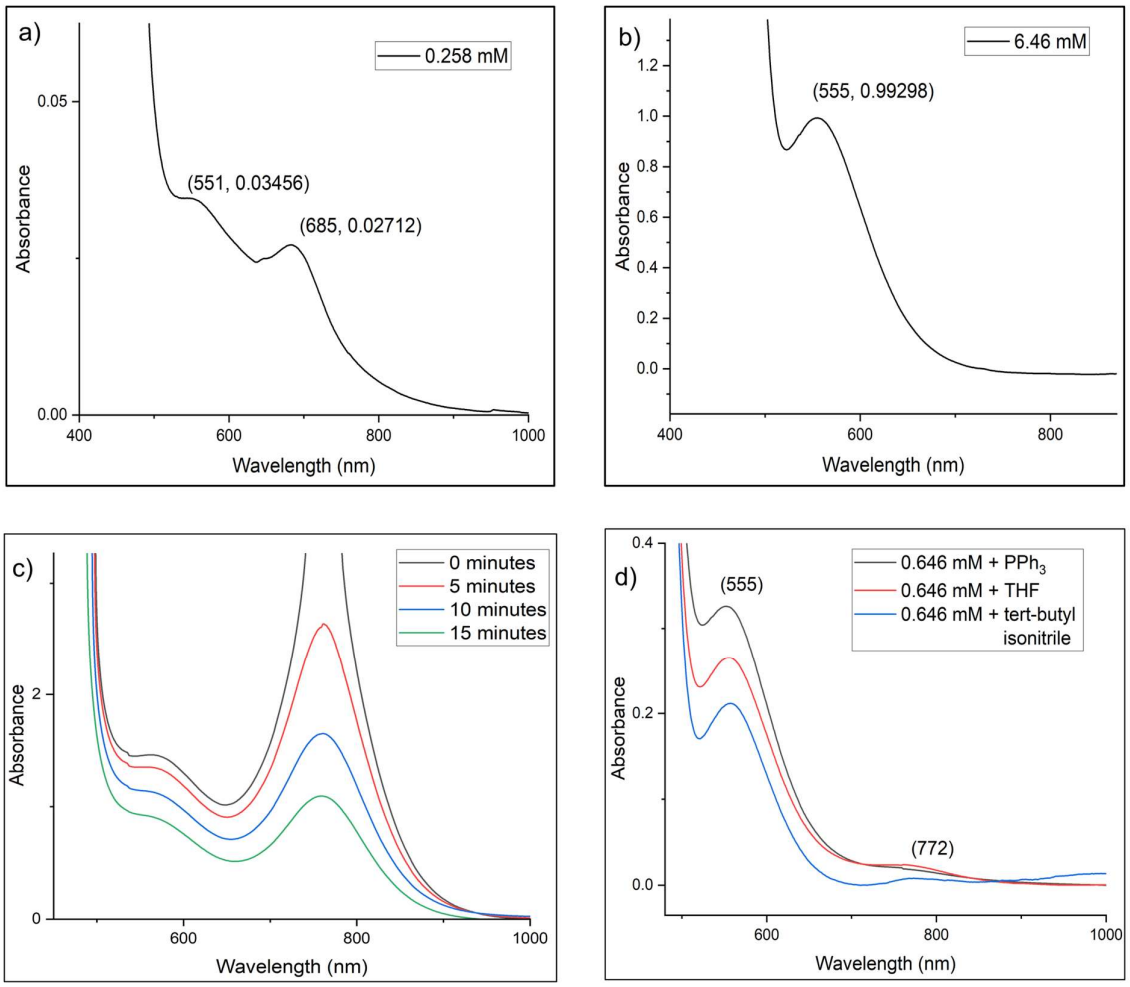

Figure 4: Varying concentration UV-Visible spectra in solution state. a) two small humps in dilute conditions; b) intense peak at 550 nm upon increasing concentration; c) pyridine addition leads to peak at 780 nm; d) donor-dependent study confirms the shifted peak at 780 nm.

Reactivity of [2]$_2$[OTf]$_4$:

From the NMR, EPR, and UV-Visible studies, the presence of multiple species in the solution after dissolving the crystals in acetonitrile is evident. Reactivity studies were carried out to check which species will be taking part in the reaction and whether there will be changes compared to the antimony analogue [**1**]$_2$[OTf]$_4$.

Radical Quench Reactivity:

Common reagents like Diphenyl dichalcogenides Ph_2Ch_2 (Ch = S, Se), p-benzoquinone, and TEMPO were taken, which are known in the literature to give

radicals in solution as well as from the reactivity observed for [**1**]$_2$[OTf]$_4$[19], to quench the radical that will be produced by the homolytic dissociation of [**2**]$_2$[OTf]$_4$.

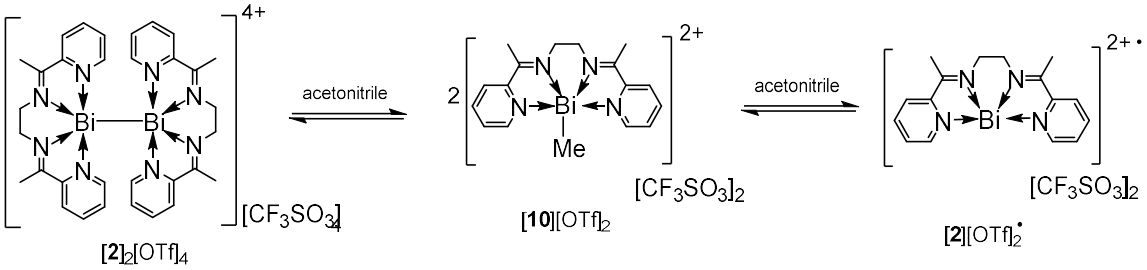

Scheme 6: Representation of possible species in the reaction medium.

[**2**]$_2$[OTf]$_4$ reacts with Ph_2S_2 and Ph_2Se_2 in acetonitrile medium at room temperature to give rise to the complexes [**3**][OTf]$_2$ and [**4**][OTf]$_2$ respectively. There are a handful of literature reports of Pn-Ch bonds[31] as well as one report by Litchenberg et al. of Ch-Ch bond in Ph2Ch2 breaking homolytically in solution to give rise to radicals, which reacts with bismuth radical to give Bi-SPh bond.[32] To the best of our knowledge [**3**][OTf]$_2$ and [**4**][OTf]$_2$ features first examples cationic Bi-Ch complexes. Light green color crystals of [**3**][OTf]$_2$ and bright yellow crystals of [**4**][OTf]$_2$ suitable for X-ray diffraction were grown in 60% and 62% yield, respectively, after filtering the acetonitrile solution to remove any metal precipitate and layering with diethyl ether kept at -30°C. Compounds [**3**][OTf]$_2$ and [**4**][OTf]$_2$ were characterized by multinuclear NMR spectroscopy in an acetonitrile medium (Figure 16-21).

The ^{19}F NMR gives a single peak at -80.26 ppm, indicating the equivalent chemical environment, hence free triflates in solution. For [**4**][OTf]$_2$, the ^{77}Se NMR gives a value of 303.29 ppm, much deshielded than the literature report of bismuth-organoselenide but in line with the corresponding antimony analogue.

Compound [**3**][OTf]$_2$ crystallizes in a monoclinic $P2_1/c$ space group (Table 1), with a mono-cationic [LBi(SPh)(OTf)] fragment and a free triflate counteranion, shows the inequivalent chemical environment in the solid state, in contrast to the solution. The coordinating triflate shows relatively stronger interaction with bismuth (Bi1-O1 = 2.726(5) Å), which is much shorter in comparison to the antimony analogue ((Sb1-O1 = 3.192(3) Å) but still longer than the sum of the covalent radii for bismuth and oxygen[34]. The bismuth center assumes a distorted pentagonal pyramidal geometry with the four coordinating nitrogens of the ligand and coordinating triflate in the distorted plane; the phenyl sulfide fragment occupies one of the axial sites, and the lone pair takes the second axial site. The Bi-S bond length of 2.550(1) Å is shorter

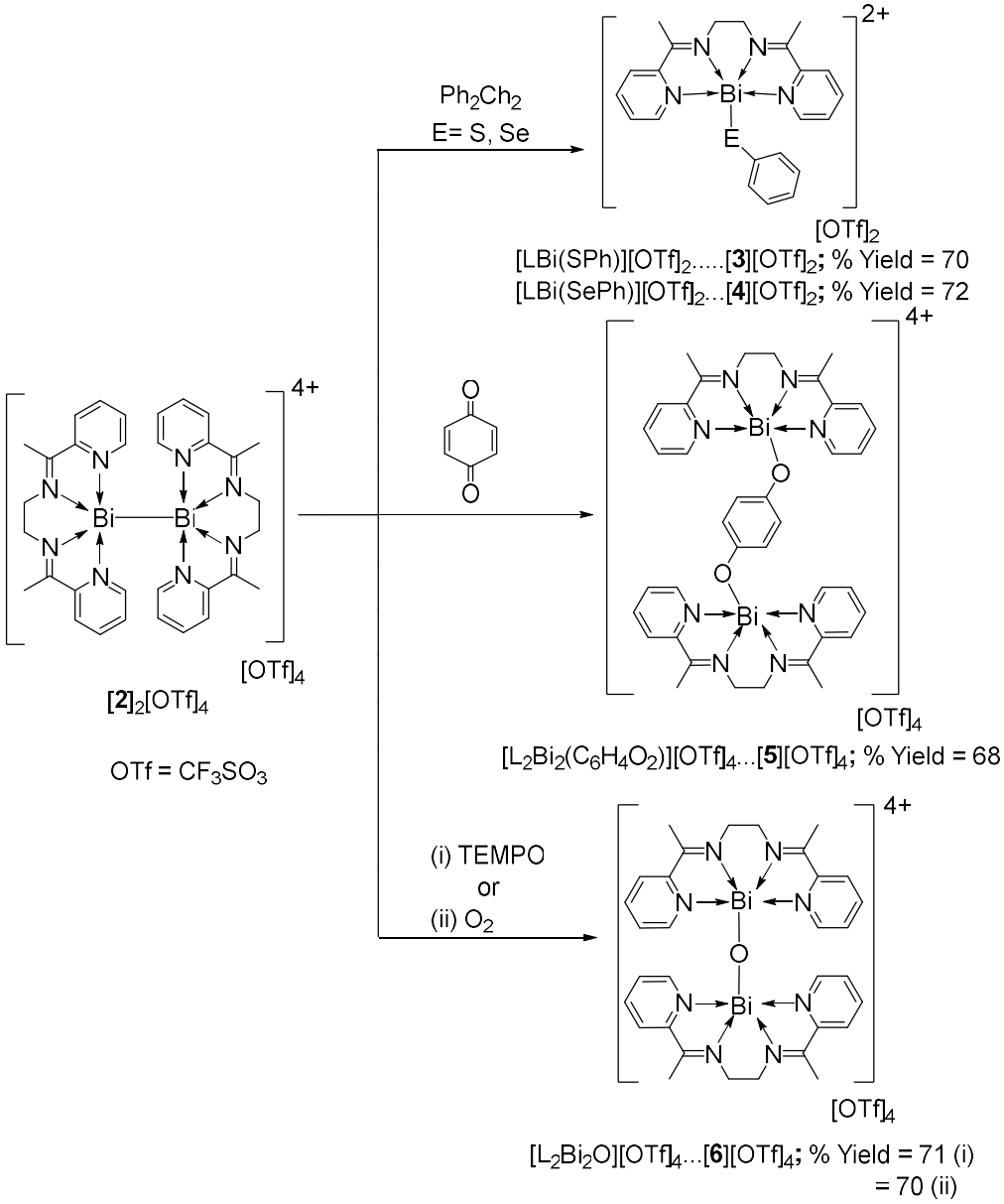

Scheme 7: Synthesis of complexes [**3**][OTf]$_2$-[**6**][OTf]$_4$.

than the literature reported Bi-S bonds[32] due to the stronger interaction between the cationic bismuth and nucleophilic sulfur center. The coordination bonds Bi-N_{im} averages 2.412(5) Å and Bi-N_{py} averages 2.550(5) Å.

Compound [**4**][OTf]$_2$ crystallizes in a triclinic *P*-1 space group (Table 2), with geometry and the coordinating environment closely resembling that of [**3**][OTf]$_2$. The Bi1-O1 bond length of 2.704(4) Å suggests strong coordination. The Bi1-Se1 bond length is estimated to be 2.6439(9) Å, relatively shorter than the literature reported ones[31] due to strong interaction between the electrophilic bismuth and nucleophilic organoselenide. The coordination bonds Bi-N_{im} averages to 2.422(5) Å and Bi-N_{py}

averages to 2.555(5) Å. Interestingly, the intermolecular Se-Se bond length of 3.3499(7) Å falls within the sum of Van der Waal's radii of both selenium atoms.[34]

[**2**]$_2$[OTf]$_4$ reacts with p-Benzoquinone in acetonitrile medium at room temperature to give rise to the complexes [**5**][OTf]$_4$ and some amount of [**10**][OTf]$_2$ as a side product. [**5**][OTf]$_4$ is the first bismuth-based p-Benzoquinone reactivity in literature. Dark red color crystals of [**5**][OTf]$_4$ suitable for X-ray diffraction were grown in 58% yield after the acetonitrile solution was filtered to remove any metal precipitate and layered with diethyl ether kept at -30°C. Regarding stability, [**5**][OTf]$_4$ is relatively stable in the solid state.

Compound [**5**][OTf]$_4$ crystallizes in a triclinic *P*-1 space group (Table 3), with a tetra-cationic [LBi-OC$_6$H$_4$O-BiL] fragment and four strongly coordinating triflate counteranions with Bi1-O$_{tf}$ bond lengths averages 2.803(5) Å, shows the larger diffuse orbitals in bismuth being able to accommodate all the triflates in the coordination sphere. The structure contains similar geometry as that of the antimony analogue.[19] The bismuth center assumes a distorted pentagonal bipyramidal geometry with the four coordinating nitrogens of the ligand and a coordinating triflate in the distorted plane, -OC$_6$H$_4$ fragment of p-Benzoquinone occupies one of the axial sites, and another coordinating triflate takes the second axial site. The Bi1-O9 = Bi2-O10 bond length of 2.096(5) Å is slightly shorter than the literature reported Bi-O bonds[35] due to the stronger interaction between the cationic bismuth and nucleophilic oxide center. The coordination bonds Bi-N$_{im}$ averages 2.398(7) Å and that of Bi-N$_{py}$ averages 2.560(7) Å.

TEMPO is generally known as a radical and typically shows the radical quench adduct formation. On reacting [**2**]$_2$[OTf]$_4$ with TEMPO in acetonitrile medium at low temperature, the dark yellow color faded to a bright yellow solution, giving rise to the complex [**6**][OTf]$_4$. The same can be achieved upon exposing the solution of [**2**]$_2$[OTf]$_4$ to air analogous to [**1**]$_2$[OTf]$_4$ case.[19] Along with [**6**][OTf]$_4$, varying amount of [**11**][OTf]$_4$ is also obtained as a side product. Other than [**1**]$_2$[OTf]$_4$, there is only one report of an oxide transfer reaction from the TEMPO radical by Tan and co-workers with an antimony(IV) radical cation.[17] Bright yellow crystals of [**6**][OTf]$_4$ suitable for X-ray diffraction were grown in 65% yield after the acetonitrile solution was filtered to remove any metal precipitate and layered with diethyl ether kept at -30°C. The compound [**6**][OTf]$_4$ has been studied by multi-nuclear NMR spectroscopy (Figure 22-24).

Compound [**6**][OTf]$_4$ crystallizes in a triclinic *P*-1 space group (Table 4), with a tetra-cationic [LBi-O-BiL] fragment and four strongly coordinating triflate counteranions with Bi1-O$_{tf}$ bond lengths average 2.822(9) Å, due to the larger diffuse orbitals in bismuth. The structure contains similar linear geometry as that of antimony analogue[19] the Bi1-O5-Bi2 = 170.3(9)° as opposed to the typical bent geometry of bridged oxo species in the literature. The bismuth center assumes a distorted pentagonal bipyramidal geometry with the four coordinating nitrogens of the ligand and a coordinating triflate in the distorted plane. The oxide fragment occupies one of the axial sites, and another coordinating triflate takes the second axial site. The Bi1-O5 and Bi2-O10 bond lengths of 1.983(1) Å and 1.942(2) Å, respectively, are slightly shorter than the literature reported Bi-O bonds[35] due to the stronger interaction between the cationic bismuth and nucleophilic oxide center. Thus, the [**6**][OTf]$_4$ can be better described as an oxide ion trapped between two tri-cationic bismuth centers.

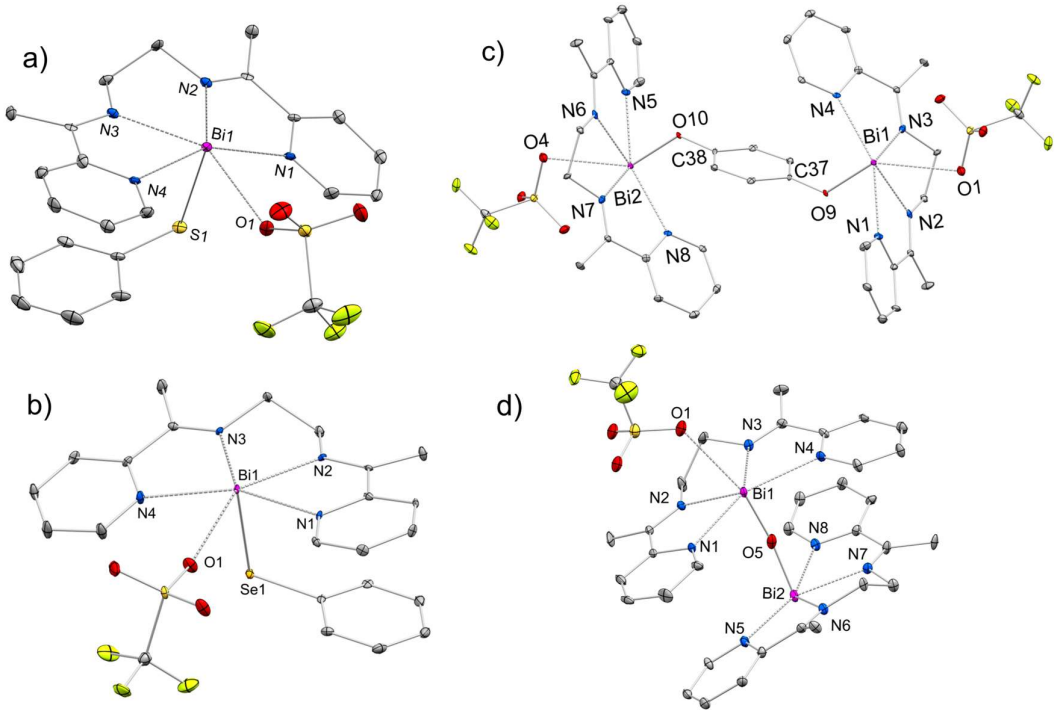

Figure 5: Molecular structure of the cationic part of a) [**3**][OTf]$_2$ b) [**4**][OTf]$_2$ c) [**5**][OTf]$_4$ and d) [**6**][OTf]$_4$ in the solid state (thermal ellipsoids at 30%, H atoms and counter anion is omitted for clarity). Selected bond lengths [Å]:a) Bi1-S1 = 2.550(1) Å, Bi1-N1 = 2.547(5) Å, Bi1-N2 = 2.413(6) Å, Bi1-N3 = 2.411(5) Å, Bi1-N4 = 2.560(5) Å, Bi1-O1 = 2.726(5) Å; b) Bi1-Se1 = 2.6439(9) Å, Bi1-N1 = 2.535(3) Å, Bi1-N2 = 2.382(3) Å, Bi1-N3 = 2.439(4) Å, Bi1-N4 = 2.596(5) Å, Bi1-O1 = 2.704(4) Å, Se1-Se1' = 3.3499(7) Å; c) Bi1-O9 = Bi2-O10 = 2.096(5) Å, Bi1-N1 = 2.542(6) Å, Bi1-N2 = 2.382(7) Å, Bi1-N3 = 2.415(7) Å, Bi1-N4 = 2.579(7) Å, Bi1-O9-C37 = 129.4(5)°, N1-N2-N3-N4 = 29.7(5)° and d) Bi1-O5 = 1.983(1) Å, Bi2-O5 = 1.942(2) Å, Bi1-O1 = 2.822(9) Å, Bi1-O5-Bi2 = 170.3(9)°, N1-N2-N3-N4 = -23(1)°

Transition-Metal Based Reactivity:

As seen from the redox reactivity with various transition metal precursors for [**1**]$_2$[OTf]$_4$ by bond homolysis, the possibility of exchange reactions with transition metal-based dimers with [**2**]$_2$[OTf]$_4$ emerged. Three dimers, i.e., dicobalt octacarbonyl, dimanganese decacarbonyl, and Bis(cyclopentadienyl) diirion tetracarbonyl, were chosen to attain the goal. However, various literature reports and reactivity studies of compounds show that transition metal complexes can exhibit many canonical structures in solution via several types of rearrangements.[37] Similarly, there are claims that all three transition metal-based dimers have TM-TM bonds and propositions that they do not have direct TM-TM but instead bridging carbonyls.[38] Thus, reacting our tetracationic dimers with these dimers can show how they behave when reacting to cationic radical species.

The reaction of [**2**]$_2$[OTf]$_4$ with dicobalt octacarbonyl led to an immediate color change of the solution from yellow to red, leading to the formation of [**7**][OTf]$_3$, along with the [LBiCo(CO)$_4$][OTf]$_2$ complex. Red crystals of [**7**][OTf]$_3$ suitable for X-ray diffraction were grown in 64% yield after the acetonitrile solution was filtered to remove any metal precipitate and layered with diethyl ether kept at -30°C. Multinuclear NMR spectroscopy was performed on the obtained crystals mixture, revealing the presence of two carbonyl species in $^{13}C\{^1H\}$. The in-situ NMR study reveals the presence of multiple carbonyl species in the solution as per $^{13}C\{^1H\}$ and cobalt(I) coordinated acetonitrile species as per ^1H NMR (Figure 25-27).

Compound [**7**][OTf]$_3$ crystallizes in orthorhombic $P2_12_12_1$ space group (Table 5), with the asymmetric unit containing cationic [LBi(OTf)-Co(CO)$_3$-Bi(OTf)L] fragment, one free triflate anion and two acetonitrile molecules. Analogous to the antimony's case, the cobalt center assumes a trigonal bipyramidal geometry, with three carbonyls in the equatorial position and two Bi(I) centers occupying the axial sites. The Bi-Co bond length averages to 2.605(6) Å. The bismuth centers assume distorted pentagonal pyramidal geometry with the four nitrogens with a triflate occupying the distorted plane and the cationic -Co(CO)3 taking the axial site. In terms of bonding parameters, [**7**][OTf]$_3$ is similar to that of the [**LSb-Co(CO)$_3$-SbL**][OTf]$_3$ (see appendix) and bismuthinidene coordinated Co(CO)$_3$ cation reported by Dostal et al. [39], indicating a redox mechanism as observed for [**7**][OTf]$_3$ (Figure 34). However, the [LBiCo(CO)$_4$][OTf]$_2$ crystallizes in a monoclinic $C2/c$ space group (Table 6), and the asymmetric unit consists of the dicationic [LBi-Co(CO)$_4$] fragment with the bismuth

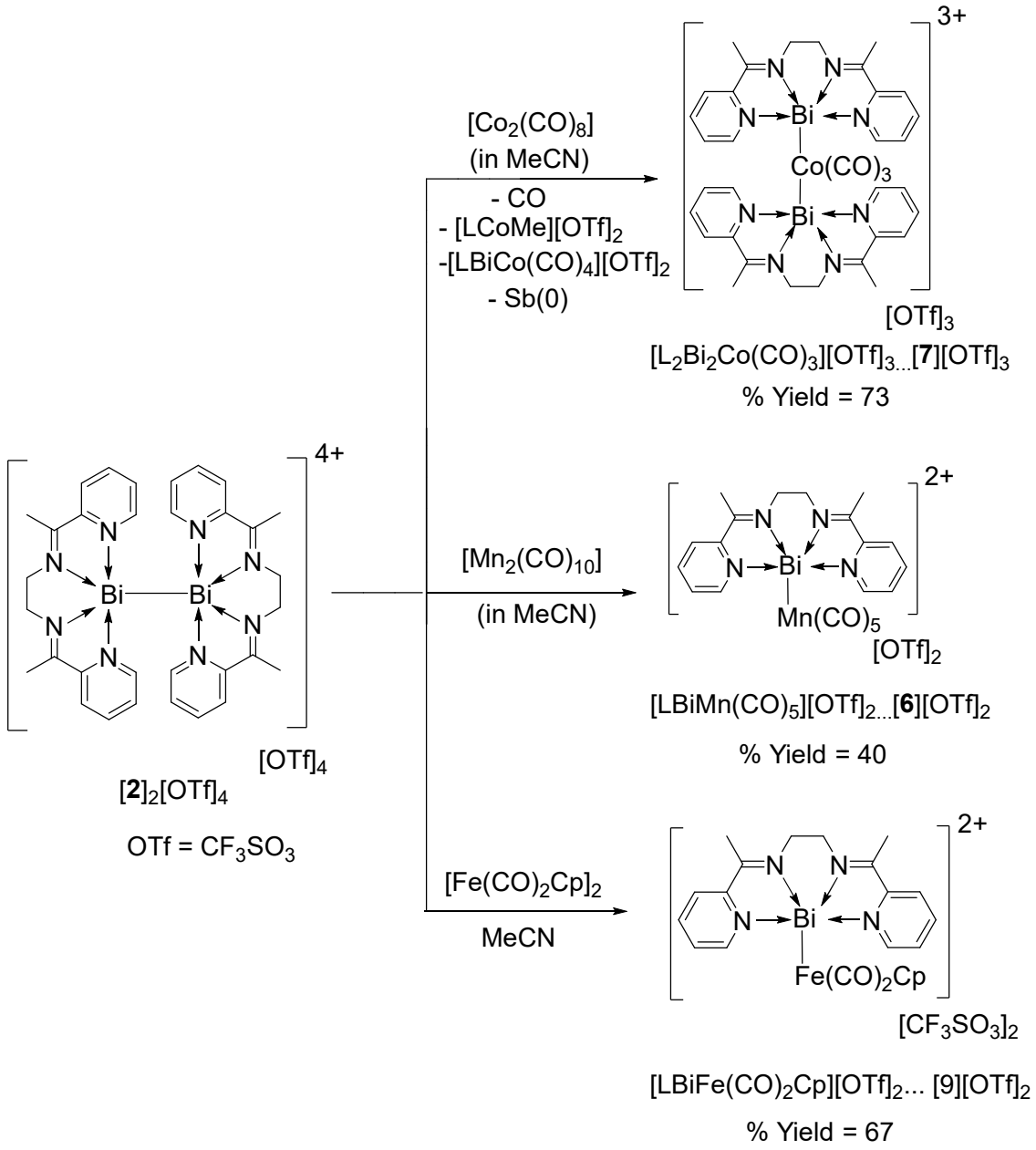

Scheme 8: Synthesis of complexes [**7**][OTf]$_3$-[**9**][OTf]$_2$.

center firmly coordinated by the two triflate counteranions with the Bi-O_{tf} bond averaging to 2.725(4) Å. The cobalt center assumes a trigonal bipyramidal geometry with three carbonyls in the equatorial position, the fourth carbonyl, and the bismuth occupying the axial site. The bismuth center assumes a pentagonal bipyramidal geometry with the Ligand's nitrogen and one triflate taking the distorted plane with the other triflate and -Co(CO)$_4$ taking the axial sites. The Bi-Co bond length is estimated to be 2.711(2) Å, which is elongated as compared to [**7**][OTf]$_3$. This structure seems similar to that of **int-4** (Figure 34), can be regarded as an isolated intermediate. However, the presence of dicationic charge and a -Co(CO)$_4$ fragment also indicates

possible exchange events simultaneously.

In the light of differing reactivity for [**2**]$_2$[OTf]$_4$ as compared to [**1**]$_2$[OTf]$_4$ with dicobalt octacarbonyl, the reaction of [**2**]$_2$[OTf]$_4$ with dimanganese decacarbonyl was performed under the same conditions as the formation of [**LSb-Mn(CO)$_5$**][OTf]$_2$ at room temperature, leading to a slower reaction rate and longer reaction time giving rise to complex [**8**][OTf]$_2$ by the cleavage of the strong Mn-Mn[40], along with the formation of [**10**][OTf]$_2$. Light yellow crystals of [**8**][OTf]$_2$ suitable for X-ray diffraction were grown in 40% yield after the acetonitrile solution was filtered to remove any metal precipitate and layered with diethyl ether kept at -30°C. Unlike the case of [**LSb-Mn(CO)$_5$**][OTf]$_2$, [**8**][OTf]$_2$ also shows relative stability to temperature.

Compound [**8**][OTf]$_2$ crystallizes in the triclinic *P*-1 space group (Table 7) with the cationic [LBiMn(CO)$_5$(OTf)] fragment and a free triflate anion in the asymmetric unit. The Bi-Mn bond length estimates to 2.773(1) Å with the manganese center assuming an octahedral geometry and the bismuth center assuming a distorted pentagonal pyramidal geometry, with the ligand's coordinating nitrogen with the one triflate anion taking the distorted plane and -Mn(CO)$_5$ taking the axial site. The compound's geometry and bonding can be compared with the neutral Bi-Mn(CO)$_5$ complex reported by Lichtenberg and co-workers.[41]

The room temperature reaction of [**2**]$_2$[OTf]$_4$ and Bis(cyclopentadienyl) diirion tetracarbonyl, [Fe(CO)$_2$Cp]$_2$ in acetonitrile led to the immediate color change from yellow to bright red with the formation of [**9**][OTf]$_2$ along with the formation of [**11**][OTf]$_4$. Bright red crystals of [**9**][OTf]$_2$ suitable for X-ray diffraction were grown in 67% yield after filtering the acetonitrile solution to remove any metal precipitate and layering with diethyl ether kept at -30°C. The solution state characterization of [**9**][OTf]$_2$ by multinuclear NMR spectroscopy resulted in the appearance of carbonyl signal at 198 ppm in $^{13}C\{^1H\}$ and two sets of ligand peaks in both 1H and $^{13}C\{^1H\}$, one for [**9**][OTf]$_2$ and the second one for [**11**][OTf]$_2$ (Figure 28-30).

Compound [**9**][OTf]$_2$ crystallizes in triclinic *P*-1 space group (Table 8) with the cationic [LBiFe(CO)$_2$Cp(OTf)] fragment and a free triflate anion in the asymmetric unit. The Bi-Fe bond length estimates to 2.635(2) Å with the iron centre assuming a three legged piano-stool geometry and the bismuth centre assuming a distorted pentagonal pyramidal geometry, with the ligand's coordinating nitrogen with the one triflate anion taking the distorted plane and -Fe(CO)$_2$Cp taking the axial site. From the structure, the cyclopentadienyl ring has η^5-coordination to the iron center. The compound's

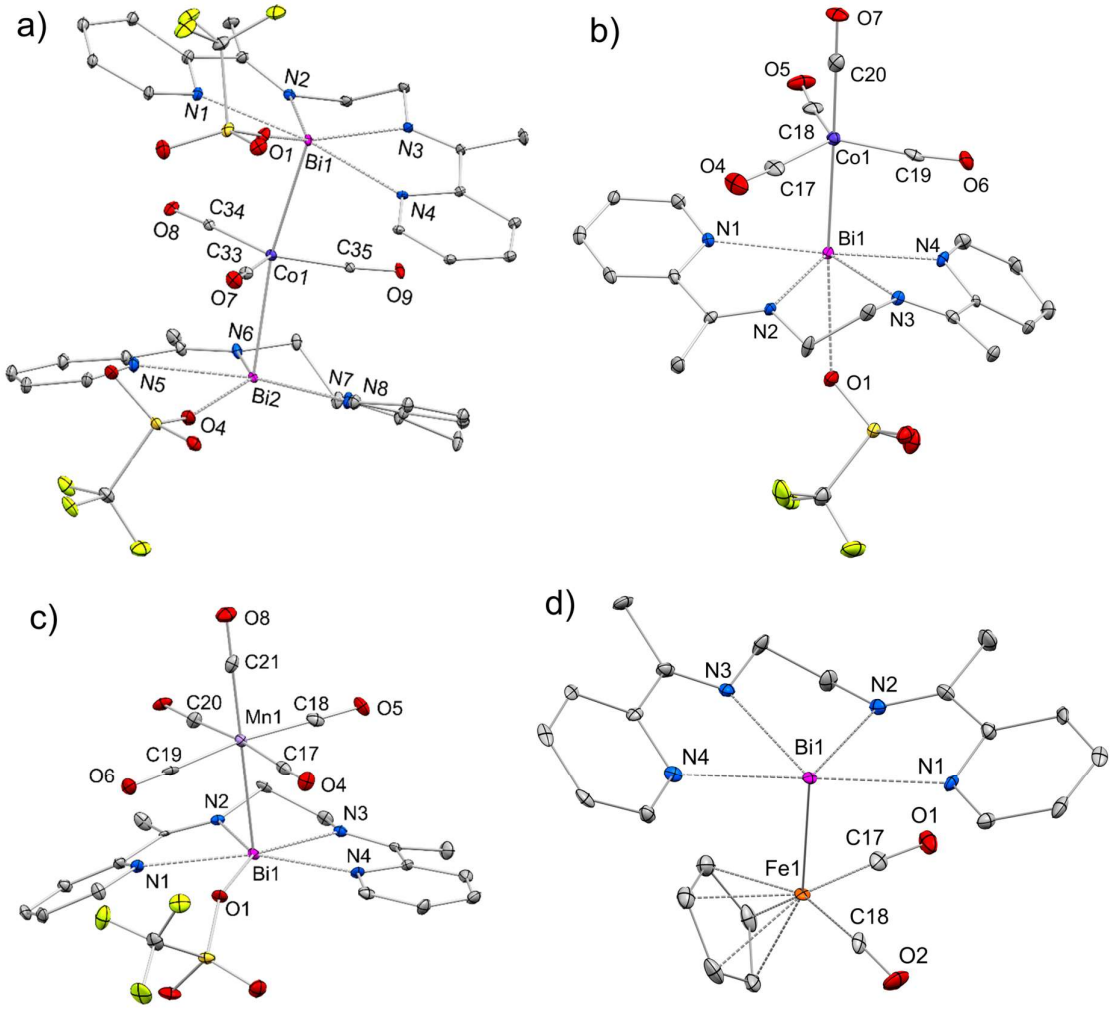

Figure 6: Molecular structure of the cationic part of a) [**7**][OTf]$_3$, b) [LBiCo(CO)$_4$][OTf]$_2$ c) [**8**][OTf]$_2$ and d) [**9**][OTf]$_2$ in the solid state (thermal ellipsoids at 30%, H atoms and counter anions are omitted for clarity). Selected bond lengths [Å]: a) Bi1-Co1= 2.646(5) Å, Bi2-Co1= 2.637(5) Å, C≡O = 1.13-1.15(2) Å, Bi1-O1 = 2.79(1), Bi2-O4 = 2.82(1), N1-N2-N3-N4 = -27.6(7), N5-N6-N7-N8 = 18.9 (6); b) Bi1-Co1 = 2.711(2) Å, Bi1-O1 = 2.908(6) Å, C≡O = 1.13-1.14(1) Å, N1-N2-N3-N4 = -23.2(4); c) Bi1-Mn1 = 2.785(2) Å , Bi1-O1 = 2.711(6) Å, C≡O = 1.12-1.15(1) Å, N1-N2-N3-N4 = -8.3(4); and d) Bi1-Fe1 = 2.635(2) Å, Fe1-Cp = 2.07-2.11(2) Å, C≡O = 1.15-1.16(3) Å, N1-N2-N3-N4 = -11.0(9).

geometry and bonding can be compared with the neutral Bi-Fe(CO)$_2$Cp complex reported by Lichtenberg and co-workers.[41]

Activation Reactions:

The complex [**2**]$_2$[OTf]$_4$ activates the C-C bond in acetonitrile (CH_3CN) to give the complex [**10**][OTf]$_2$, which appears as a side product in many of the reactivities mentioned above. This activation step is not observed in the case of [**1**]$_2$[OTf]$_4$. It is C-C single bond activation, which is remarkable as there are reports of C-H and C≡N bond activations[42,43]. Still, very few literature reported C-C bond cleavage of

acetonitrile.[44] Attempts to understand the mechanism behind this activation along with the isolation of the side products are being made.

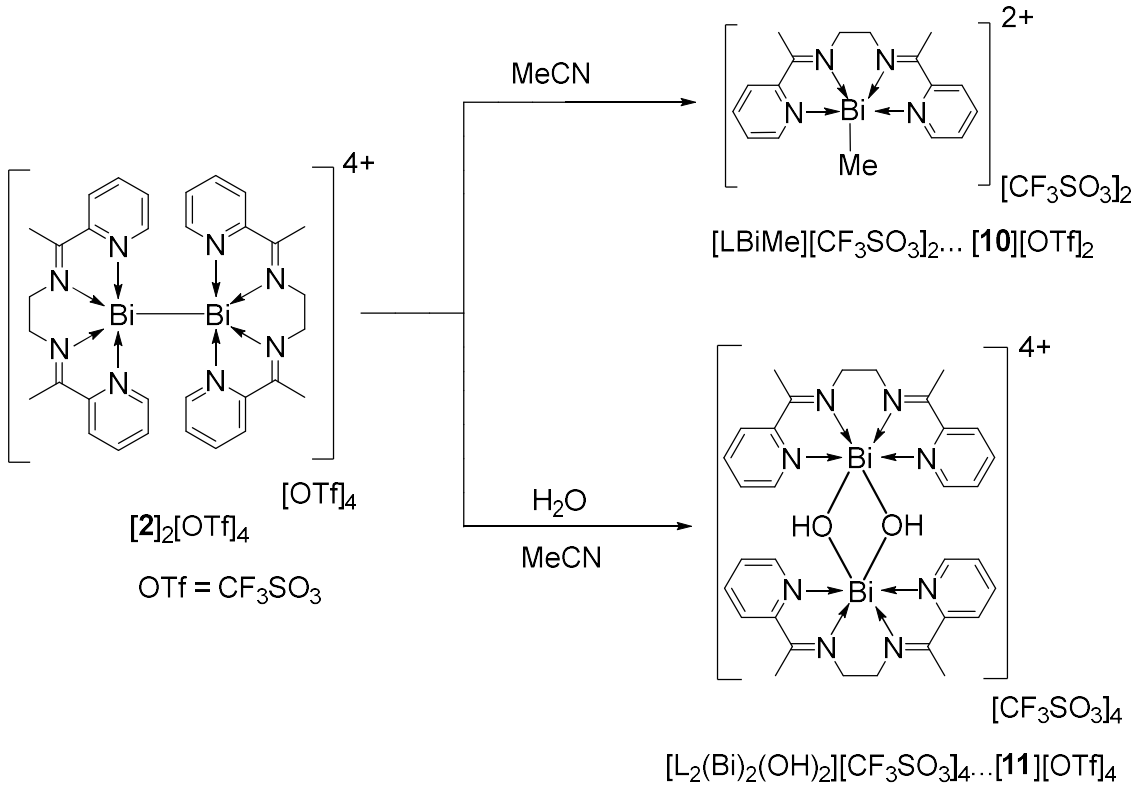

Scheme 9: Synthesis of complexes [**10**][OTf]$_2$ and [**11**][OTf]$_4$.

Colorless crystals of [**10**][OTf]$_2$ suitable for X-ray diffraction were grown, and compound [**10**][OTf]$_2$ crystallized in a monoclinic *C*2/*c* space group (Table 9). The asymmetric unit consists of the cationic [LBi(CH$_3$)(OTf)] fragment with a free triflate anion. The bismuth center takes a distorted pentagonal pyramidal geometry with the ligand's nitrogen, with the triflate taking the distorted plane and the methyl group occupying the axial site. The triflate coordination to the bismuth center is strong, with a Bi-O$_{Tf}$ bond length of 2.710(3) Å. The Bi-CH$_3$ bond length of 2.233(5) Å is comparable to literature examples of Bi-Me bonds.[33]

The complex [**2**]$_2$[OTf]$_4$ also activates the O-H bond of water (H$_2$O) in acetonitrile medium to give rise to complex [**11**][OTf]$_4$. This species also appears in several activations, as the bismuth triflate contains some water that cannot be excluded. Colorless crystals of [**11**][OTf]$_4$ suitable for X-ray diffraction were grown in 70% yield after the acetonitrile solution was filtered to remove any metal precipitate and layered with diethyl ether kept at -30°C. Further characterization by multinuclear NMR spectroscopy has been done (31-33).

compound [**11**][OTf]$_4$ crystallizes in a triclinic *P*-1 space group (Table 10). The asymmetric unit comprises a tetracationic [LBi-(μ-OH$_2$)-BiL] fragment with four coordinating triflate anions. The bismuth center takes a geometry with the ligand's nitrogen, with one of the triflate taking the distorted plane and the other triflate and -OH groups occupying a plane axial to the distorted one. The triflate coordination to the bismuth center is strong, with a Bi-O$_{Tf}$ bond length of 2.810(5) Å. The Bi1-O1 bond length of 2.127(3) Å and Bi2-O1 bond length of 2.378(4) Å, is comparable to literature examples of Bi-(μ-OH$_2$)-Bi moieties.[45,46]

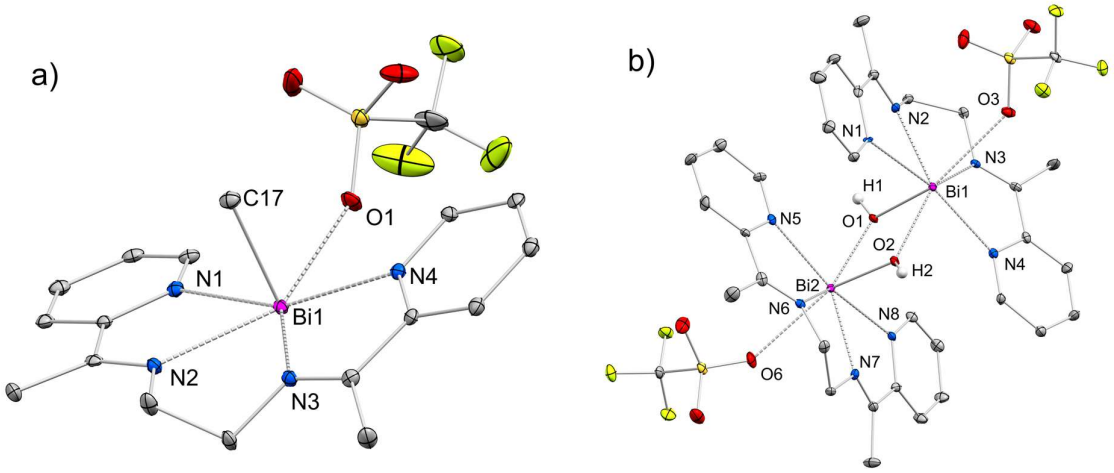

Figure 7: Molecular structure of the cationic parts of a) [**10**][OTf]$_2$ and b) [**11**][OTf]$_4$ in the solid state (thermal ellipsoids at 30%, H atoms and counter anion is omitted for clarity). Selected bond lengths [Å]: Bi1-C17 = 2.236(7) Å, Bi1- O1 = 2.711(4) Å, N1-N2-N3-N4 = 20.7(3); b) Bi1-O1 = 2.125(6) Å , Bi1-O2 = 2.378(4) Å, Bi1-O3 = 2.817(5) Å, Bi1-O1-Bi2 = 113.4(2)°, N1-N2-N3-N4 = 15.7(4)°.

Chapter 4 Conclusion

This study records a detailed characterization of the novel tetracationic dibismuthane [**2**]$_2$[OTf]$_4$ in both solid and solution state. [**2**]$_2$[OTf]$_4$ shows differing extent of monomeric dicationic radical [**2**][OTf]$_2^{\bullet}$ and tetracationic dimer [**2**]$_2$[OTf]$_4$ equilibrium established from detailed NMR spectroscopy and UV-Visible spectroscopy as compared to [**1**]$_2$[OTf]$_4$. The detection of this monomeric radical [**2**][OTf]$_2^{\bullet}$ was done by DOSY NMR Spectroscopy and EPR Spectroscopy. The significant localization of positive charges on dimer and unpaired spin density on the monomeric bismuth centre is backed by computations findings. The confirmation of the radical localization on bismuth centre by the radical quench reactions with diphenyl dichalogenides and p-Benzoquinone led to formation of diamagnetic complexes [**3**][OTf]$_2$, [**4**][OTf]$_2$, and [**5**][OTf]$_4$. Reaction of [**2**]$_2$[OTf]$_4$ with TEMPO or exposure to oxygen leads to an oxo transfer reaction giving rise to [**6**][OTf]$_4$, with unprecedented linear Bi-O-Bi motif. Furthermore, Reaction of [**2**]$_2$[OTf]$_4$ dimer with transition metal carbonyls containg intermetallic bonds led to heterobimetallic complexes. While [**2**]$_2$[OTf]$_4$ shows redox chemistry with $Co_2(CO)_8$ with the formation of [**7**][OTf]$_3$, $Mn_2(CO)_{10}$ and $[FeCp(CO)_2]_2$ shows exchange reactions to form [**2**][OTf]$_2$ and [**2**][OTf]$_2$ respectively. Observation of [**10**][OTf]$_2$, upon rare C-C bond activation of acetonitrile and [**11**][OTf]$_4$ from O-H bond of water by [**2**]$_2$[OTf]$_4$ showcases the potential for further small molecule activations

Additional Experiments Performed

Synthesis of [$L_2Sb_2Co(CO)_3$][OTf]$_3$ [7][OTf]$_3$. Dicobalt octacarbonyl (0.010 g, 0.03 mmol) was added to a solution of [**1**]$_2$[OTf]$_4$ (0.040 g, 0.03 mmol) in 10 mL acetonitrile. The resulting dark brown solution was stirred at ambient temperature for 6 hours. Then the reaction mixture was concentrated to 5 mL. Reddish brown single crystals of [$\mathbf{L_2Sb_2Co(CO)_3}$][OTf]$_3$ were obtained from this concentrated solution layered with diethyl ether maintained at -30^{o}C in 73% yield (0.03 g). Decomp. of [$\mathbf{L_2Sb_2Co(CO)_3}$][OTf]$_3$: >200 ^{o}C

^{1}H NMR (400 MHz, CD_3CN, 298 K) δ 8.99 (d, *J* = 4.8, 2H, *o*-Pyr-*H*); 8.38 (d, *J* = 8.0, 2H, *m*-Pyr-*H*); 8.25 (td, *J* = 7.9, 1.4, 2H, *m*-Pyr-*H*); 7.75 (dd, *J* = 7.1, 5.2, 2H, *p*-Pyr-*H*); 4.42-4.28 (m, 2H, -CH_2-CH_2−); 4.19-3.94 (m, 2H, -CH_2-CH_2−); 2.83 (s, 6H, -CH_3) ppm.

^{13}C{^{1}H} NMR (101 MHz, CD_3CN, 298 K) δ 200.20 (Co-*C*O); 174.36 (*C*=N); 148.26 (Pyr-C_i); 147.00 (Pyr-C_o); 140.93 (Pyr-C_p); 128.25 (Pyr-C_m); 127.92 (Pyr-C_m); 50.05 (−*C*H_2-*C*H_2−); 19.19 (−*C*H_3) ppm.

^{19}F{^{1}H} NMR (377 MHz, CD_3CN, 298 K) δ -78.73 (s) ppm.

UV/Vis (acetonitrile) λ_{max} (ε) 478 nm (ε =11860 $M^{-1}cm^{-1}$), 415 nm (ε = 8490 $M^{-1}cm^{-1}$).

MALDI-TOF (CD Matrix): Observed m/z = 682.4116 (calculated m/z= 682.4475) [($L_2Sb_2Co(CO)_3$)(CF_3SO_3)$_3$(H^+)$_2$]$^{2+}$

Synthesis of [LSbMn(CO)$_5$)][OTf]$_2$ [8][OTf]$_2$: One drop of pyridine was added to a solution of [**1**]$_2$[OTf]$_4$ (0.040 g, 0.03 mmol) in 10 mL acetonitrile. To the resulting blue solution, $Mn_2(CO)_{10}$ (0.011 g, 0.03 mmol) was added and stirred at ambient temperature for 3 days period. The reddish orange solution obtained was filtered to remove the black metal precipitate formed during the reaction. The filtrate was evaporated to get a crude reddish solid. Orange colored single crystals of [**8**][OTf]$_2$ were obtained by dissolving the crude solid in tetrahydrofuran solvent and layering with pentane, maintained at -30 ˚C in 31% yield (0.002 g). Decomp. of [**8**][OTf]$_2$: 30 ^{o}C

^{1}H NMR (600 MHz, CD_3CN, 268 K) δ 9.46-9.45 (m, 2H, *o*-Pyr-*H*); 8.54-8.51 (m, 2H, *m*-Pyr-*H*); 8.36-8.34 (m, 2H, *m*-Pyr-*H*); 7.92-7.90 (m, 2H, *p*-Pyr-*H*); 4.49-4.34 (m, 4H, -CH_2-CH_2−); 2.95 (s, 6H, -CH_3) ppm.

^{13}C{^{1}H} NMR (101 MHz, CD_3CN, 268 K) δ 209.41 (*C*≡O); 176.79 (*C*=N); 149.88 (Pyr-C_i); 149.13 (Pyr-C_o); 141.73 (Pyr-C_p); 129.31 (Pyr-C_m); 128.96 (Pyr-C_m); 121.76 (q, *J* = 320 Hz, CF_3SO_3); 50.66 (−*C*H_2-*C*H_2−); 25.96 (−*C*H_3) ppm.

^{19}F{^{1}H} NMR (377 MHz, CD_3CN, 268 K) δ -80.26 (s) ppm.

MALDI-TOF (CHCA Matrix): Observed m/z = 389.5006 (calculated m/z= 389.5009) $[(LSbMn(CO)_5)(CF_3SO_3)(CH_3CN)(H^+)_4(H^-)_3]^{2+}$

The reaction of $[\mathbf{1}]_2[OTf]_4$ with dicobalt octacarbonyl ($Co_2(CO)_8$) in acetonitrile medium at room temperature gave rise to the complexes [Sb**Co**][OTf]$_3$ and some amount of [LCo][OTf]$_2$ as a side product. So, a redox reaction took place instead of a clean exchange reaction. During the reaction, some amount of Sb(0) precipitated, indicating the reduction of antimony, possibly from the oxidation of cobalt(I) to Co(II) and the release of carbonyls with the coordination by the free ligand due to Sb(0) fall out. Reddish-brown crystals of [Sb**Co**][OTf]$_3$ suitable for X-ray diffraction were grown in 73% yield after the acetonitrile solution was filtered to remove any metal precipitate and layered with diethyl ether kept at -30°C. The solution state properties were studied by multinuclear NMR spectroscopy and UV-Visible spectroscopy. ^{1}H NMR of isolated crystals of [Sb**Co**][OTf]$_3$ gives one set of downfield shifted ligand peaks along with a few broad peaks centered around 15 ppm, which is the characteristic peak of Co(I)

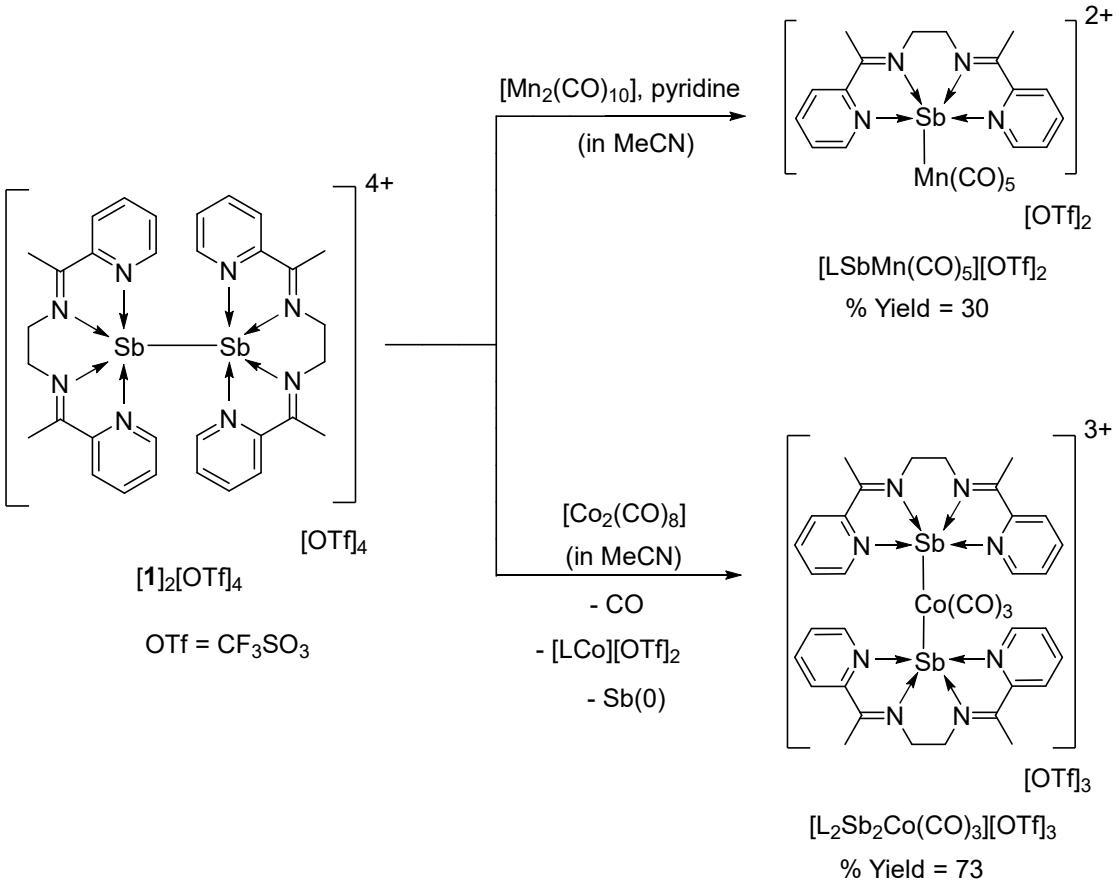

Scheme 10: Synthesis of complexes [**LSb-Co(CO)$_3$-SbL**][OTf]$_3$ and [**LSb-Mn(CO)$_5$**][OTf]$_2$.

coordinated acetonitrile. $^{13}C\{^{1}H\}$ gives the carbonyl peaks at 200.20 ppm with a broad acetonitrile solvent peak, which is assumed because of solvent coordination. The infrared spectroscopy revealed the carbonyl stretching at 2085.95, 2013.78, and 1941.37 cm^{-1}. The absorbance measurements led to two transitions in the visible range, one at 478 nm (ε =11860 $M^{-1}cm^{-1}$) and the other at 415 nm (ε = 8490 $M^{-1}cm^{-1}$). The 478 nm transition is assigned to the 515 nm transition due to HOMO→LUMO, and the 415 nm transition is assigned to the 435 nm transition due to HOMO-1→LUMO as predicted from TD-DFT calculations.

Compound [Sb**Co**][OTf]$_3$ crystallizes in a triclinic *P*-1 space group with two tricationic [LSb-Co(CO)3-SbL] fragments with six non-coordinating triflate anions in the vicinity. In terms of geometry, the structure resembles that of Dostal et al.'s stibinidene coordinated $Co(CO)_3$ cationic unit.[39] The Sb-Co bond lengths average to 2.544(5) Å. The central cobalt(I) assumes a trigonal bipyramidal geometry with three carbonyls occupying the equatorial position and the two axial sites occupied by the cationic stibinidene units. In terms of mechanism, the most energetically favorable one is the dissociation of $Co_2(CO)_8$ to $Co(CO)_4^+$ and $Co(CO)_4^-$ as well the dissociation of [**1**]$_2$[OTf]$_4$ to monomeric radical species [**1**][OTf]$_2^{\bullet}$ followed by one-electron reduction of the Sb(II) centers by the $Co(CO)_4^-$ fragment to get oxidized to $Co(Co)_4^+$, which gets inserted between the two antimony centers with the release of a carbonyl and forming a 18$\overline{e}$ complex. The computational findings show that the Wiberg bond order of Sb-Co bonds is 0.64, indicating an intermediate between purely covalent and purely dative bonds.

The reaction between [**1**]$_2$[OTf]$_4$ and dimanganese decacarbonyl ($Mn_2(CO)_{10}$) in acetonitrile medium at room temperature gives rise to the complexes [Sb**Mn**][OTf]$_2$. The reaction is energy-demanding as the Mn-Mn bond is very strong and, as per literature, requires energy to break, either in the form of light or heat.[40] A small amount of pyridine is added to assist the Mn-Mn bond cleavage by forming a 19$\overline{e}$ paramagnetic complex, $Mn(CO)_5(Py)^{\bullet}$. This in-situ formed complex has been observed by EPR experiments, which reacts with the radical species [**1**][OTf]$_2^{\bullet}$ with the elimination of pyridine to give the exchange product [Sb**Mn**][OTf]$_2$. Orange crystals of [Sb**Mn**][OTf]$_2$ suitable for X-ray diffraction were grown in 31% yield after the acetonitrile solution was filtered to remove any metal precipitate and layered with diethyl ether kept at -30°C. [Sb**Mn**][OTf]$_2$ has been characterized by multinuclear NMR experiments, showing the carbonyl peaks at 209.41 ppm, confirmed by the FT-IR data giving peaks at 2106,

2011, and 1939 cm^{-1}. The absorbance study for this compound was hindered by the limited stability at room temperature upon dissolution.

Compound [Sb**Mn**][OTf]$_2$ crystallizes in a triclinic *P*-1 space group with the cationic [LSbMn(CO)$_5$(OTf)] fragment and a free triflate anion. The antimony center assumes a distorted pentagonal pyramidal geometry with the four coordinating nitrogen of the ligand and the coordinating triflate occupying the distorted plane, and the Mn(CO)5 fragment takes the axial position. The Sb-Mn bond length is 2.7234(8) Å which is elongated than the literature reported ones[47] due to steric clash with the bulky ligand **L**. Further, the Natural Bonding Orbital analysis shows the bonding parameters resemble that reported by Dostal et al., with a Wiberg bond order of 0.65, indicating the partial dative nature of the bond despite having a bonding orbital for Sb-Mn covalent bond.

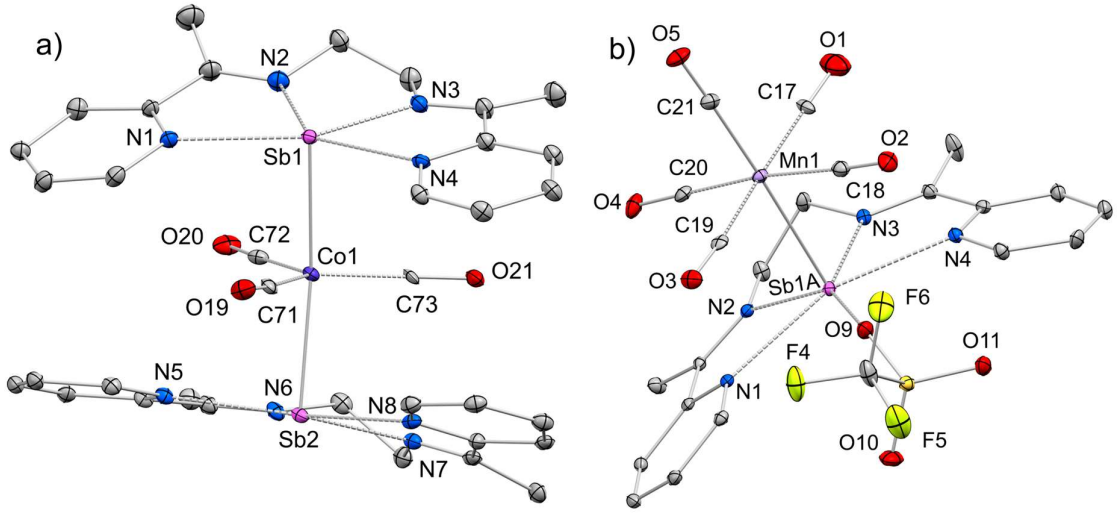

Figure 8: Molecular structure of the cationic parts of a) [**LSb-Co(CO)$_3$-SbL**][OTf]$_3$ and b) [**LSbMn(CO)$_5$**][OTf]$_2$ in the solid state (thermal ellipsoids at 30%, H atoms and counter anions are omitted for clarity). The Sb atom in [**LSbMn(CO)$_5$**][OTf]$_2$ has 85:15 partial occupancies. Selected bond lengths [Å] and angles [°]: a) Sb1-Co1 = 2.554(4), Sb2-Co1 = 2.534(3), Sb1-N1 = 2.569(16), Sb1-N2 = 2.318(16), Sb1-N3 = 2.256(17), Sb1-N4 = 2.489(16), Sb2-N5 = 2.530(16), Sb2-N6 = 2.238(17), Sb2-N7 = 2.283(18), Sb2-N8 = 2.567(16); Sb1-Co1-Sb2 = 170.58(13); b) Sb1A-Mn1 = 2.723(1), Sb1A-N1 = 2.590(5), Sb1A-N2 = 2.306(4), Sb1A-N3 = 2.258(5), Sb1A-N4 = 2.488(4), Sb1A···O9 = 2.981(5).

Achievements During MS-Thesis:

- During, my thesis work I have worked significantly on the manuscript titled “Tetra-Cationic Distibane Stabilized by Bis(α-iminopyridine) and Its Reactivity” (please find below) and performed its under-revision assignments. During this time, I have spent time in the manuscript formulation, data collection and data analysis for the compounds mentioned in the manuscript.

  ‘Tetra-cationic Distibane stabilized by Bis(alpha-iminopyridine) and its Reactivity’ Hritwik Haldar, **Satyabrata Das**, Haakon T. A. Wiedemann, Katrin Beuthert, Christopher W. M. Kay, Stefanie Dehnen, Cem B. Yildiz* and Moumita Majumdar*, *J. Am. Chem. Soc*. **2025**, *147*, 3140-3151.

- I have presented my thesis work at the 2nd International conference of Main-Group Synthesis and Catalysis (ICMGSC 2025) at IISER Thiruvananthapuram and received ***Dalton Transactions*** **Best Poster Award**. (13-16 February, 2025).

References

1. Reactivity of Transition Metal Complexes with Small Molecules. In *Inorganic Electrochemistry Theory, Practice and Application*; The Royal Society of Chemistry, 2011; pp 420–480. https://doi.org/10.1039/BK9781849730716-00420.
2. Valdés, H.; Germán-Acacio, J. M.; Koten, G. van; Morales-Morales, D. Bimetallic Complexes That Merge Metallocene and Pincer-Metal Building Blocks: Synthesis, Stereochemistry and Catalytic Reactivity. *Dalton Trans.* **2022**, *51* (5), 1724–1744. https://doi.org/10.1039/D1DT03870B.
3. Melese, A.; Wubet, W.; Hussen, A.; Temesgen, A.; Mulate, K. Review on Activation of Small Molecules (Dihydrogen, Carbon Dioxide, and Dinitrogen) by Various Transition Metal Complexes. *Journal of Chemical Research* **2025**. https://doi.org/10.1177/17475198251313648.
4. Somerville, R. J.; Campos, J. Cooperativity in Transition Metal Tetrylene Complexes. *Eur. J. Inorg. Chem.* **2021**, *2021* (34), 3488–3498. https://doi.org/10.1002/ejic.202100460.
5. Inoue, S.; Melen, R. L.; Harder, S. Main Group Catalysis. *European Journal of Inorganic Chemistry* **2022**, *2022* (26), e202200414. https://doi.org/10.1002/ejic.202200414.
6. Pang, Y.; Nöthling, N.; Leutzsch, M.; Kang, L.; Bill, E.; van Gastel, M.; Reijerse, E.; Goddard, R.; Wagner, L.; SantaLucia, D.; DeBeer, S.; Neese, F.; Cornella, J. Synthesis and Isolation of a Triplet Bismuthinidene with a Quenched Magnetic Response. *Science* **2023**, *380* (6649), 1043–1048. https://doi.org/10.1126/science.adg2833.
7. Meleschko, D.; Palui, P.; Pugliese, G.; Schnakenburg, G.; Gomila, R. M.; Frontera, A.; Bismuto, A. Synthesis, Reactivity, and Theoretical Insights of Co-Sb2 and Co-Bi2 Rings. *Organometallics* **2024**, *43* (20), 2581–2588. https://doi.org/10.1021/acs.organomet.4c00238.
8. Weber, L.; Ebeler, F.; Ghadwal, R. S. Advances and Recent Trends in Dipnictenes Chemistry. *Coord. Chem. Rev.* **2022**, *461*, 214499. https://doi.org/10.1016/j.ccr.2022.214499.
9. Jones, C. Dimeric Magnesium(I) β-Diketiminates: A New Class of Quasi-Universal Reducing Agent. *Nat. Rev. Chem.* **2017**, *1* (8), 1–9. https://doi.org/10.1038/s41570-017-0059.
10. Schwamm, R. J.; Lein, M.; Coles, M. P.; Fitchett, C. M. Bi−P Bond Homolysis as a Route to Reduced Bismuth Compounds and Reversible Activation of P_4. *Angew. Chem. Int. Ed.* **2016**, *55* (47), 14798–14801. https://doi.org/10.1002/anie.201608615.
11. Ishida, S.; Hirakawa, F.; Furukawa, K.; Yoza, K.; Iwamoto, T. Persistent Antimony- and Bismuth-Centered Radicals in Solution. *Angew. Chem. Int. Ed.* **2014**, *53* (42), 11172–11176. https://doi.org/10.1002/anie.201405509.
12. Schwamm, R. J.; Coles, M. P. Distibanes and Distibenes from Reduction of Sb(NON^R)Cl by Using MgI Reagents. *Chem. Eur. J.* **2019**, *25* (62), 14183–14191. https://doi.org/10.1002/chem.201903175.
13. Dabringhaus, P.; Barthélemy, A.; Krossing, I. The Coordination Chemistry and Clustering of Subvalent Ga+ and In+ upon Addition of σ-Donor Ligands. *Z. Anorg. Allg. Chem.* **2021**, *647* (18), 1660–1673. https://doi.org/10.1002/zaac.202100129.
14. Glootz, K.; Kratzert, D.; Himmel, D.; Kastro, A.; Yassine, Z.; Findeisen, T.; Krossing, I. Tetracationic Gallium Cluster Cations. *Angew. Chem. Int. Ed.* **2018**, *57* (43), 14203–14206. https://doi.org/10.1002/anie.201807486.
15. Dabringhaus, P.; Molino, A.; Gilliard, R. J. Jr. Carbodiphosphorane-Activated Distibene and Dibismuthene Dications. *J. Am. Chem. Soc.* **2024**, *146* (39), 27186–27195. https://doi.org/10.1021/jacs.4c10834.
16. Barthélemy, A.; Krossing, I. Cationic Group 13 and 14 Element Clusters. *Inorg. Chem.* **2024**, *63* (46), 21763–21787. https://doi.org/10.1021/acs.inorgchem.4c03251.
17. Li, T.; Wei, H.; Fang, Y.; Wang, L.; Chen, S.; Zhang, Z.; Zhao, Y.; Tan, G.; Wang, X. Elusive Antimony-Centered Radical Cations: Isolation, Characterization, Crystal Structures, and Reactivity Studies. *Angew. Chem. Int. Ed.* **2017**, *56* (2), 632–636. https://doi.org/10.1002/anie.201610334.
18. Li, S.; Shiri, F.; Xu, G.; Yiu, S.-M.; Lee, H. K.; Ng, T. H.; Lin, Z.; Lu, Z. Reactivity of a Hexaaryldiboron(6) Dianion as Boryl Radical Anions. *J. Am. Chem. Soc.* **2024**, *146* (25), 17348–17354. https://doi.org/10.1021/jacs.4c04253.
19. Haldar, H.; Das, S.; Wiedemann, H. T. A.; Beuthert, K.; Kay, C. W. M.; Dehnen, S.; Yildiz, C. B.; Majumdar, M. Tetra-Cationic Distibane Stabilized by Bis(α-Iminopyridine) and Its

Reactivity. *J. Am. Chem. Soc.* **2025**, *147* (4), 3140–3151. https://doi.org/10.1021/jacs.4c12354.
20. Haldar, H. Bis (α-Iminopyridine) Stabilized Dimeric Sb(II) and Bi(II) Tetra-Cation : Bond Lability Based Reactivity. Thesis, 2024. http://dr.iiserpune.ac.in:8080/xmlui/handle/123456789/8741 (accessed 2025-03-15).
21. de Marcillac, P.; Coron, N.; Dambier, G.; Leblanc, J.; Moalic, J.-P. Experimental Detection of α-Particles from the Radioactive Decay of Natural Bismuth. *Nature* **2003**, *422* (6934), 876–878. https://doi.org/10.1038/nature01541.
22. Bradley, B.; Singleton, M.; Po, A. L. W. Bismuth Toxicity—a Reassessment. *Journal of Clinical Pharmacy and Therapeutics* **1989**, *14* (6), 423–441. https://doi.org/10.1111/j.1365-2710.1989.tb00268.x.
23. S. A. Singerling, R. M. Callaghan, 2018 USGS Minerals Yearbook: Bismuth, United States Geological Survey, **2018** https://pubs.usgs.gov/myb/vol1/2018/myb1-2018-bismuth.pdf.
24. The Sohio Acrylonitrile Process (American Chemical Society, **1996**). https://www.acs.org/content/dam/acsorg/education/whatischemistry/landmarks/acrylonitrile/sohio-acrylonitrile-process-commemorative-booklet-1996.pdf.
25. Maile, F. J.; Pfaff, G.; Reynders, P. Effect Pigments—Past, Present and Future. *Progress in Organic Coatings* **2005**, *54* (3), 150–163. https://doi.org/10.1016/j.porgcoat.2005.07.003.
26. Moon, H. W.; Cornella, J. Bismuth Redox Catalysis: An Emerging Main-Group Platform for Organic Synthesis. *ACS Catal.* **2022**, *12* (2), 1382–1393. https://doi.org/10.1021/acscatal.1c04897.
27. Mato, M.; Cornella, J. Bismuth in Radical Chemistry and Catalysis. *Angew. Chem. Int. Ed.* **2024**, *63* (8), e202315046. https://doi.org/10.1002/anie.202315046.
28. Peyronneau, M.; Arrondo, C.; Vendier, L.; Roques, N.; Le Roux, C. An Inexpensive and Simple Process for the Preparation of Antimony(III) and Bismuth(III) Triflates. *Journal of Molecular Catalysis A: Chemical* **2004**, *211* (1), 89–91. https://doi.org/10.1016/j.molcata.2003.10.020.
29. Mears, K. L.; Nguyen, G.-A.; Ruiz, B.; Lehmann, A.; Nelson, J.; Fettinger, J. C.; Tuononen, H. M.; Power, P. P. Hydrobismuthation: Insertion of Unsaturated Hydrocarbons into the Heaviest Main Group Element Bond to Hydrogen. *J. Am. Chem. Soc.* **2024**, *146* (1), 19–23. https://doi.org/10.1021/jacs.3c06535.
30. Haldar, H.; Yildiz, Cem. B.; Majumdar, M. Coordination Chemistry of the Antimony(III) and Bismuth(III) Cations Using Bis(α-Iminopyridine) as Ligand. *ChemPlusChem* **2023**, *88* (7), e202300211. https://doi.org/10.1002/cplu.202300211.
31. Šimon, P.; Jambor, R.; Růžička, A.; Dostál, L. Oxidative Addition of Diphenyldichalcogenides PhEEPh (E = S, Se, Te) to Low-Valent CN- and NCN-Chelated Organoantimony and Organobismuth Compounds. *Organometallics* **2013**, *32* (1), 239–248. https://doi.org/10.1021/om3010383.
32. Ramler, J.; Krummenacher, I.; Lichtenberg, C. Bismuth Compounds in Radical Catalysis: Transition Metal Bismuthanes Facilitate Thermally Induced Cycloisomerizations. *Angew. Chem. Int. Ed.* **2019**, *58* (37), 12924–12929. https://doi.org/10.1002/anie.201904365.
33. Mukhopadhyay, D. P.; Schleier, D.; Wirsing, S.; Ramler, J.; Kaiser, D.; Reusch, E.; Hemberger, P.; Preitschopf, T.; Krummenacher, I.; Engels, B.; Fischer, I.; Lichtenberg, C. Methylbismuth: An Organometallic Bismuthinidene Biradical. *Chem. Sci.* **2020**, *11* (29), 7562–7568. https://doi.org/10.1039/D0SC02410D.
34. Bondi, A. Van Der Waals Volumes and Radii. *J. Phys. Chem.* **1964**, *68* (3), 441–451. https://doi.org/10.1021/j100785a001.
35. Balazs, L.; Breunig, H. J.; Lork, E.; Soran, A.; Silvestru, C. Isomers of a Dibismuthane, R2Bi−BiR2 [R = 2,6-(Me2NCH2)2C6H3], and Unusual Reactions with Oxygen: Formation of [R2Bi]2(O2) and R‘R‘ ‘Bi [R‘ = 2-(Me2NCH2)-6-{Me2N(O)CH2}C6H3; R‘ ‘ = 2-(Me2NCH2)-6-{O(O)C}C6H3]. *Inorg. Chem.* **2006**, *45* (5), 2341–2346. https://doi.org/10.1021/ic052160n.
36. Thompson, S.; Burnett, S.; Ferns, R.; van Mourik, T.; McKay, A. P.; Slawin, A. M. Z.; Cordes, D. B.; Stasch, A. Facile, Reversible Hydrogen Activation by Low-Coordinate Magnesium Oxide Complexes. *J. Am. Chem. Soc.* **2025**. https://doi.org/10.1021/jacs.4c16041.
37. Donaldson, J. D.; Beyersmann, D. Cobalt and Cobalt Compounds. In *Ullmann's Encyclopedia of Industrial Chemistry*; Wiley, 2005. https://doi.org/10.1002/14356007.a07_281.pub2.

38. Green, J. C.; Green, M. L. H.; Parkin, G. The Occurrence and Representation of Three-Centre Two-Electron Bonds in Covalent Inorganic Compounds. *Chem. Commun.* **2012**, *48* (94), 11481–11503. https://doi.org/10.1039/C2CC35304K.
39. Vránová, I.; Alonso, M.; Jambor, R.; Růžička, A.; Erben, M.; Dostál, L. Stibinidene and Bismuthinidene as Two-Electron Donors for Transition Metals (Co and Mn). *Chem. Eur. J.* **2016**, *22* (22), 7376–7380. https://doi.org/10.1002/chem.201601272.
40. Jones, J. S.; Pan, B.; Gabbaï, F. P. Group 15 Metal–Metal Bonds. In *Molecular Metal-Metal Bonds*; John Wiley & Sons, Ltd, 2015; pp 519–558. https://doi.org/10.1002/9783527673353.ch15.
41. Ramler, J.; Krummenacher, I.; Lichtenberg, C. Bismuth Compounds in Radical Catalysis: Transition Metal Bismuthanes Facilitate Thermally Induced Cycloisomerizations. *Angew. Chem. Int. Ed.* **2019**, *58* (37), 12924–12929. https://doi.org/10.1002/anie.201904365.
42. Roters, S.; Hepp, A.; Slootweg, J. C.; Lammertsma, K.; Uhl, W. Alkynide and Acetonitrile Activation by Strained $AlPC_2$ Heterocycles. *Chem. Commun.* **2012**, *48* (77), 9616–9618. https://doi.org/10.1039/C2CC33300G.
43. Zhou, X.; Gao, X.; Liu, M.; Gao, Z.; Qin, X.; Xu, W.; Ye, S.; Zhou, W.; Fan, H.; Li, J.; Fan, S.; Yang, L.; Fu, J.; Xiao, D.; Lin, L.; Ma, D.; Yao, S. Photocatalytic Dehydrogenative C-C Coupling of Acetonitrile to Succinonitrile. *Nat. Commun.* **2022**, *13* (1), 4379. https://doi.org/10.1038/s41467-022-32137-y.
44. Evans, M. E.; Li, T.; Jones, W. D. C−H vs C−C Bond Activation of Acetonitrile and Benzonitrile via Oxidative Addition: Rhodium vs Nickel and Cp* vs Tp′ (Tp′ = Hydrotris(3,5-Dimethylpyrazol-1-Yl)Borate, Cp* = H5-Pentamethylcyclopentadienyl). *J. Am. Chem. Soc.* **2010**, *132* (45), 16278–16284. https://doi.org/10.1021/ja107927b.
45. Fridrichová, A.; Svoboda, T.; Jambor, R.; Padělková, Z.; Růžička, A.; Erben, M.; Jirásko, R.; Dostál, L. Synthesis and Structural Study on Organoantimony(III) and Organobismuth(III) Hydroxides Containing an NCN Pincer Type Ligand. *Organometallics* **2009**, *28* (18), 5522–5528. https://doi.org/10.1021/om900607n.
46. Breunig, H. J.; Haddad, N.; Lork, E.; Mehring, M.; Mügge, C.; Nolde, C.; Raţ, C. I.; Schürmann, M. Novel Sterically Congested Monoorganobismuth(III) Compounds: Synthesis, Structure, and Bismuth−Arene π Interaction in ArBiXY (X, Y = Br, I, OH, 2,6-Mes2-4-t-Bu-$C_6H_2PHO_2$). *Organometallics* **2009**, *28* (4), 1202–1211. https://doi.org/10.1021/om800934c.
47. Grobe, J.; Golla, W.; Le Van, D.; Krebs, B.; Läge, M. Preparation and Characterization of a Series of Novel Mono(Metallo)Stibanes [M]Sb(CF3)2. *Organometallics* **1998**, *17* (26), 5717–5720. https://doi.org/10.1021/om9807452.

Appendix

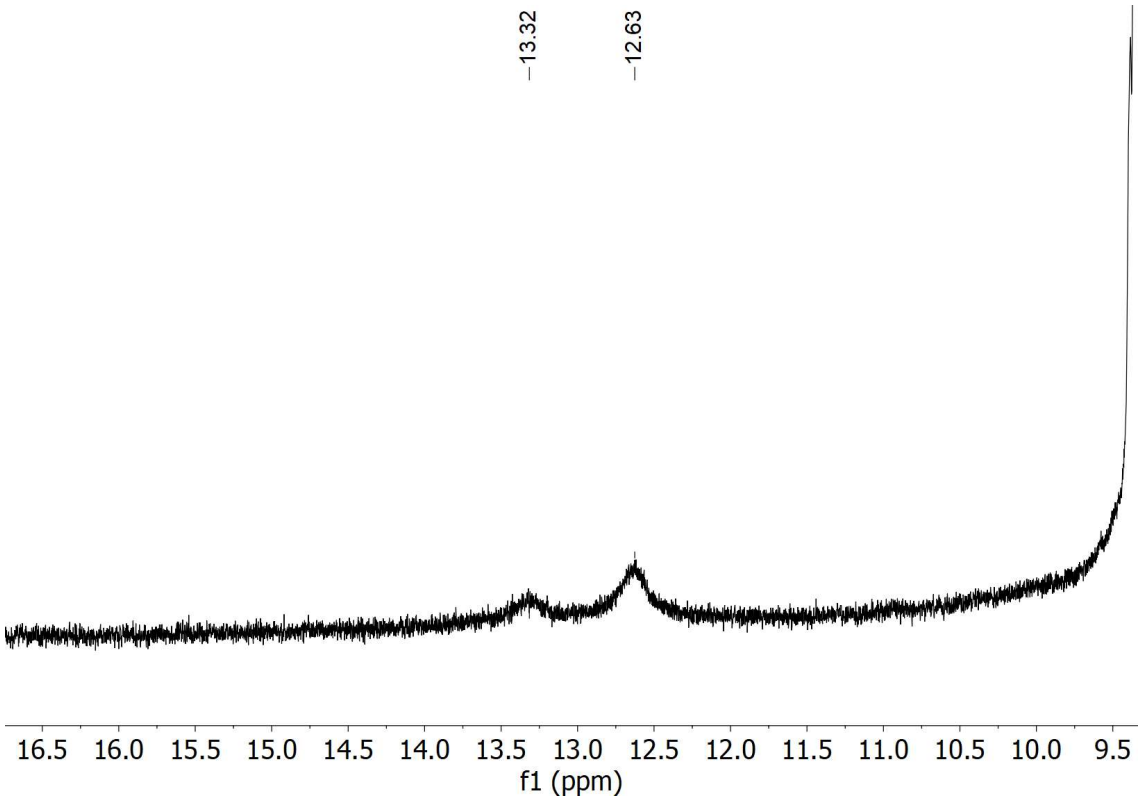

Figure 9. ^{1}H NMR of *in-situ* reaction mixture for $[2]_2[OTf]_4$ (400 MHz, CD_3CN, 278 K, 16.16 mM).

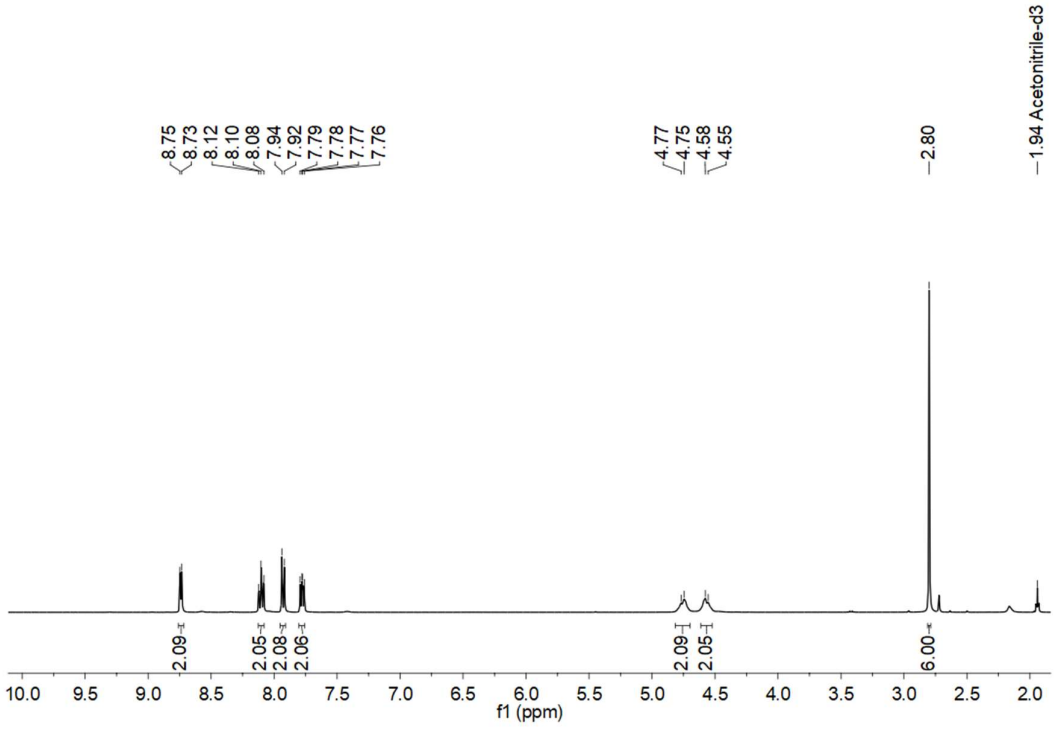

Figure 10. ^{1}H NMR spectrum (400 MHz, CD_3CN, 298 K, 16.16 mM) of $[\mathbf{2}]_2[OTf]_4$.

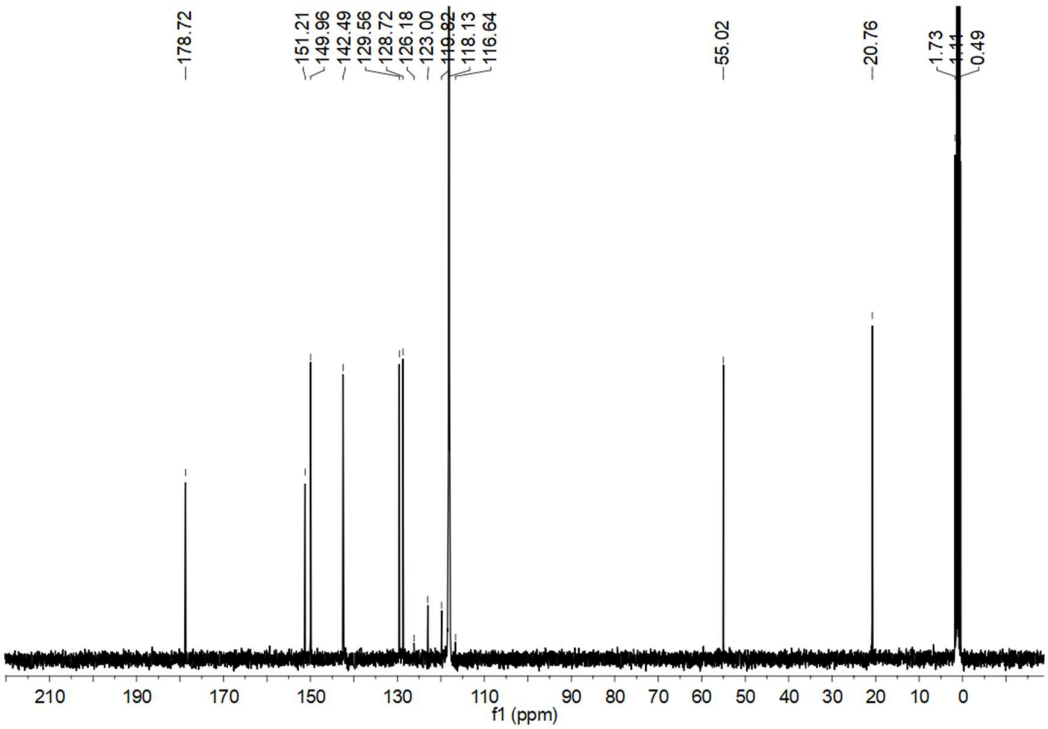

Figure 11. $^{13}C\{^{1}H\}$ NMR spectrum (101 MHz, CD_3CN, 298 K, 16.16 mM) of [**2**]$_2$[OTf]$_4$.

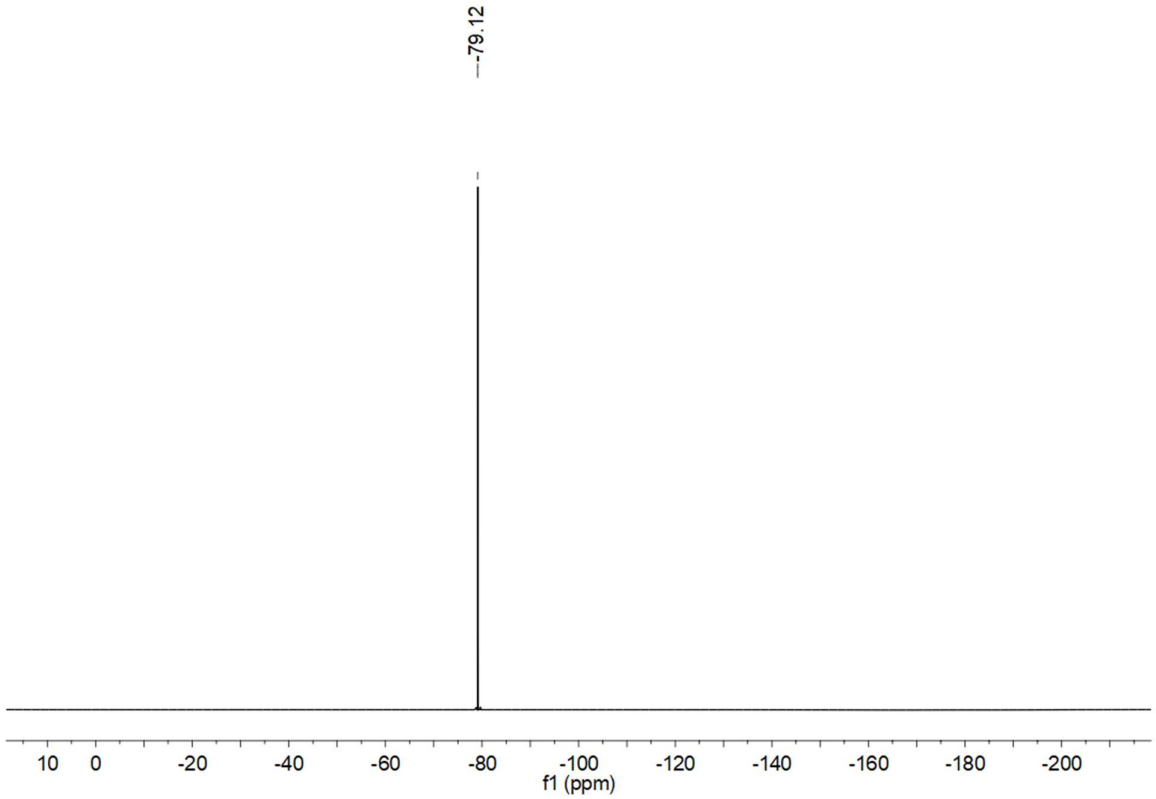

Figure 12. $^{19}F\{^{1}H\}$ NMR spectrum (377 MHz, CD_3CN, 298 K) of [**2**]$_2$[OTf]$_4$.

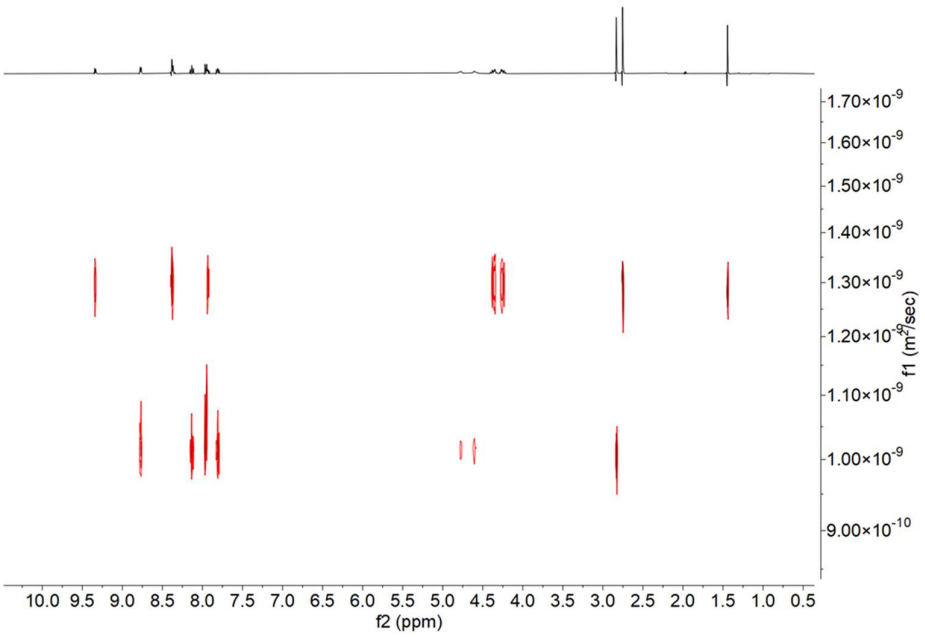

Figure 13. DOSY NMR spectra of [**2**]$_2$[OTf]$_4$ at 24.24 mM. In this case we found two peaks one at 2.72 ppm which we normally get for monomer and additional peak is also visible at 2.81 ppm corresponding to the dimer after the change of some parameters for DOSY.

From the analysis of the data, I found the diffusion coefficient of the monomer to be $1.307458 * 10^{-9}$ m^2/s and the diffusion coefficient of the dimer to be $9.878444 * 10^{-10}$ m^2s^{-1}.

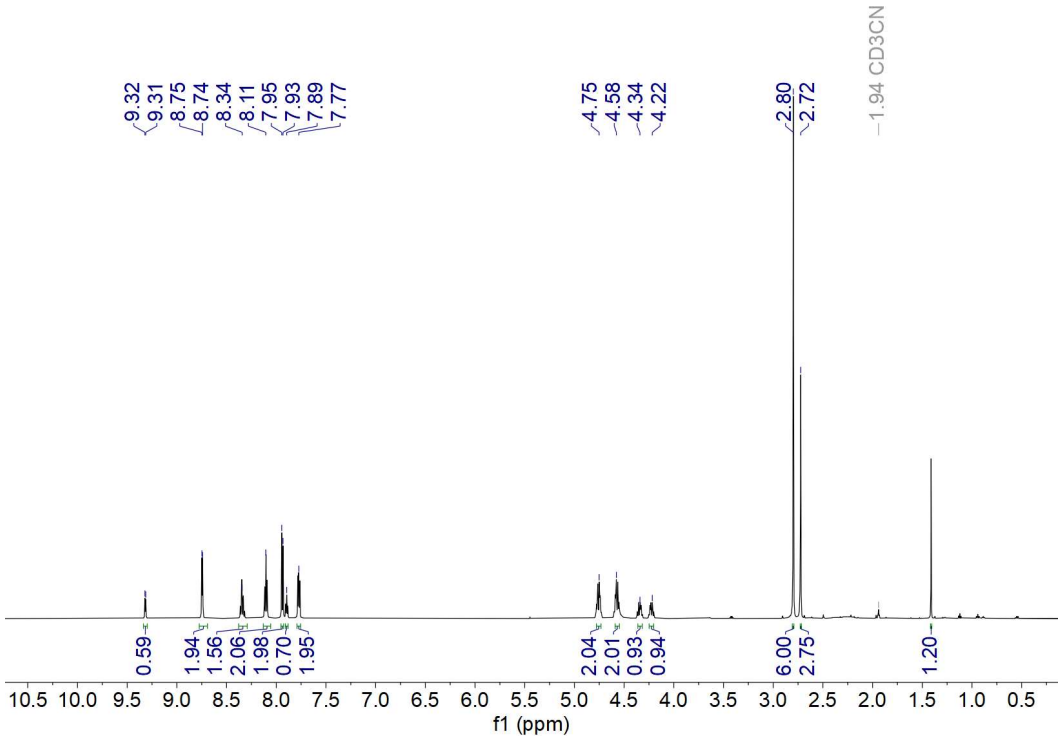

Figure 14. ^{1}H NMR spectrum after time-delay (600 MHz, CD_3CN, 298 K, 24.24 mM) of [**2**]$_2$[OTf]$_4$. Two sets of peaks found, possibly indicating the monomer-dimer equilibrium or if the peak at +1.41ppm is considered for Bi-Me species then the equilibrium between [**2**]$_2$[OTf]$_4$ and [**10**][OTf]$_2$.

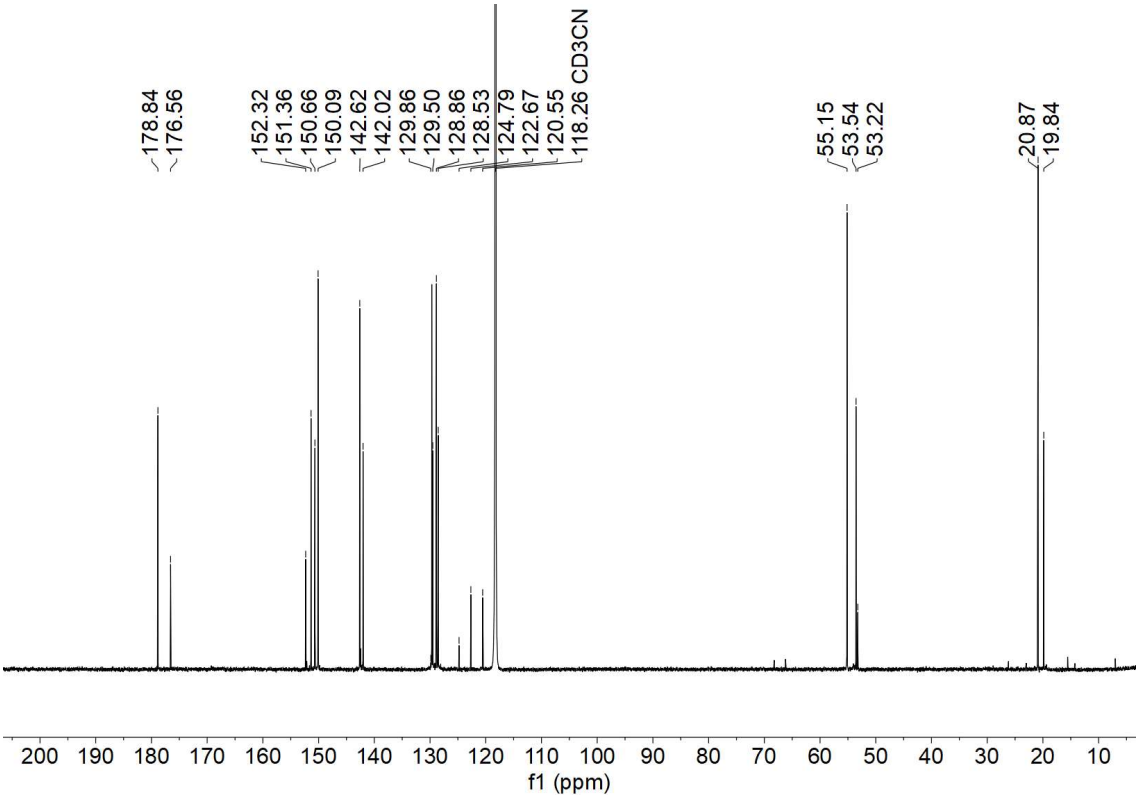

Figure 15. $^{13}C\{^{1}H\}$ NMR spectrum after time-delay (151 MHz, CD_3CN, 298 K, 24.24 mM) of [**2**]$_2$[OTf]$_4$. Two sets of peaks found, equilibrium between [**2**]$_2$[OTf]$_4$ and [**10**][OTf]$_2$.

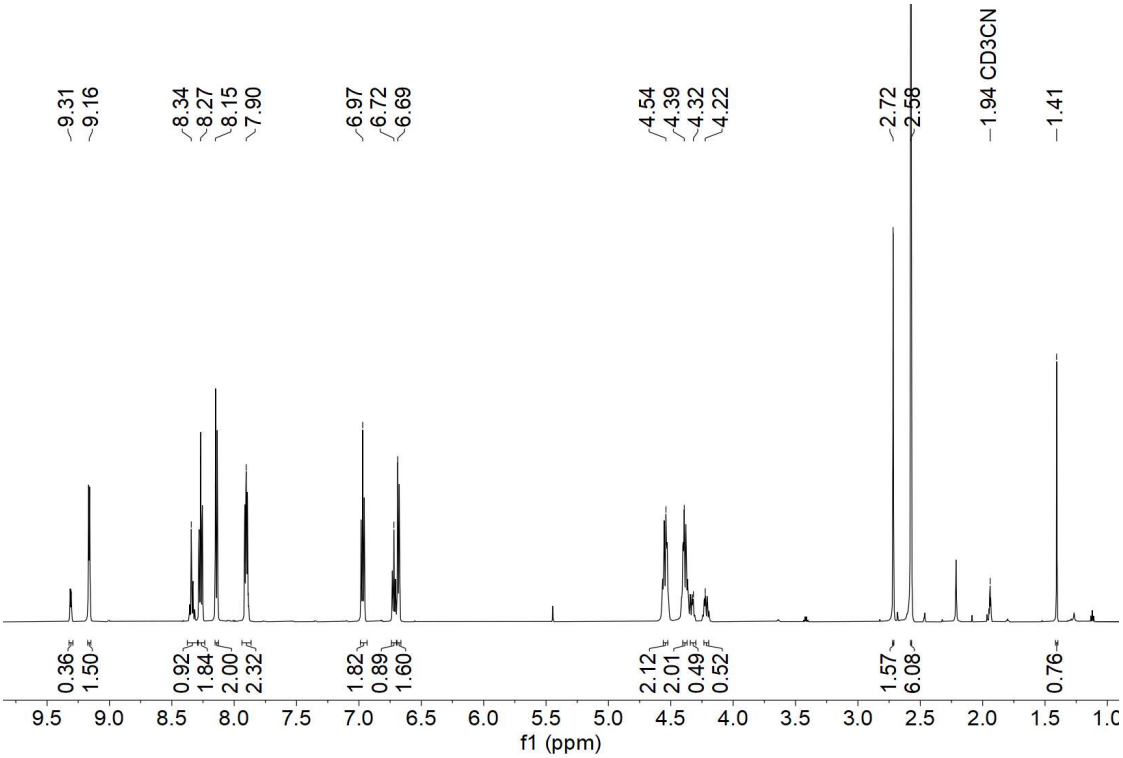

Figure 16. ^{1}H NMR spectrum (600 MHz, CD_3CN, 298 K, 42.51 mM) of [**3**][OTf]$_2$. Two sets of peaks, one is assigned to [**3**][OTf]$_2$ and the other set is assigned to Bi-Me species [**10**][OTf]$_2$ due to reversible binding of –SPh fragment or due to co-crystallization of both species due to competing acetonitrile activation.

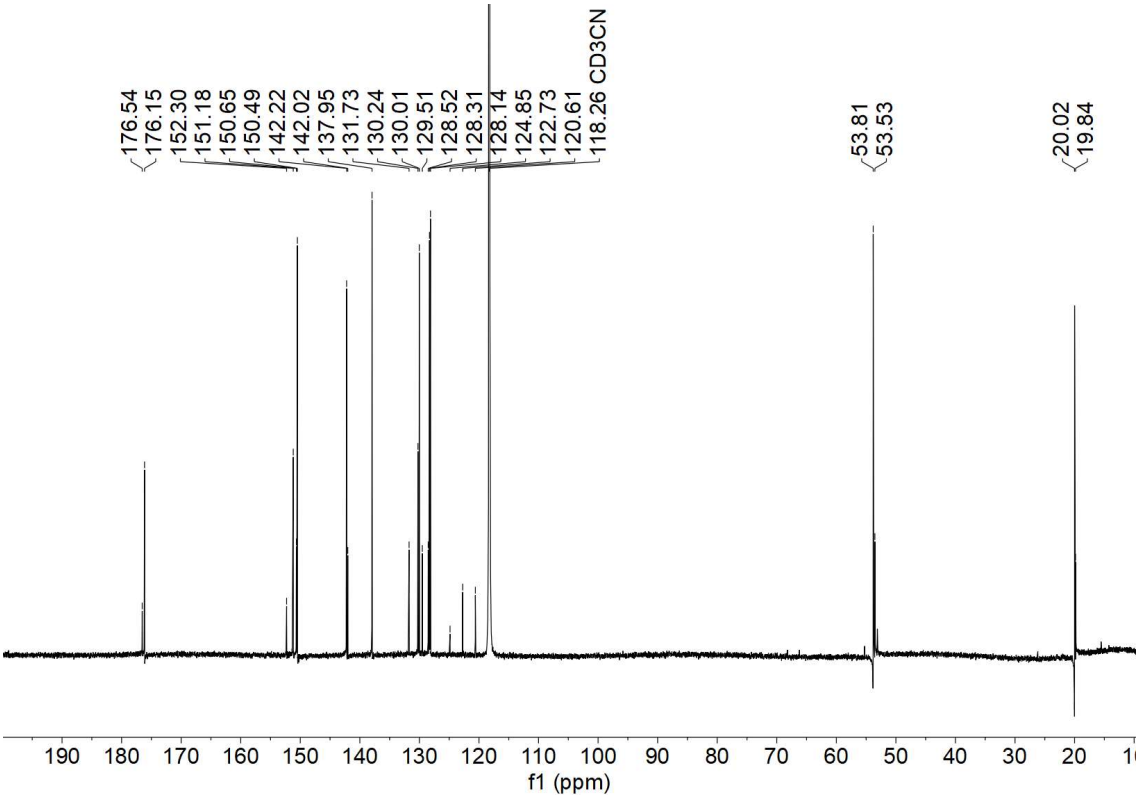

Figure 17. $^{13}C\{^{1}H\}$ NMR spectrum (151 MHz, CD_3CN, 298 K, 42.51 mM) of [**3**][OTf]$_2$. Two sets of peaks found, One for [**3**][OTf]$_2$ and other having less intensity for [**10**][OTf]$_2$.

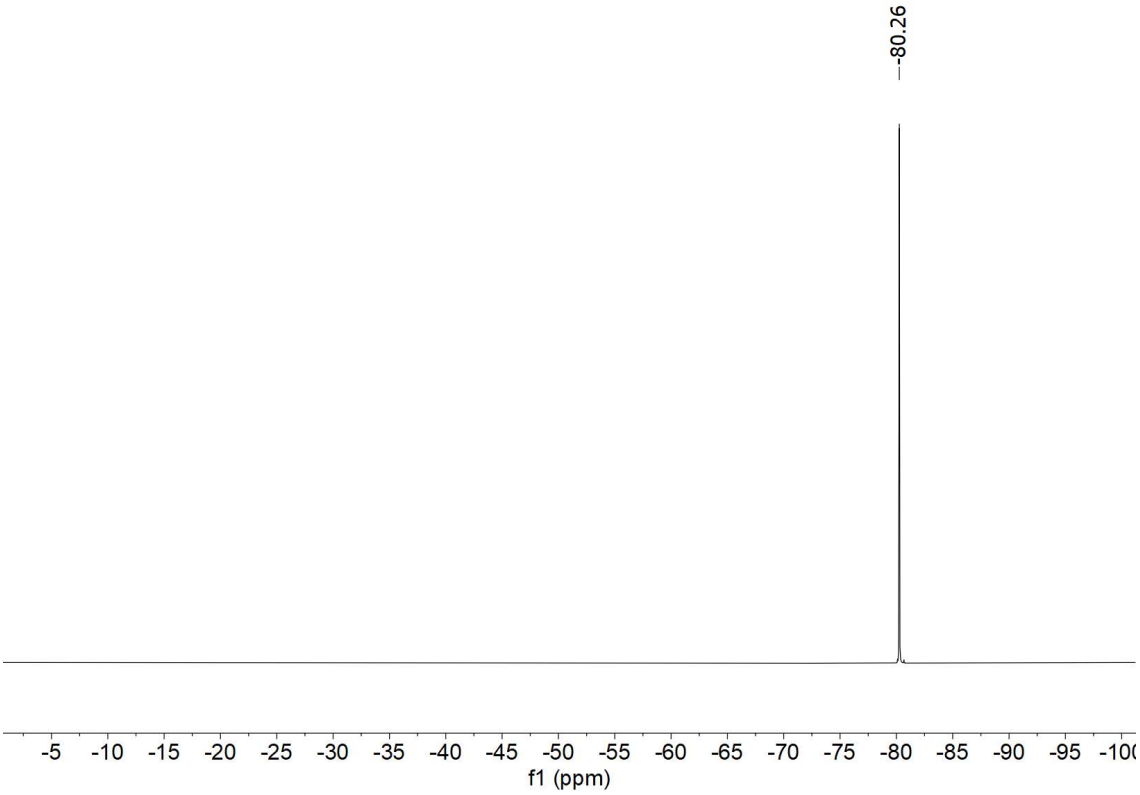

Figure 18. ^{19}F NMR spectrum (564 MHz, CD_3CN, 298 K, 42.51 mM) of [**3**][OTf]$_2$.

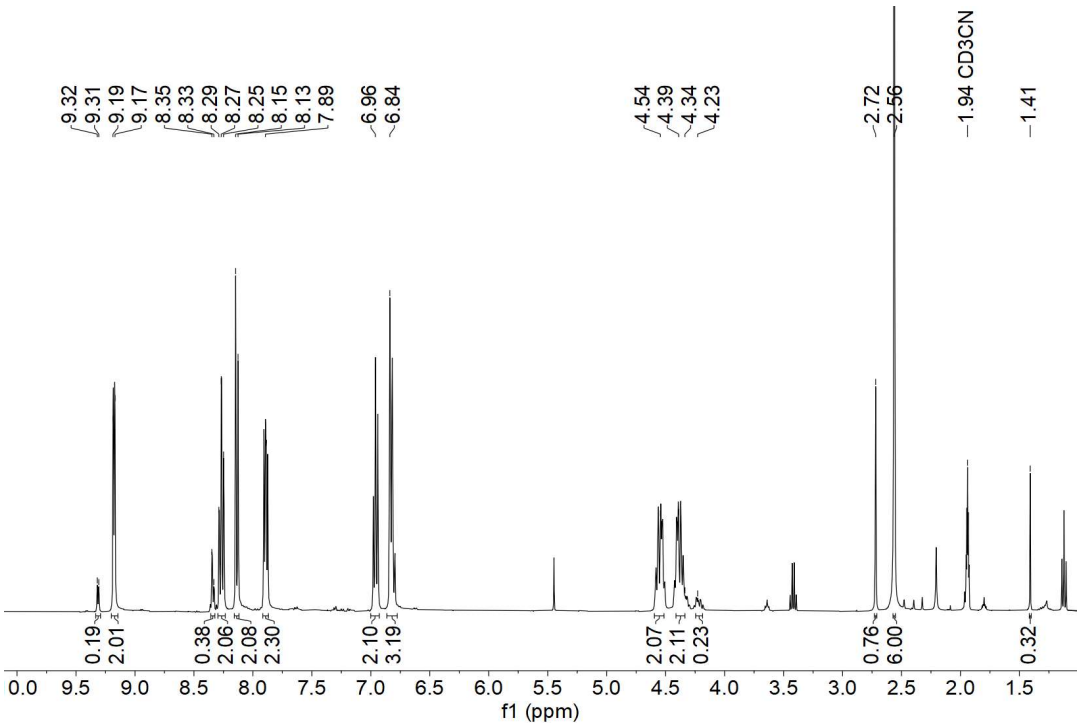

Figure 19. ^{1}H NMR spectrum (600 MHz, CD_3CN, 298 K, 40.40 mM) of [**4**][OTf]$_2$. Two sets of peaks, one is assigned to [**4**][OTf]$_2$ and the other set is assigned to Bi-Me species [**10**][OTf]$_2$ due to reversible binding of –SePh fragment or due to co-crystallization of both species due to competing acetonitrile activation.

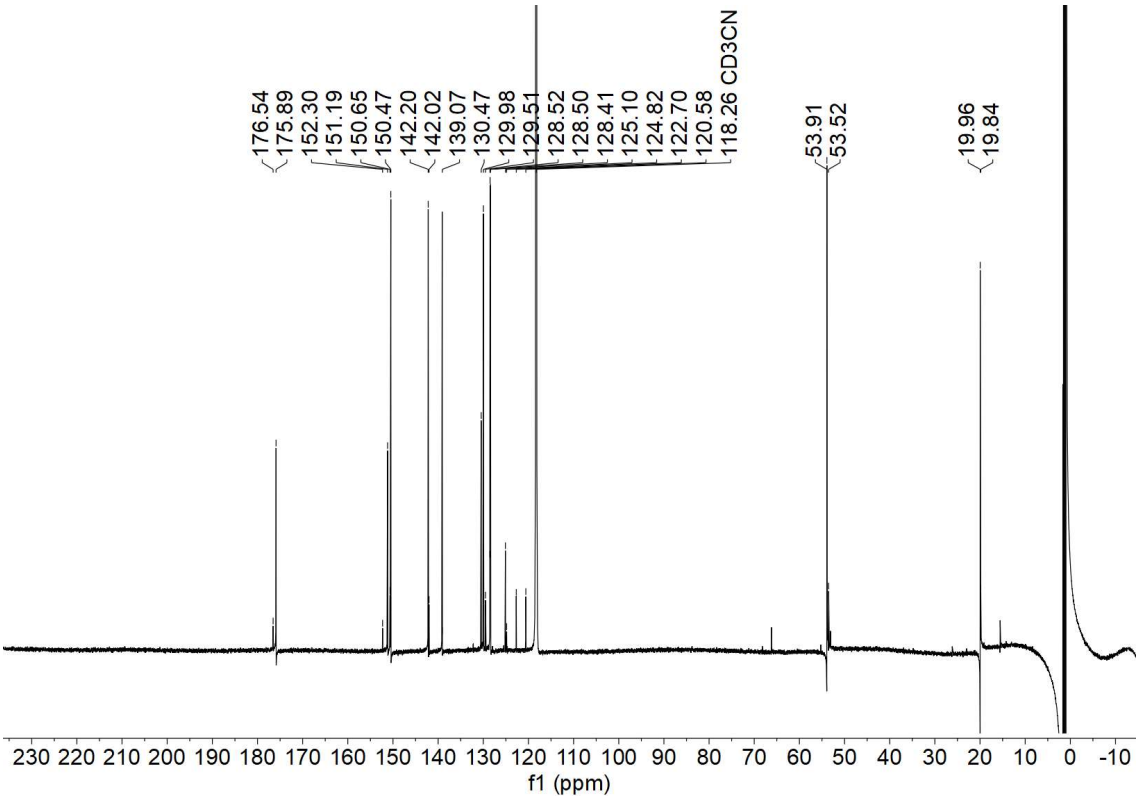

Figure 20. $^{13}C\{^{1}H\}$ NMR spectrum (151 MHz, CD_3CN, 298 K, 40.40 mM) of [**4**][OTf]$_2$. Two sets of peaks found, One for [**4**][OTf]$_2$ and other having less intensity for [**10**][OTf]$_2$.

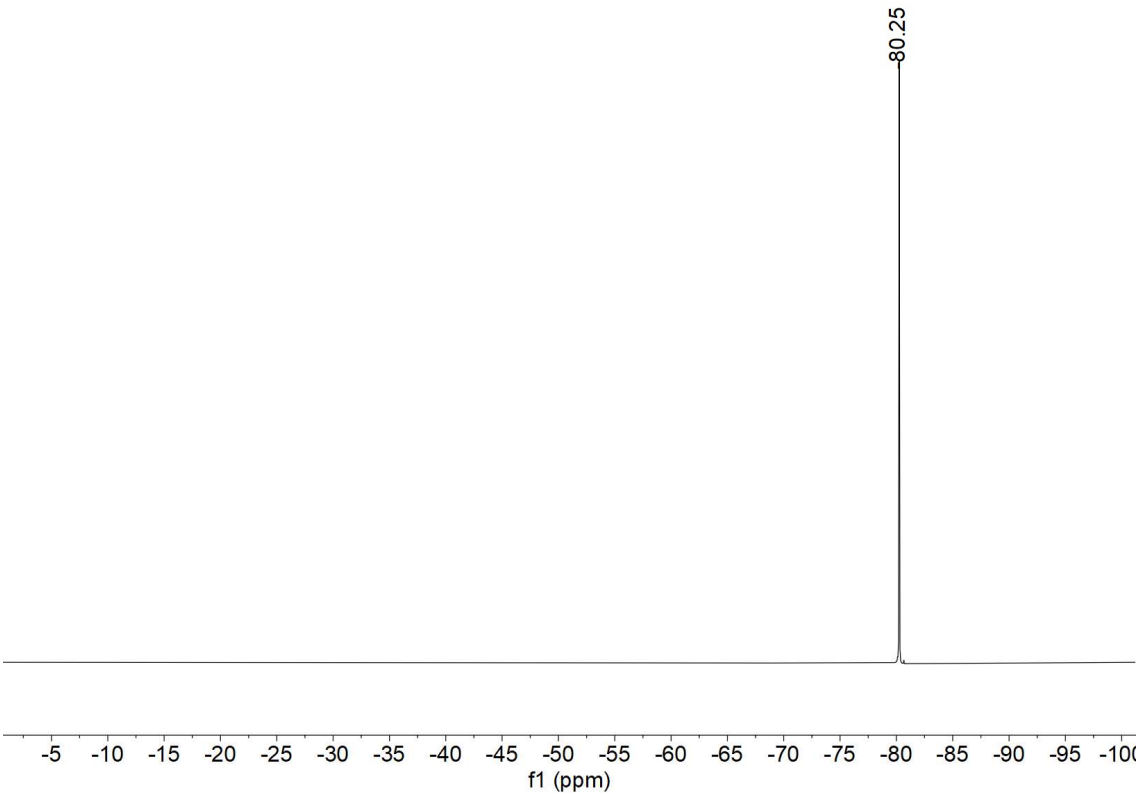

Figure 21. ^{19}F NMR spectrum (564 MHz, CD_3CN, 298 K, 40.40 mM) of [**4**][OTf]$_2$.

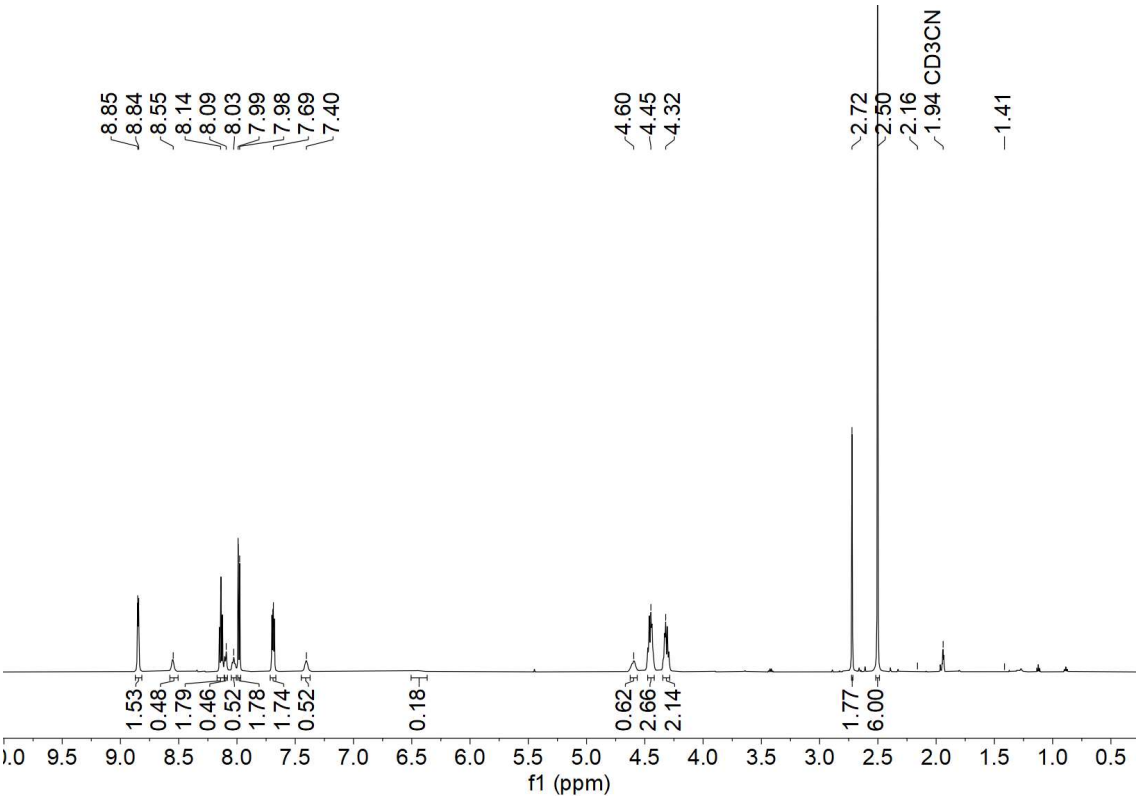

Figure 22. ^1H NMR spectrum (600 MHz, CD_3CN, 298 K, 23.73 mM) of [**6**][OTf]$_4$. Two sets of peaks, one due to [**6**][OTf]$_4$ and the other set is suspected as [**11**][OTf]$_4$.

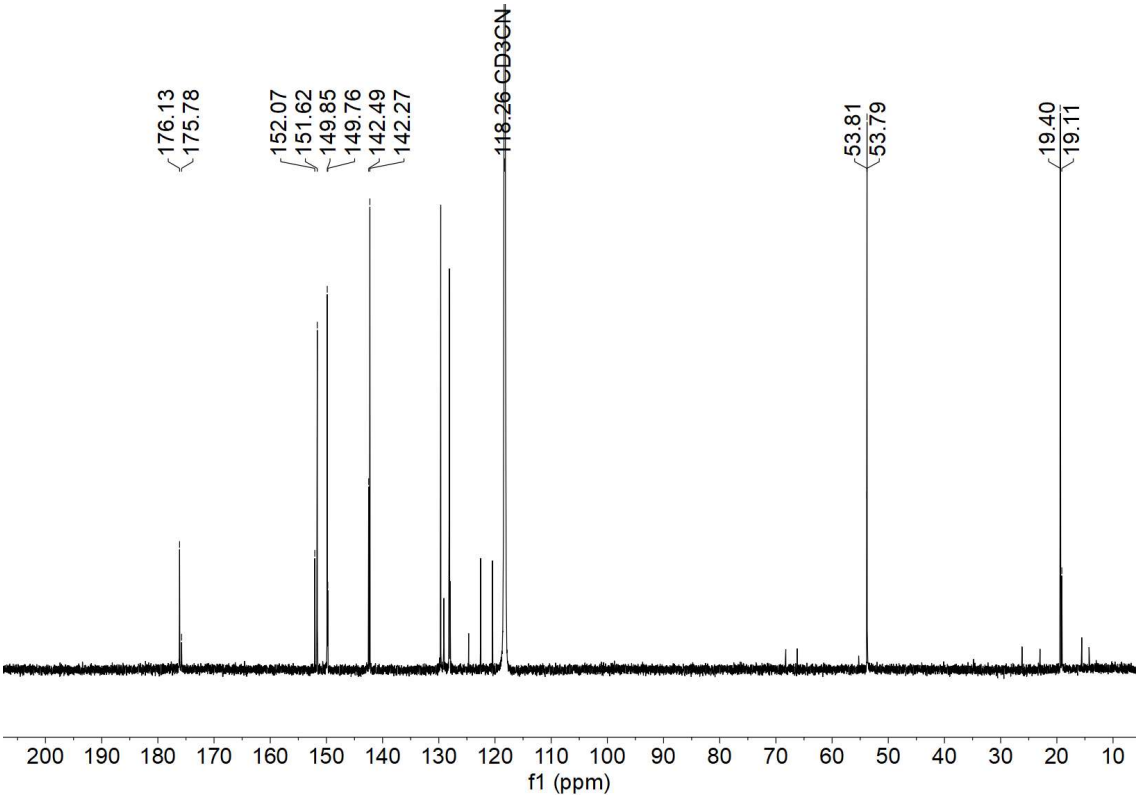

Figure 23. $^{13}C\{^{1}H\}$ NMR spectrum (151 MHz, CD_3CN, 298 K, 23.73 mM) of [**6**][OTf]$_4$. Two sets of peaks found, One for [**6**][OTf]$_4$ and other having less intensity for [**11**][OTf]$_4$.

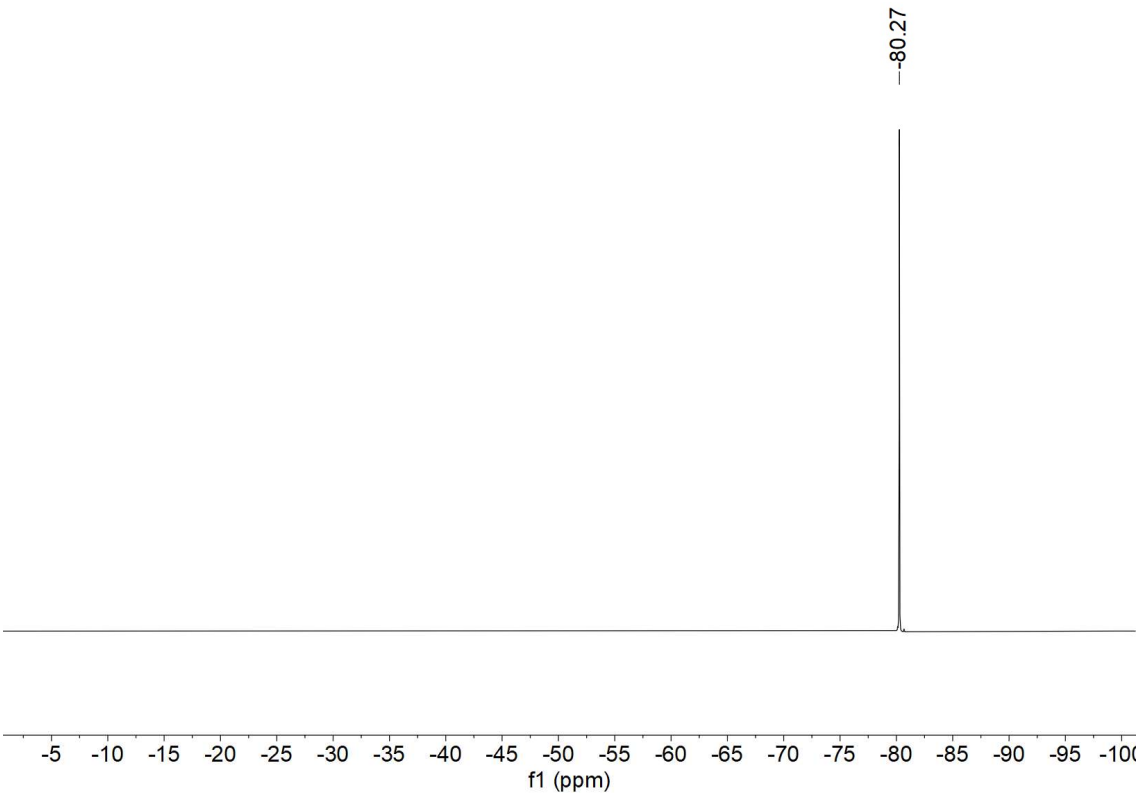

Figure 24. ^{19}F NMR spectrum (564 MHz, CD_3CN, 298 K, 23.73 mM) of [**6**][OTf]$_4$.

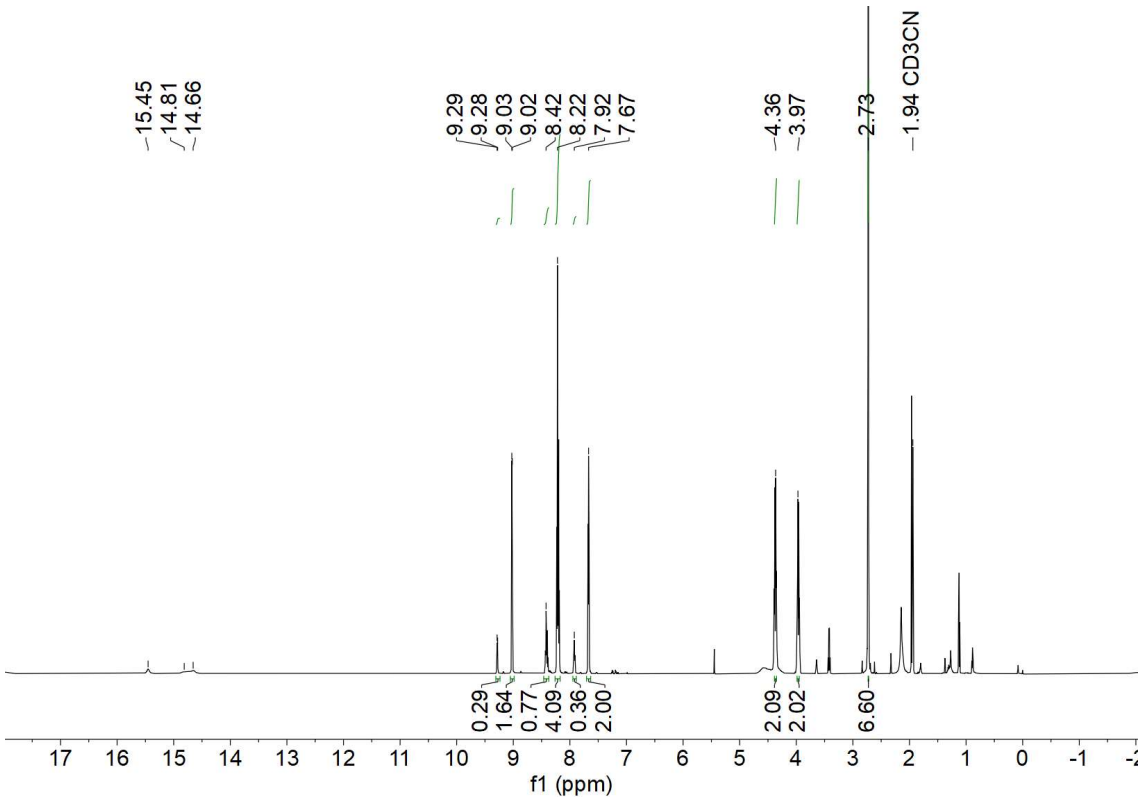

Figure 25. ^{1}H NMR spectrum (600 MHz, CD_3CN, 298 K, 23.73 mM) of [**7**][OTf]$_3$. Two sets of peaks, one due to [**7**][OTf]$_3$ and the other set is suspected as [**LBi-Co(CO)$_4$**][OTf]$_2$.

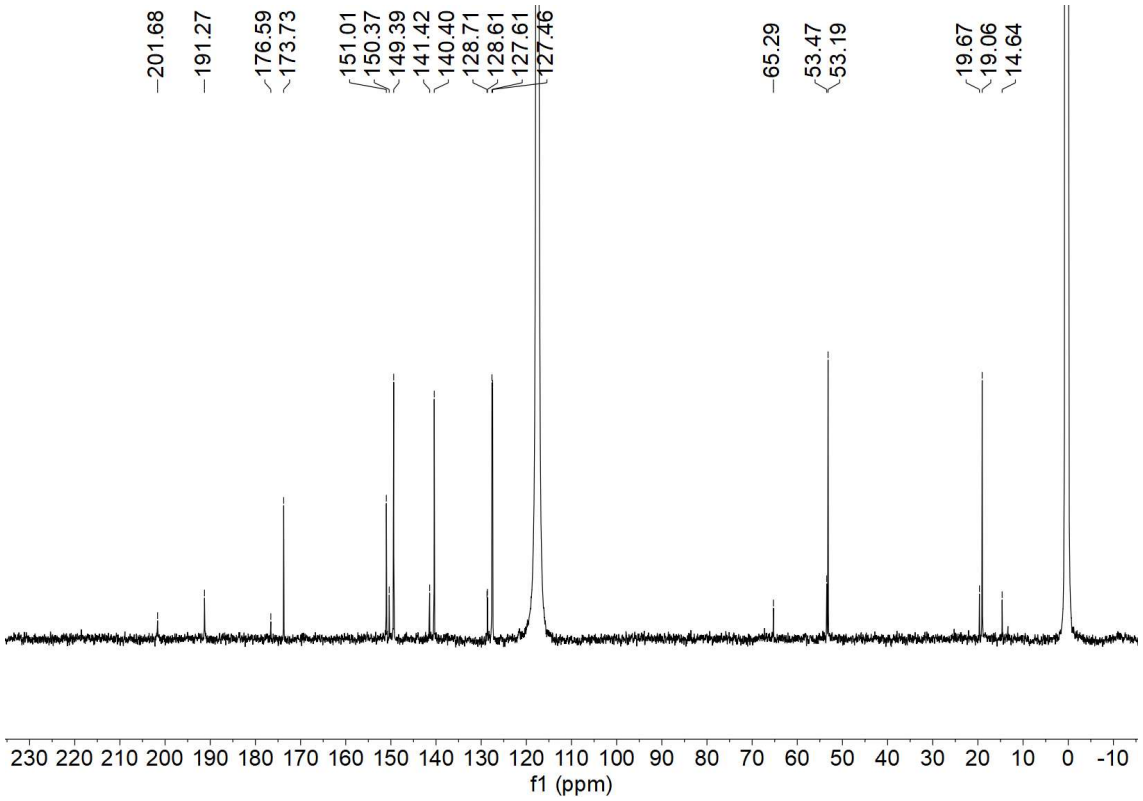

Figure 26. $^{13}C\{^{1}H\}$ NMR spectrum (151 MHz, CD_3CN, 298 K, 23.73 mM) of [**7**][OTf]$_3$. Two sets of peaks found, One for [**7**][OTf]$_3$ and other having less intensity for [**LBi-Co(CO)$_4$**][OTf]$_2$.

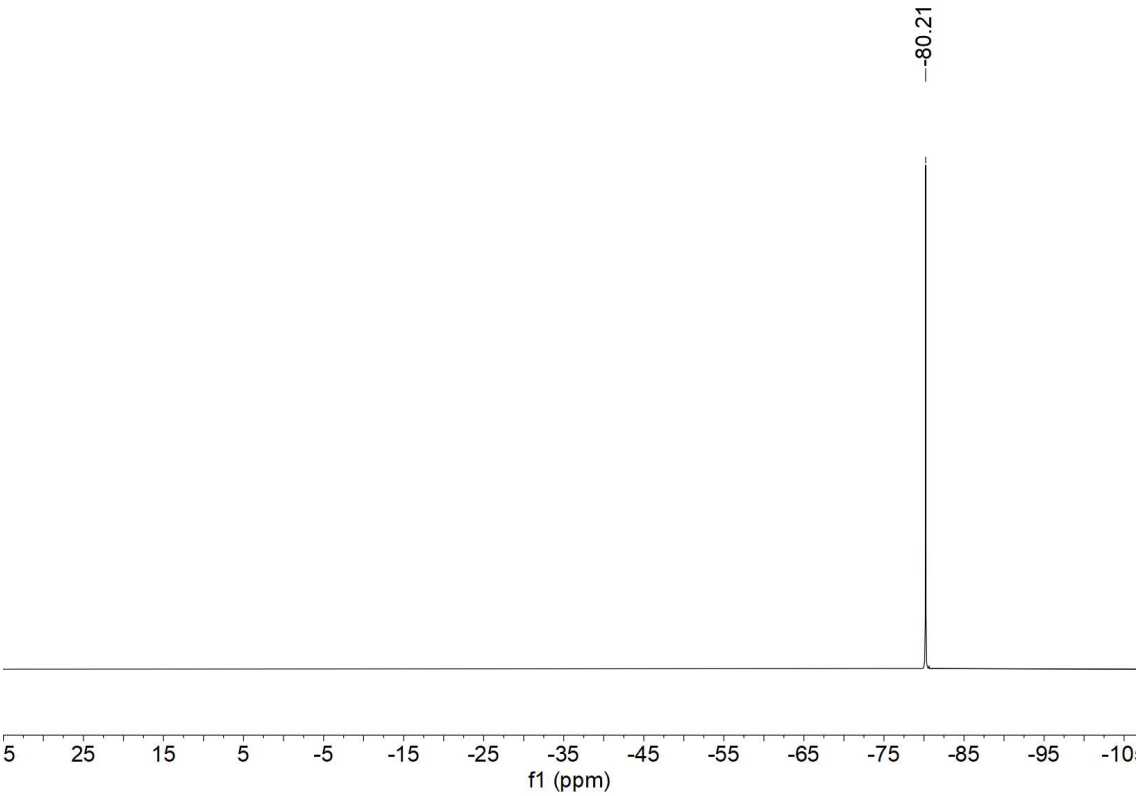

Figure 27. ^{19}F NMR spectrum (564 MHz, CD_3CN, 298 K, 23.73 mM) of [**7**][OTf]$_3$.

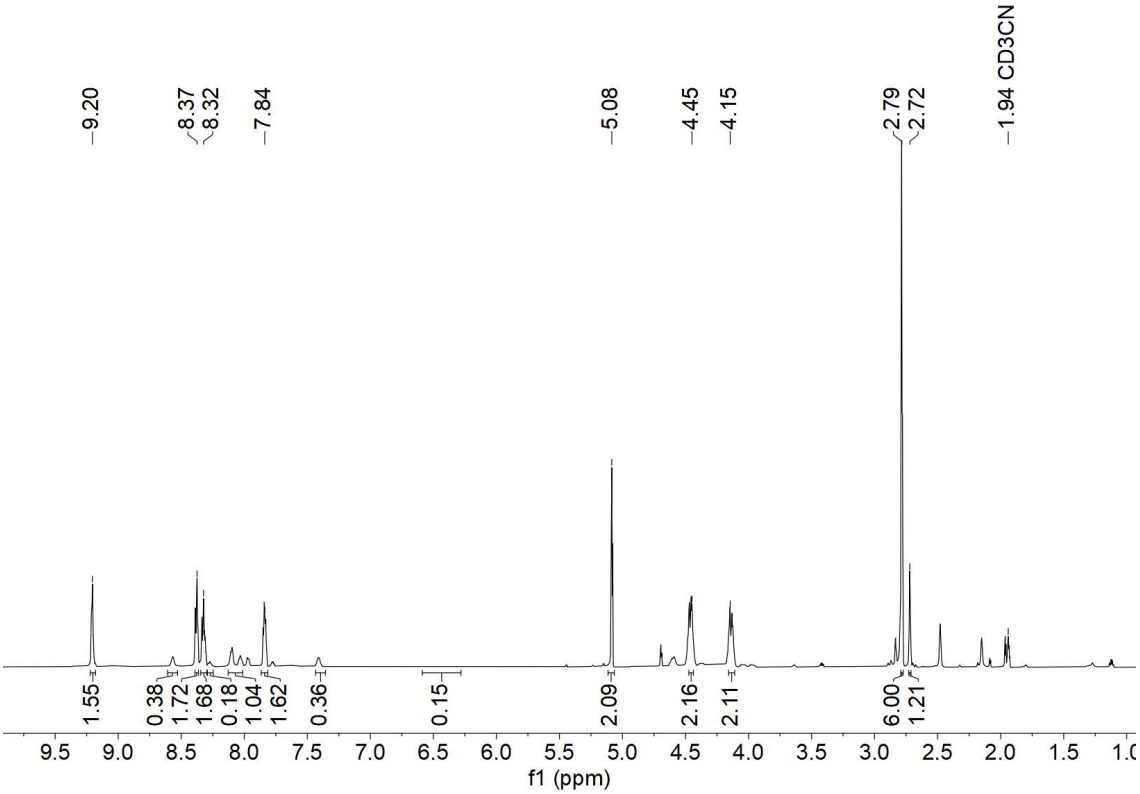

Figure 28. ^1H NMR spectrum (600 MHz, CD_3CN, 298 K, 32.33 mM) of [**9**][OTf]$_2$. Two sets of peaks, one due to [**9**][OTf]$_2$ and the other set is suspected as [**11**][OTf]$_4$.

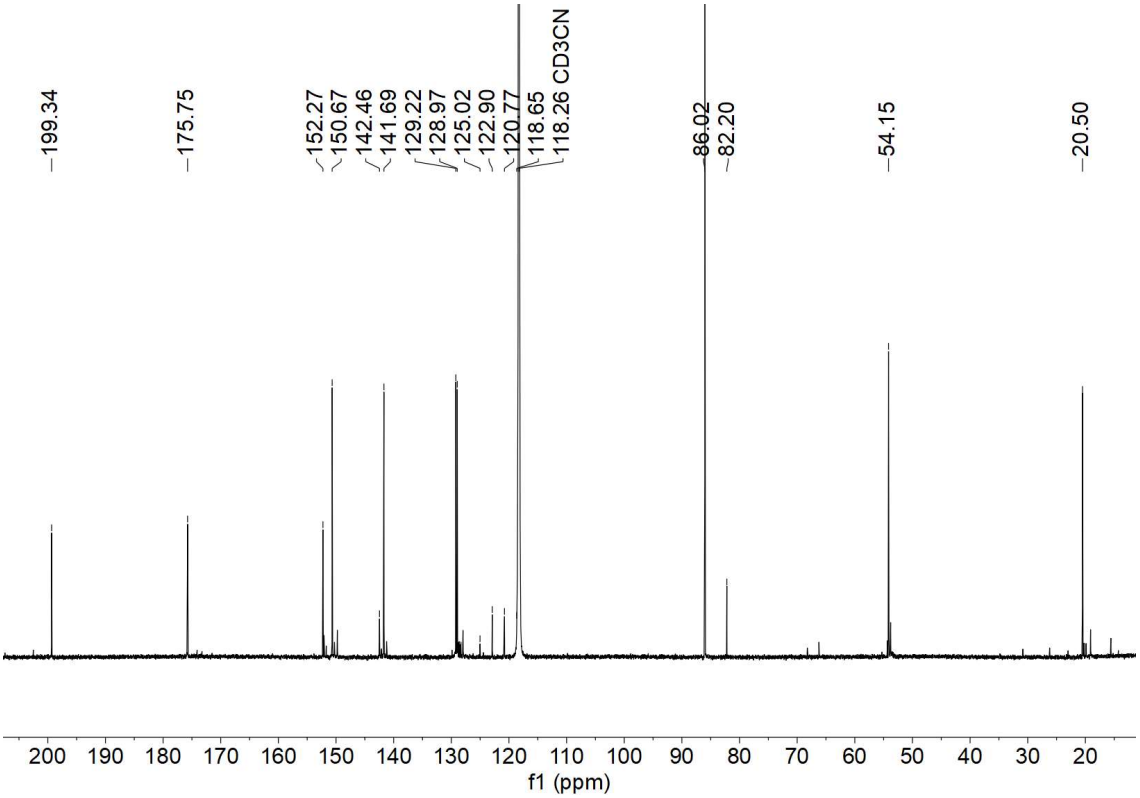

Figure 29. $^{13}C\{^{1}H\}$ NMR spectrum (151 MHz, CD_3CN, 298 K, 32.33 mM) of Two sets of peaks, one due to [**9**][OTf]$_2$ and the other set is suspected as [**11**][OTf]$_4$ and carbonyl peak at 199 ppm.

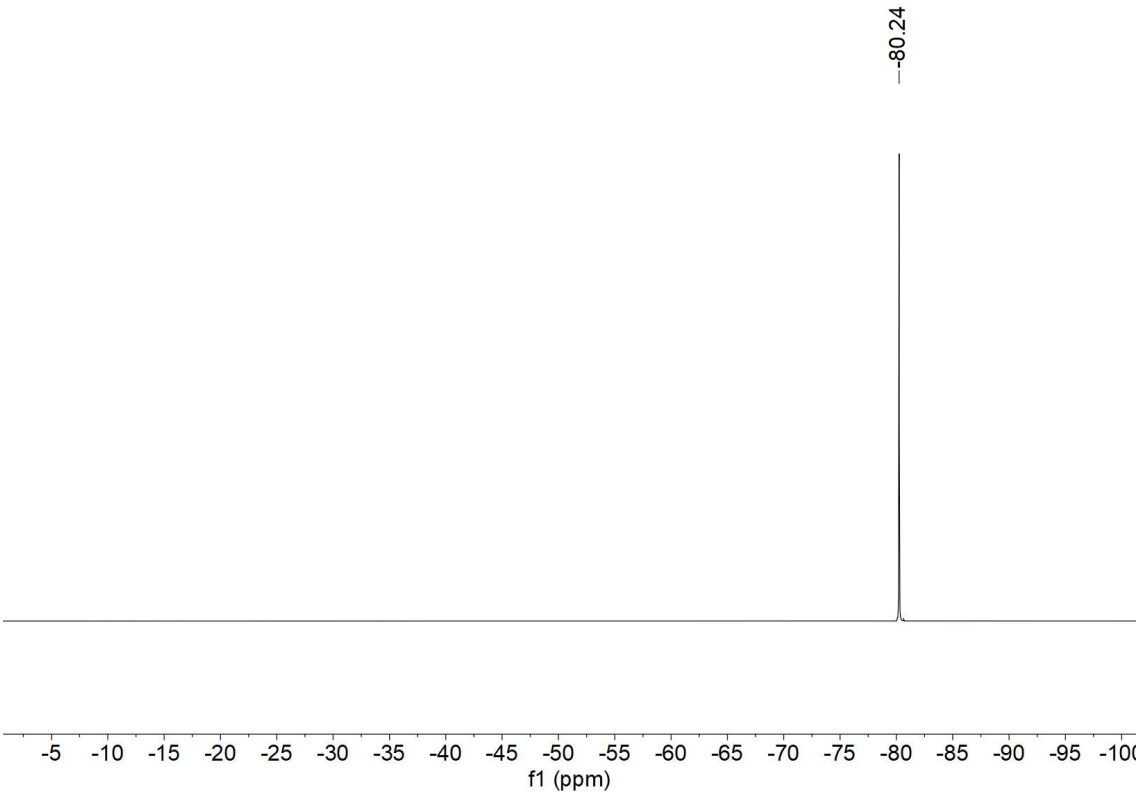

Figure 30. ^{19}F NMR spectrum (564 MHz, CD_3CN, 298 K, 32.33 mM) of [**9**][OTf]$_2$.

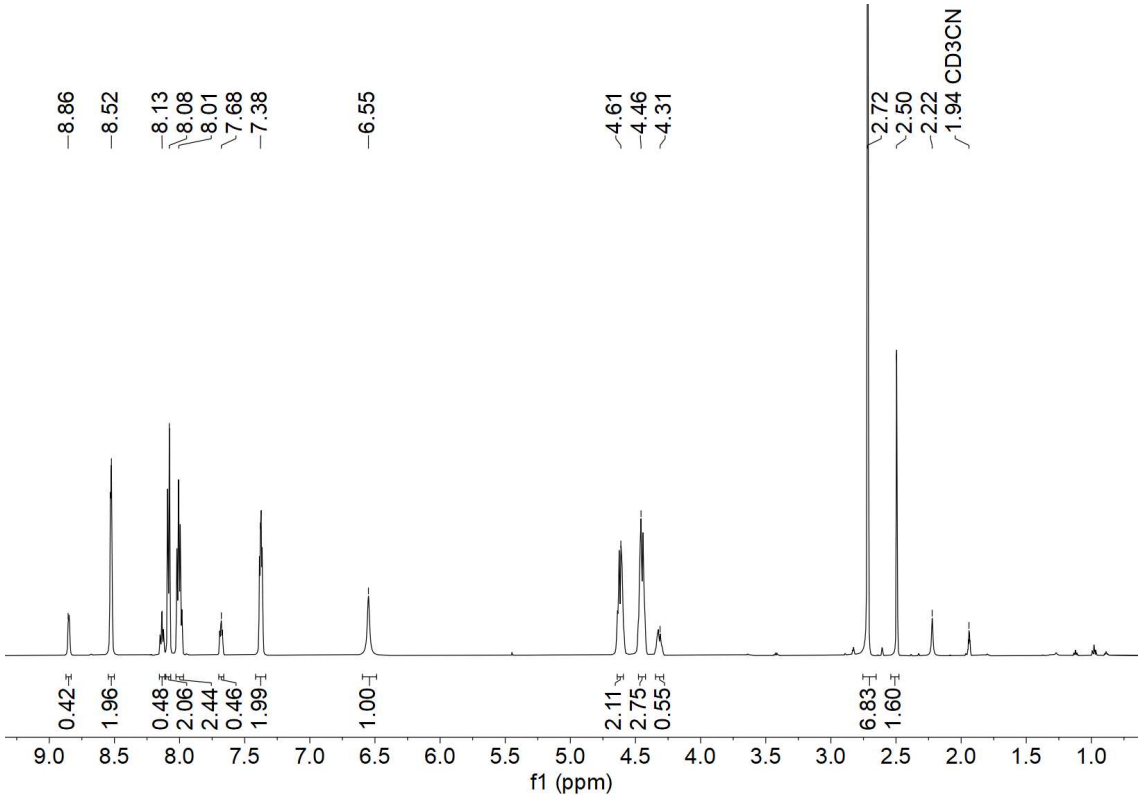

Figure 31. ^{1}H NMR spectrum (600 MHz, CD_3CN, 298 K, 42.51 mM) of [**11**][OTf]$_4$. Two sets of peaks, one due to [**11**][OTf]$_4$ and the other set is suspected as [**6**][OTf]$_4$**.**

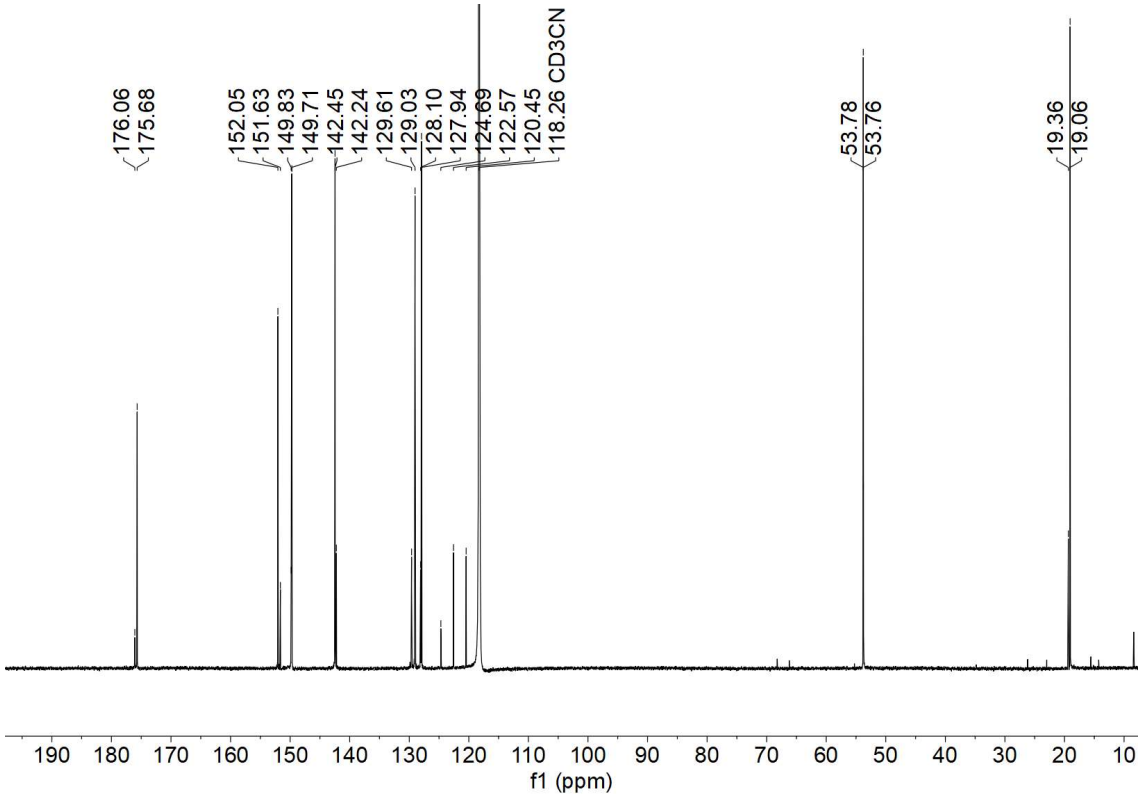

Figure 32. ^{13}C NMR spectrum (151 MHz, CD_3CN, 298 K, 42.51 mM) of [**11**][OTf]$_4$. Two sets of peaks, one due to [**11**][OTf]$_4$ and the other set is suspected as [**6**][OTf]$_4$**.**

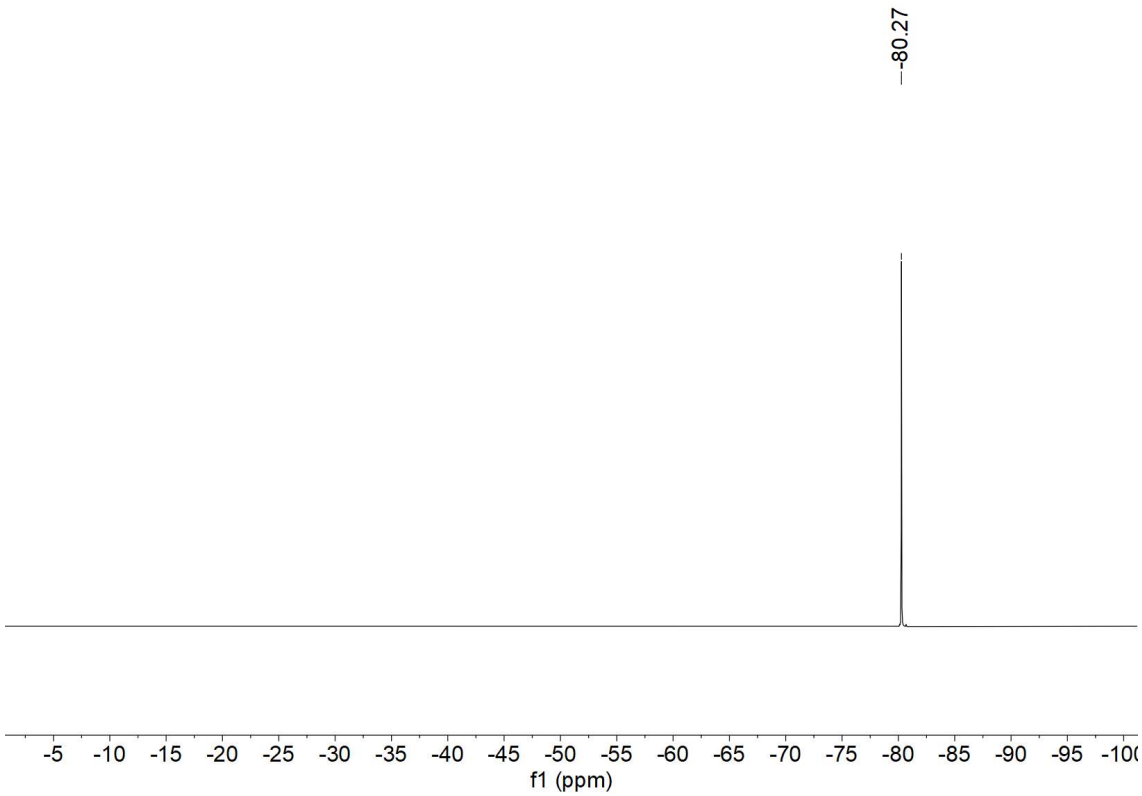

Figure 33. ^{19}F NMR spectrum (564 MHz, CD_3CN, 298 K, 42.51 mM) of [**11**][OTf]$_4$.

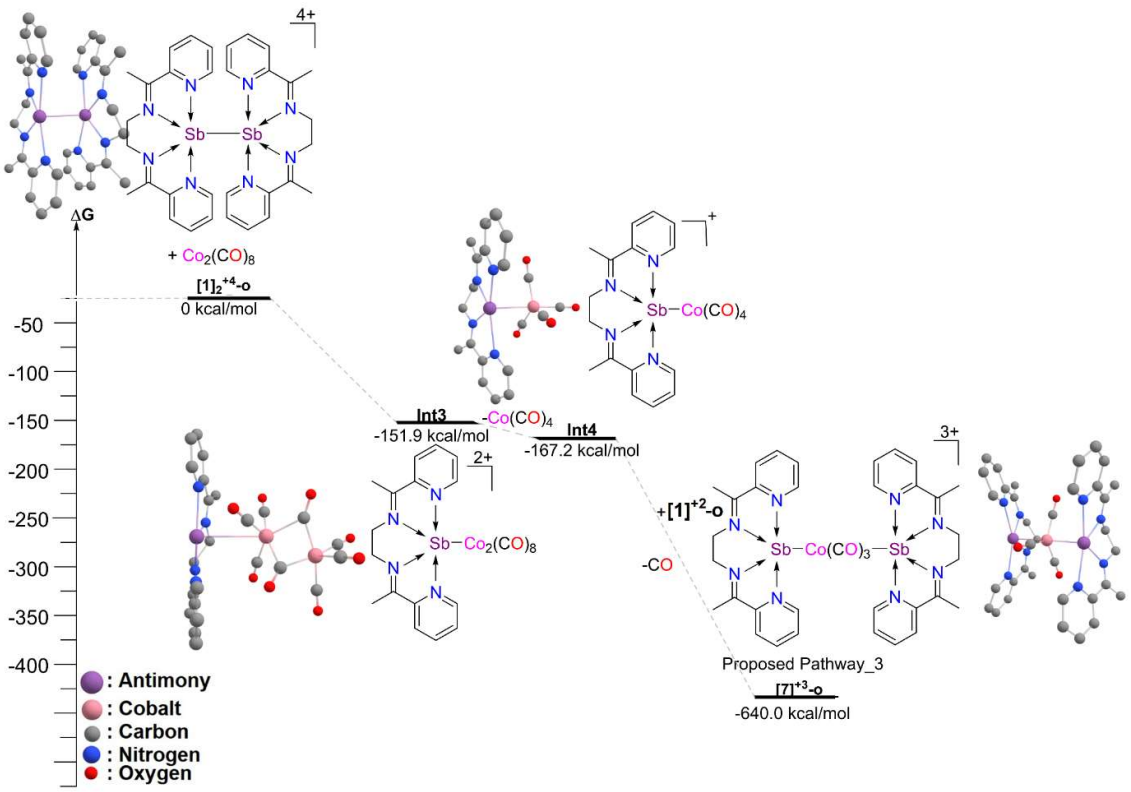

Figure 34. Proposed pathway for the formation of the compound $[\mathbf{7}]^{3+}$-o([SbCo][OTf]$_3$) from $[\mathbf{1}]_2^{4+}$-o + $Co_2(CO_8)$ via intermediate 3 and 4 (**Int3** and **Int4**) at the BP86-D4/def2-TZVPP level of theory.

Table 1. Crystal data and structure refinement for [**3**][OTf]$_2$.

Color	Light green	
Empirical formula	C24 H23 Bi1 F6 N4 O6 S3	
Formula weight	882.6225	
Temperature	150(2) K	
Wavelength	0.71073 Å	
Crystal system	Monoclinic	
Space group	P 21/c	
Unit cell dimensions	a = 12.0953(14) Å	a= 90°.
	b = 15.5017(15) Å	b= 104.899(3)°.
	c = 17.973(2) Å	g = 90°.
Volume	3256.5(6) Å^3	
Z	4	
Density (calculated)	1.800 Mg/m^3	
Absorption coefficient	5.683 mm^{-1}	
F(000)	1712	
Crystal size	0.200 x 0.060 x 0.040 mm^3	
Theta range for data collection	2.182 to 25.179°.	
Index ranges	-14<=h<=14, -18<=k<=16, -21<=l<=21	
Reflections collected	60934	
Independent reflections	5835 [R(int) = 0.0748]	
Completeness to theta = 25.179°	99.4 %	
Refinement method	Full-matrix least-squares on F^2	
Data / restraints / parameters	5835 / 0 / 382	
Goodness-of-fit on F^2	1.037	
Final R indices [I>2sigma(I)]	R1 = 0.0641, wR2 = 0.1626	
R indices (all data)	R1 = 0.0744, wR2 = 0.1730	
Extinction coefficient	0.00041(18)	
Largest diff. peak and hole	1.9227 and -2.328 e.Å^{-3}	

Table 2. Crystal data and structure refinement for [**4**][OTf]$_2$.

Identification code	HH_BI2_SEPH_solved
Chemical formula	C24H23BiF6N4O6S2Se
Formula weight	929.52 g/mol
Temperature	296(2) K
Wavelength	0.71073 Å
Crystal system	triclinic
Space group	P -1
Unit cell dimensions	a = 13.3900 Å α = 80.010°
b = 15.1970 Å	β = 81.930°
c = 16.3940 Å	γ = 74.860°
Volume	3155.5 Å^3
Z	4
Density (calculated)	1.957 g/cm^3
Absorption coefficient	6.952 mm^{-1}
F(000)	1784
Theta range for data collection	1.93 to 25.14°
Index ranges	-15<=h<=15, -18<=k<=18, -19<=l<=19
Reflections collected	75252
Independent reflections	11188 [R(int) = 0.0640]
Completeness to theta = 25.143°	99.2 %
Refinement method	Full-matrix least-squares on F^2
Refinement program	SHELXL-2019/1 (Sheldrick, 2019)
Function minimized	Σ w(Fo^2 - Fc^2)^2
Data / restraints / parameters	11188 / 0 / 797
Goodness-of-fit on F^2	1.038
Δ/σmax	0.002
Final R indices 10054 data; I>2σ(I)	R1 = 0.0403, wR2 = 0.1021
all data	R1 = 0.0469, wR2 = 0.1064
Weighting scheme	w=1/[σ^2(Fo^2)+(0.0455P)^2+45.5783P] where P=(Fo^2+2Fc^2)/3
Largest diff. peak and hole	5.271 and -1.099 eÅ^{-3}
R.M.S. deviation from mean	0.212 eÅ^{-3}

Table 3. Crystal data and structure refinement for [**5**][OTf]$_4$.

Color	Dark Red	
Chemical formula	C42H40Bi2F12N8O14S4	
Formula weight	1655.02 g/mol	
Temperature	150(2) K	
Wavelength	0.71073 Å	
Crystal size	0.020 x 0.050 x 0.070 mm	
Crystal system	triclinic	
Space group	P -1	
Unit cell dimensions	a = 10.4570 Å	α = 90.000°
	b = 10.0740 Å	β = 93.010°
	c = 25.1960 Å	γ = 90.020°
Volume	2650.6 Å^3	
Z	2	
Density (calculated)	2.074 g/cm^3	
Absorption coefficient	6.901 mm^{-1}	
F(000)	1596	
Theta range for data collection	1.95 to 25.10°	
Index ranges	-12<=h<=11, -12<=k<=12, -30<=l<=30	
Reflections collected	53414	
Independent reflections	9390 [R(int) = 0.0532]	
Completeness to theta = 25.10°	99.6 %	
Max. and min. transmission	0.8740 and 0.6440	
Refinement method	Full-matrix least-squares on F^2	
Refinement program	SHELXL-2019/1 (Sheldrick, 2019)	
Function minimized	Σ w(Fo^2 - Fc^2)^2	
Data / restraints / parameters	9390 / 24 / 713	
Goodness-of-fit on F^2	1.069	
Δ/σmax	0.003	
Final R indices 8361 data; I>2σ(I)	R1 = 0.0434, wR2 = 0.1076	
all data	R1 = 0.0506, wR2 = 0.1125	
Weighting scheme	w=1/[σ^2(Fo^2)+(0.0535P)^2+35.5055P]	
	where P=(Fo^2+2Fc^2)/3	
Largest diff. peak and hole	2.421 and -1.605 eÅ^{-3}	

Table 4. Crystal data and structure refinement for [**6**][OTf]$_4$.

Color	Dark Yellow	
Chemical formula	C35.50Bi2F12N8.50O13S4	
Formula weight	1527.64 g/mol	
Temperature	150(2) K	
Wavelength	0.71073 Å	
Crystal size	0.040 x 0.050 x 0.050 mm	
Crystal system	triclinic	
Space group	P -1	
Unit cell dimensions	a = 11.4450 Å	α = 74.320°
	b = 20.8780 Å	β = 82.580°
	c = 21.8050 Å	γ = 80.430°
Volume	4927.1 Å^3	
Z	4	
Density (calculated)	2.059 g/cm^3	
Absorption coefficient	7.416 mm^{-1}	
F(000)	2858	
Theta range for data collection	1.02 to 25.31°	
Index ranges	-13<=h<=13, -24<=k<=24, -26<=l<=25	
Reflections collected	29597	
Independent reflections	17313 [R(int) = 0.0869]	
Completeness to theta = 25.31°	96.3 %	
Max. and min. transmission	0.7560 and 0.7080	
Refinement method	Full-matrix least-squares on F^2	
Refinement program	SHELXL-2019/1 (Sheldrick, 2019)	
Function minimized	Σ w(Fo^2 - Fc^2)^2	
Data / restraints / parameters	17313 / 1266 / 1201	
Goodness-of-fit on F^2	1.041	
Δ/σmax	0.217	
Final R indices 9338 data; I>2σ(I)	R1 = 0.0838, wR2 = 0.1925	
all data	R1 = 0.1650, wR2 = 0.2361	
Weighting scheme	w=1/[σ^2(Fo^2)+(0.0865P)^2+52.7424P]	
	where P=(Fo^2+2Fc^2)/3	
Largest diff. peak and hole	4.605 and -4.507 eÅ^{-3}	
R.M.S. deviation from mean	0.276 eÅ^{-3}	

Table 5. Crystal data and structure refinement for [**7**][OTf]$_3$.

Color	Dark Red	
Chemical formula	C41.50H41.25Bi2CoF9N9.75O12S3	
Formula weight	1612.66 g/mol	
Temperature	296(2) K	
Wavelength	0.71073 Å	
Crystal system	orthorhombic	
Space group	P 21 21 21	
Unit cell dimensions	a = 11.31(3) Å	α = 90°
	b = 14.32(3) Å	β = 90°
	c = 31.79(8) Å	γ = 90°
Volume	5150.(20) Å^3	
Z	4	
Density (calculated)	2.081 g/cm^3	
Absorption coefficient	7.364 mm^{-1}	
F(000)	3106	
Theta range for data collection	2.21 to 25.53°	
Index ranges	-13<=h<=13, -17<=k<=17, -38<=l<=38	
Reflections collected	56299	
Independent reflections	9562 [R(int) = 0.0815]	
Completeness to theta = 25.53°	99.5 %	
Refinement method	Full-matrix least-squares on F^2	
Refinement program	SHELXL-2019/1 (Sheldrick, 2019)	
Function minimized	Σ w(Fo^2 - Fc^2)^2	
Data / restraints / parameters	9562 / 42 / 719	
Goodness-of-fit on F^2	1.055	
Δ/σmax	0.001	
Final R indices 8897 data; I>2σ(I)	R1 = 0.0389, wR2 = 0.0807	
all data	R1 = 0.0446, wR2 = 0.0828	
Weighting scheme	w=1/[σ^2(Fo^2)+(0.0305P)^2+22.4450P]	
	where P=(Fo^2+2Fc^2)/3	
Absolute structure parameter	0.300(8)	
Largest diff. peak and hole	1.729 and -1.940 eÅ^{-3}	
R.M.S. deviation from mean	0.181 eÅ^{-3}	

Table 6. Crystal data and structure refinement for [**LBiCo(CO)$_4$**][OTf]$_2$.

Color	Light red	
Chemical formula	C23H18BiCoF6N4.50O10S2	
Formula weight	963.45 g/mol	
Temperature	150(2) K	
Wavelength	0.71073 Å	
Crystal size	0.040 x 0.120 x 0.150 mm	
Crystal system	monoclinic	
Space group	C 1 2/c 1	
Unit cell dimensions	a = 27.5080 Å	α = 90.000°
	b = 15.6290 Å	β = 125.570°
	c = 17.6860 Å	γ = 90.000°
Volume	6184.8 Å3	
Z	8	
Density (calculated)	2.069 g/cm^3	
Absorption coefficient	6.451 mm^{-1}	
F(000)	3708	
Theta range for data collection	2.31 to 25.10°	
Index ranges	-19<=h<=32, -16<=k<=18, -21<=l<=19	
Reflections collected	18163	
Independent reflections	5455 [R(int) = 0.0787]	
Completeness to theta = 25.10°	99.1 %	
Max. and min. transmission	0.7820 and 0.4450	
Refinement method	Full-matrix least-squares on F^2	
Refinement program	SHELXL-2019/1 (Sheldrick, 2019)	
Function minimized	Σ w(Fo^2 - Fc^2)^2	
Data / restraints / parameters	5455 / 0 / 468	
Goodness-of-fit on F^2	1.013	
Δ/σmax	0.001	
Final R indices 4053 data; I>2σ(I)	R1 = 0.0399, wR2 = 0.0824	
all data	R1 = 0.0662, wR2 = 0.0921	
Weighting scheme	w=1/[σ^2(Fo^2)+(0.0288P)^2+1.5075P]	
	where P=(Fo^2+2Fc^2)/3	
Largest diff. peak and hole	1.066 and -1.141 eÅ^{-3}	
R.M.S. deviation from mean	0.168 eÅ^{-3}	

Table 7. Crystal data and structure refinement for [**8**][OTf]$_2$.

Color	Light Yellow	
Chemical formula	C25H21BiF6MnN5O11S2	
Formula weight	1009.51 g/mol	
Temperature	273(2) K	
Wavelength	0.71073 Å	
Crystal system	triclinic	
Space group	P -1	
Unit cell dimensions	a = 13.2490 Å	α = 90.080°
	b = 14.6760 Å	β = 90.070°
	c = 18.8090 Å	γ = 111.060°
Volume	3413.0 Å^3	
Z	4	
Density (calculated)	1.965 g/cm^3	
Absorption coefficient	5.737 mm^{-1}	
F(000)	1952	
Theta range for data collection	1.08 to 25.16°	
Index ranges	-15<=h<=15, -17<=k<=17, -22<=l<=22	
Reflections collected	30412	
Independent reflections	12174 [R(int) = 0.0771]	
Completeness to theta = 25.179°	99.4 %	
Refinement method	Full-matrix least-squares on F^2	
Refinement program	SHELXL-2019/1 (Sheldrick, 2019)	
Function minimized	Σ w(Fo^2 - Fc^2)^2	
Data / restraints / parameters	12174 / 0 / 920	
Goodness-of-fit on F^2	1.043	
Δ/σmax	0.001	
Final R indices 9078 data; I>2σ(I)	R1 = 0.0502, wR2 = 0.0989	
all data	R1 = 0.0819, wR2 = 0.1104	
Weighting scheme	w=1/[σ2(Fo^2)+(0.0423P)^2]	
	where P=(Fo^2+2Fc^2)/3	
Extinction coefficient	0.0002(1)	
Largest diff. peak and hole	2.423 and -2.673 eÅ^{-3}	
R.M.S. deviation from mean	0.216 eÅ^{-3}	

Table 8. Crystal data and structure refinement for [**9**][OTf]$_2$.

Color	Dark Red	
Chemical formula	C27H26BiF6FeN5O8S2	
Formula weight	991.48 g/mol	
Temperature	296(2) K	
Wavelength	0.71073 Å	
Crystal system	triclinic	
Space group	P -1	
Unit cell dimensions	a = 10.7140 Å	α = 66.330°
	b = 13.3390 Å	β = 72.870°
	c = 13.6310 Å	γ = 74.650°
Volume	1681.0 Å^3	
Z	2	
Density (calculated)	1.959 g/cm^3	
Absorption coefficient	5.872 mm^{-1}	
F(000)	964	
Theta range for data collection	2.02 to 25.70°	
Index ranges	-13<=h<=13, -16<=k<=16, -16<=l<=13	
Reflections collected	20994	
Independent reflections	6138 [R(int) = 0.0640]	
Completeness to theta = 25.70°	96.3 %	
Refinement method	Full-matrix least-squares on F^2	
Refinement program	SHELXL-2019/1 (Sheldrick, 2019)	
Function minimized	Σ w(Fo^2 - Fc^2)^2	
Data / restraints / parameters	6138 / 18 / 454	
Goodness-of-fit on F^2	1.058	
Final R indices 5553 data; I>2σ(I)	R1 = 0.0807, wR2 = 0.2184	
all data	R1 = 0.0891, wR2 = 0.2262	
Weighting scheme	w=1/[σ^2(Fo^2)+(0.1227P)^2+79.8166P]	
	where P=(Fo^2+2Fc^2)/3	
Largest diff. peak and hole	8.119 and -3.646 eÅ^{-3}	
R.M.S. deviation from mean	0.382 eÅ^{-3}	

Table 9. Crystal data and structure refinement for [**10**][OTf]$_2$.

Color	Colorless
Chemical formula	C19H21BiF5.50N4O6S2
Formula weight	779.00 g/mol
Temperature	273(2) K
Wavelength	0.71073 Å
Crystal system	monoclinic
Space group	C 1 2/c 1
Unit cell dimensions	a = 27.0800 Å α = 90.000°
b = 9.3060 Å	β = 118.960°
c = 24.0650 Å	γ = 90.000°
Volume	5306.2 Å^3
Z	8
Density (calculated)	1.950 g/cm^3
Absorption coefficient	6.882 mm^{-1}
F(000)	3004
Theta range for data collection	1.86 to 25.26°
Index ranges	-32<=h<=32, -11<=k<=11, -28<=l<=28
Reflections collected	28784
Independent reflections	4745 [R(int) = 0.0540]
Completeness to theta = 25.26°	98.6 %
Refinement method	Full-matrix least-squares on F^2
Refinement program	SHELXL-2019/1 (Sheldrick, 2019)
Function minimized	Σ w(Fo^2 - Fc^2)^2
Data / restraints / parameters	4745 / 12 / 346
Goodness-of-fit on F^2	1.062
Δ/σmax	0.005
Final R indices 4201 data; I>2σ(I)	R1 = 0.0269, wR2 = 0.0576
all data	R1 = 0.0338, wR2 = 0.0607
Weighting scheme	w=1/[σ^2(Fo^2)+(0.0167P)^2+41.3114P] where P=(Fo^2+2Fc^2)/3
Largest diff. peak and hole	1.275 and -0.894 eÅ^{-3}
R.M.S. deviation from mean	0.126 eÅ^{-3}

Table 10. Crystal data and structure refinement for [**11**][OTf]$_2$.

Color	Colorless	
Chemical formula	C44H52Bi2F12N12O14S4	
Formula weight	1747.17 g/mol	
Temperature	150(2) K	
Wavelength	0.71073 Å	
Crystal size	0.050 x 0.050 x 0.060 mm	
Crystal system	monoclinic	
Space group	C 1 2/c 1	
Unit cell dimensions	a = 22.471(8) Å	α = 90°
	b = 17.323(6) Å	β = 96.497(10)°
	c = 15.572(6) Å	γ = 90°
Volume	6023.(4) Å^3	
Z	4	
Density (calculated)	1.927 g/cm^3	
Absorption coefficient	6.082 mm^{-1}	
F(000)	3400	
Theta range for data collection	2.35 to 25.50°	
Index ranges	-27<=h<=22, -19<=k<=20, -18<=l<=18	
Reflections collected	20130	
Independent reflections	5547 [R(int) = 0.0742]	
Completeness to theta = 25.50°	98.9 %	
Max. and min. transmission	0.7510 and 0.7120	
Refinement method	Full-matrix least-squares on F^2	
Refinement program	SHELXL-2019/1 (Sheldrick, 2019)	
Function minimized	Σ w(Fo^2 - Fc^2)^2	
Data / restraints / parameters	5547 / 0 / 409	
Goodness-of-fit on F^2	1.016	
Δ/σmax	0.002	
Final R indices 4292 data; I>2σ(I)	R1 = 0.0409, wR2 = 0.0895	
all data	R1 = 0.0610, wR2 = 0.0977	
Weighting scheme	w=1/[σ^2(Fo^2)+(0.0454P)^2]	
	where P=(Fo^2+2Fc^2)/3	
Largest diff. peak and hole	3.850 and -2.669 eÅ^{-3}	
R.M.S. deviation from mean	0.185 eÅ^{-3}	

Table 11. Crystal data and structure refinement for [**LSb-Co(CO)$_3$-SbL**][OTf]$_3$

Empirical formula	C88 H94 Co2 F18 N20 O25 S6 Sb4	
Color	Reddish-brown	
Formula weight	2971.05	
Temperature	273(2) K	
Wavelength	0.71073 Å	
Crystal system	Triclinic	
Space group	$P\bar{1}$	
Unit cell dimensions	a = 15.741(7) Å	α= 82.917(9)°.
	b = 15.777(7) Å	β= 87.028(9)°.
	c = 23.919(11) Å	γ = 79.689(9)°.
Volume	5797(5) Å^3	
Z	2	
Density (calculated)	1.702 Mg/m^3	
Absorption coefficient	1.411 mm^{-1}	
F(000)	2956	
Crystal size	0.272 x 0.173 x 0.118 mm^3	
Theta range for data collection	0.858 to 25.000°.	
Index ranges	-18<=h<=18, -18<=k<=18, -28<=l<=28	
Reflections collected	42106	
Independent reflections	42106 [R(int) = 11.11]	
Completeness to theta = 25.000°	96.0 %	
Absorption correction	Semi-empirical from equivalents	
Max. and min. transmission	0.76 and 0.55	
Refinement method	Full-matrix least-squares on F^2	
Data / restraints / parameters	42106 / 4438 / 1555	
Goodness-of-fit on F^2	1.023	
Final R indices [I>2sigma(I)]	R1 = 0.1072, wR2 = 0.2410	
R indices (all data)	R1 = 0.1881, wR2 = 0.2987	
Extinction coefficient	0.00129(13)	
Largest diff. peak and hole	2.935 and -1.736 e.Å^{-3}	

Table 12. Crystal data and structure refinement for [**LSb-Mn(CO)$_5$**][OTf]$_2$.

Color	Orange	
Chemical formula	C23H18F6MnN4O11S2Sb	
Formula weight	881.22 g/mol	
Temperature	150(2) K	
Wavelength	0.71073 Å	
Crystal size	0.070 x 0.100 x 0.110 mm	
Crystal system	triclinic	
Space group	$P\bar{1}$	
Unit cell dimensions	a = 10.8232(9) Å	α = 77.056(2)°
	b = 12.9392(11) Å	β = 75.318(2)°
	c = 15.8153(13) Å	γ = 77.479(2)°
Volume	2057.8(3) Å^3	
Z	2	
Density (calculated)	1.422 g/cm^3	
Absorption coefficient	1.140 mm^{-1}	
F(000)	868	
Theta range for data collection	1.93 to 25.40°	
Index ranges	-13<=h<=13, -15<=k<=15, -19<=l<=17	
Reflections collected	30003	
Independent reflections	7502 [R(int) = 0.0865]	
Completeness to theta = 25.40°	99.0 %	
Max. and min. transmission	0.9240 and 0.8850	
Refinement method	Full-matrix least-squares on F^2	
Data / restraints / parameters	7502 / 1 / 453	
Goodness-of-fit on F^2	1.043	
Final R indices	R1 = 0.0601, wR2 = 0.1482	
R indices (all data)	R1 = 0.0835, wR2 = 0.1613	
Largest diff. peak and hole	0.999 and -1.423 eÅ^{-3}	
R.M.S. deviation from mean	0.143 eÅ^{-3}	